Structural-Functional Studies on PSI-IsiA Super-complex in *Synechocystis* sp. PCC 6803

by

Jin Li

A Dissertation Presented in Partial Fulfillment
of the Requirements for the Degree
Doctor of Philosophy

Approved April 2024 by the
Graduate Supervisory Committee:

Yuval Mazor, Chair
Po-Lin Chiu
Jeremy Mills

ARIZONA STATE UNIVERSITY

May 2024

ABSTRACT

The thylakoid membranes of oxygenic photosynthetic organisms contain four large membrane complexes vital for photosynthesis: photosystem II and photosystem I (PSII and PSI, respectively), the cytochrome b_6f complex and ATP synthase. Two of these complexes, PSII and PSI, utilize solar energy to carry out the primary reaction of photosynthesis, light induced charge separation. In vivo, both photosystems associate with multiple antennae to increase their light absorption cross section. The antennae, Iron Stress Induced A (IsiA), is expressed in cyanobacteria as part of general stress response and forms a ring system around PSI. IsiA is a member of a large and relatively unexplored antennae family prevalent in cyanobacteria. The structure of the PSI-IsiA super-complex from the cyanobacteria *Synechocystis* sp. PCC 6803 was resolved to high resolution, revealing how IsiA interacts with PSI as well as the chlorophyll organization within this antennae system. Despite these structural insights, the basis for the binding between 18 IsiA subits and PSI is not fully resolved. Several IsiA mutants were constructed using insights from the atomic structure of PSI-IsiA, revealing the role of the C-terminus of IsiA in its interaction with PSI.

ACKNOWLEDGMENTS

I would like to express my deepest appreciation to my PI, my committee chair, Dr. Yuval Mazor, for his invaluable patience and encouragement during my Ph.D. I know you are always anxious about every unexpected event in the lab but I hope you can relieve stress sometime. I also could not have undertaken this journey without my defense committee, Dr. Po-lin Chiu and Dr. Jememy Mills, who generously provided knowledge and expertise on my presentation and dissertation. Additionally, this endeavor would not have been possible without the help of Dr. Hila Toporik, who trains me to learn how to use a pipette from ground.

I am also grateful to my lab members, Christopher Gorski, Halima Khatun, Kelsey Krail, Ranel Maqdisi, Zhen Da, including our previous lab member Dr. Reece Riddle and Dr. Zachary Dobson, for their daily help, late-night lab cleaning, and moral support. Many thanks should also go to our collaborator and research assistants, Anton Khmelnitskiy and Dwight Williams from Arizona State University, who helped me to operate TCSPC, streak camera, sample preparation robot and cryo-TEM.

Lastly, I would be remiss in not mentioning my family, especially my parents, my girlfriend and my dog, Nano. Their belief in me has kept my spirits and motivation high during this process. I would also like to thank my friend, Liang Jing, Chang Liu, Yue Tang, Lan Zhu and Tina Chen. Hanging out with you guys saves all my weekend lab time.

TABLE OF CONTENTS

Page

LIST OF TABLES v

LIST OF FIGURES vi

LIST OF ABREVATIONS viii

CHAPTER

1 INTRODUCTION 1

History of Photosynthesis 1

Oxygenic Photosynthesis 2

Antennae 7

Cyanobacteria 9

Spectroscopy of Photosynthetic Systems 12

Kinetics of $P700^+$ Absorbance 19

Ultrafast Spectroscopy 19

Iron Limitation in the Ocean 22

Introduction to Cryo-Em 24

Cryo-Em Workflow 28

Scope of Thesis 37

2 THE STRUCTURE OF STRESS-INDUCED PSI-ISIA ANTENNAE SUPERCOMPLEX 39

Introduction 39

Methods 44

Results 51

Discussions 60

Figure Supplements 62

CHAPTER Page

3 LOSS OF ISIA C-TERMINUS REVEALS A NEW ROLE OF PSI-ISIA ASSEMBLIES. 63

Introduction 63

Methods 67

Results 73

Discussions 85

Figure Supplements 88

4 STRUCTURAL BASIS FOR ENERGY TRANSFER IN THE PSI-ISIA SUPERCOMPLEX. 92

Introduction 92

Methods 95

Results 98

Discussions 101

5 CONCLUDING REMARKS AND FUTURE OUTLOOK 102

REFERENCES 104

APPENDIX

A PERMISSIONS 116

LIST OF TABLES

Table Page

2.1. Data Collection and Processing Statistics 53

S2.1. Mg to Mg Distances in the IsiA Monomer 62

S2.2. Chlorophyll Coordination in IsiA. 62

3.1. Fluorescence Lifetime 81

LIST OF FIGURES

Figure Page

1.1. Four Essential Complexes for the Light Reactions of Oxygenic Photosynthesis ...3

1.2. Z-Scheme of Electron Transport in Photosynthesis 6

1.3. Varieties of PSI-Lhc Antennae Supercomplexes among Species 8

1.4. Transmission Electron Microscopy of *Synechocystis* 6803 Cells 11

1.5. Chemical Structures of Chlorophylls 13

1.6. Terrestrial Solar Irradiance and Photosynthetic Absorption Spectra 15

1.7. Schematic Potential Energy Diagrams and Spectra for Energy Transitions 16

1.8. Chlorophyll A Concentration Map in 1997 23

1.9. The Global Distribution of Iron (Fe) in The World's Oceans 24

1.10. The Development of Cryo-Em 26

1.11. Growth of Structures Solved by Electron Microscopy 27

1.12. A Schematic Image of Grids....30

1.13. A Plunge-Freezing Robot with Schematic Image 32

1.14. The Process of Preparing Biological Specimens on Grids 33

1.15. The Basic Process for Image Processing in Cryo-Em 35

2.1. The Initial Discovered on Isia 40

2.2. Electron Microscope Image of Psi-Isia 42

2.3. Iron Optimization of PsI-IsiA and PsI-IsiA Characterization 44

2.4. Image Processing Strategy 48

2.5. Global and Local Resolution 50

2.6. An Overview of Psi-Isia 52

2.7. Organization of Two Chlorophyll Layers in Psi-Isia 56

2.8. Structure of Isia 58

Figure Page

3.1. An Overview of The Isia Monomer 65

3.2. Conformational Flexibility among IsiA Dimers 67

3.3. Growth Rate among Wt, IsiaΔc and Δisia 75

3.4. Spectroscopic Measurements of Wt, IsiaΔc and Δisia. 77

3.5. Fluorescence of Wt, IsiaΔc And Δisia 78

3.6. Functional Antennae Size of Wt And IsiaΔc 79

3.7. Time-Resolved Fluorescence Spectral 80

3.8. Isolation of Psi-IsiaΔC from Strain IsiaΔC 83

3.9. The Structure of Psi-IsiaΔC 84

S3.1. Schematic Diagram of Wt Transformation and Agarose Gel 88

S3.2. Schematic Diagram of IsiaΔC Transformation and Agarose Gel 89

S3.3. Schematic Diagram of ΔIsia Transformation and Agarose Gel 90

S3.4. Image Processing Strategy 90

4.1. Lumenal Chlorophylls Distance From IsiA to PsI 94

4.2. Part of Alignment Result of Isia on *Synechocystis* 6803 96

4.3. Normalized Absorption Spectra of IsiaΔChl17_1, IsiaΔChl17_2 99

4.4. Sucrose Gradient Fraction 100

LIST OF ABBREVIATION

Word	Symbol
Photosystem I	PSI
Photosystem II	PSII
Chorophyll	Chl
Synechocystis sp. PCC 6803	*Synechocystis* 6803
Iron Stress Induced Protein A	IsiA
Linear Electron Transport Flow	LEF
Electron Transport Chain	ETC
Oxygen Evolving Center	OEC
Plastoquinone	PQ
Plastocyanin	PC
Ferredoxin-NADP+ Reductase	FNR
Cyanobacterial Phycocyanin Protein G	CpcG
Light-Harvesting Complex	LHC
Cryogenic Electron Microscope	Cryo-EM
Time-Correlated Single Photon Counting	TCSPC
Single-Photon Timing	SPT
Nuclear Magnetic Resonance	NMR

CHAPTER 1

INTRODUCTION

History of Photosynthesis

Photosynthesis is the only significant biological process utilizing solar energy and storing it as chemical bond, fueling the majority of life's processes. From land to the sea, photosynthetic organisms encompass a wide range of life forms, including plants, algae, and cyanobacteria. In plants, photosynthesis primarily occurs in chloroplasts, specialized organelles found in plant cells. Algae, ranging from microscopic unicellular species to large multicellular seaweeds, also conduct photosynthesis, often using chlorophyll pigments to capture the light and convert it to forms usable by living organisms. Cyanobacteria contain specialized structures called thylakoids where photosynthetic reactions take place. Through photosynthesis, these organisms not only produce oxygen essential for aerobic respiration but also generate organic compounds that serve as the building blocks for all life on our planet (Blankenship 2002).

Our understanding of the earliest origins of photosynthesis remains limited. While various hypotheses have been proposed regarding its inception, direct evidence supporting any specific origin is lacking. Suggestive evidence indicates the presence of photosynthetic organisms around 3.2 to 3.5 billion years ago, inferred from the existence of stromatolites—layered structures akin to those formed by modern cyanobacteria—as well as microfossils interpreted as originating from phototrophs (Blankenship and Blankenship 1992a). It’s proven that photosynthesis commenced relatively early in Earth's timeline. However, it is unlikely to have been among the earliest metabolic chemical processes. The earliest forms of photosynthesis are believed to have been anoxygenic, with oxygenic forms emerging at a later stage (Blankenship 2010).

One of the most debated yet poorly understood milestones in the evolution of photosynthesis is the development of the capability to utilize water as an electron donor, leading to the production of oxygen as a byproduct and marking the advent of oxygenic photosynthesis (Blankenship and Blankenship 2010). The release of oxygen and its subsequent buildup in the atmosphere had a profound and irreversible impact on Earth, facilitating the emergence of complex life forms that rely on oxygen for aerobic respiration. Multiple lines of geochemical evidence suggest that atmospheric oxygen began to accumulate approximately 2.4 billion years ago, although the evolution of oxygenic photosynthesis likely preceded this event (Buick 2008).

In contrast to the intricate cells involved in contemporary oxygenic photosynthesis, the initial photosynthetic systems responsible for this process were probably less complex. Understanding the functioning of these earliest photosynthetic organisms poses a challenge due to the limited organisms available for examination, as only those that have persisted until today can be studied (Raymond and Blankenship 2008). Overall, while the exact details of the origins of photosynthetic organisms remain uncertain, ongoing research continues to shed light on the evolutionary processes that led to the development of this fundamental biological process, which played a crucial role in shaping Earth's atmosphere and supporting diverse forms of life.

Oxygenic photosynthesis

Oxygenic photosynthesis comprises a crucial series of biochemical reactions for all life on earth as it produces oxygen and supplies most of the energy utilized by living organisms. The engines that drive the light reactions of oxygenic photosynthesis are located in thylakoid membrane of photoautotrophs (Nelson and Ben-Shem 2004). Thylakoid membranes contain four large complexes vital for photosynthesis: PSII, cytochrome b_6f, PSI and ATP synthase (Figure1.1). Across domains, these four complexes show high

conservation within oxygenic photosynthetic organisms (Nelson and Yocum 2006). Two of these complexes, PSII and PSI, utilize hundreds of pigments to absorb light energy and subsequently transfer this energy to a reaction center comprised of a special chlorophyll pairs, P680 and P700, in PSII and PSI respectively, where charge separation take place (Nelson and Ben-Shem 2004; Nelson and Yocum 2006). The electron transferred by this event is moved uphill energetically by these complexes and passed along the electron transport chain, eventually being stored as high energy chemical bonds.

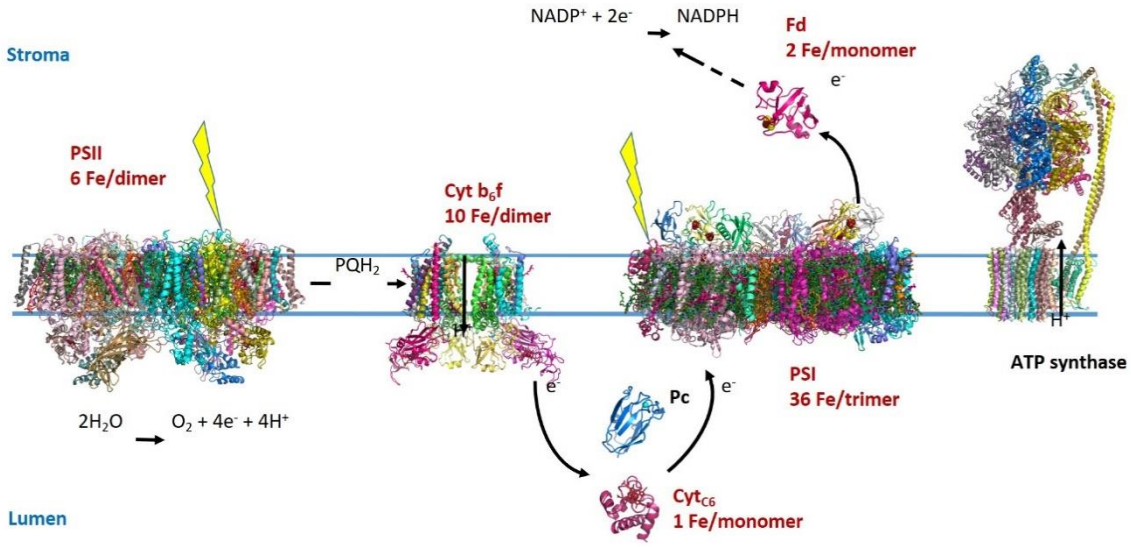

Figure 1.1. Sideview of the four essential complexes for the light reactions of oxygenic photosynthesis, placed in the thylakoid membrane (marked in blue). The initial charge separation takes place at the PSII and PSI reaction centers, causing electron transport from PSII to PSI via the cytochrome b_6f complex. Finally, the electrons passing through PSI reduce $NADP^+$ to NADPH providing the reducing power for carbon fixation. The iron content of each component in its most common biological form is marked in red.

The electron transport chain is a key component of the light-dependent reactions of photosynthesis, occurring within the thylakoid membranes of chloroplasts in all photosynthetic organisms (Genty, Briantais, and Baker 1989; Trebst 1974). This process

involves a series of electron carrier molecules that shuttle electrons, derived from the splitting of water molecules, through a sequence of redox reactions, ultimately leading to the production of ATP and NADPH.

The process of linear electron transport flow (LEF) starts with the absorption of light energy by chlorophyll molecules within Photosystem II (PSII), leading to the excitation of chlorophyll. These excited states are then transferred to the primary electron acceptor, P680. Upon reaching the reaction center, the captured energy ejects an electron to the Electron Transport Chain (ETC), resulting in a highly reactive $P680^{+}$ ion with a redox potential of +1.2 V (Barber and Archer 2001) (Figure 1.2). PSII catalyzes the splitting of water molecules, releasing oxygen as a byproduct and donating electrons to reduce $P680^{+}$. This process is essential for oxygenic photosynthesis and occurs on the Oxygen Evolving center (OEC) of the PSII.

The energized electrons from PSII are transferred through a series of electron carrier molecules, including plastoquinone (PQ), embedded within the thylakoid membrane. As electrons move through the PQ pool, from PSII to the cytochrome b_6f complex, their red-ox potential is utilized to pump protons (H^{+}) from the stroma into the thylakoid lumen, establishing a proton gradient. The cytochrome b_6f complex facilitates the transfer of electrons to plastocyanin (PC), a soluble electron carrier in the thylakoid lumen (Genty, Briantais, and Baker 1989).

The cytochrome b_6f complex exists as a homodimer, comprising four major subunits and four minor subunits in each monomer (Kurisu et al. 2003; Stroebel et al. 2003). Its primary role in linear electron flow involves proton pumping across the membrane, thereby contributing to the proton gradient. This process entails transferring protons from the stromal side of the membrane to the lumen through proton-coupled electron transfer,

ultimately reducing plastocyanin, which transports the electron to Photosystem I (PSI) (Kurisu et al. 2003; Stroebel et al. 2003).

The electrons from plastocyanin are transferred to PSI, where light energy was absorbed and converted it into chemical energy in the form of reduced ferredoxin (Fd) (Ben-Shem, Frolow, and Nelson 2003; Croce and Van Amerongen 2013) In order to reduce Fd, PSI utilize around 100 chlorophylls to absorb light photons and transfer electrons to 4Fe-4S iron sulfur cluster. Most of the electron transport pathway is on the reducing side of PSI, an electron from excited P700 to A (Chl a), A_0 (Chl a), A_1 (phylloquinone), F_X (4Fe4S cluster), F_A (4Fe4S cluster), and finally the terminal iron sulfur cluster, F_B (Jordan et al. 2001) (Figure 1.2). The electrons from the electron carriers within PSI eventually reduce ferredoxin and ferredoxin-$NADP^+$ reductase (FNR). Finally these electrons are used in the reduction of $NADP^+$ to NADPH. This NADPH serves as a reducing agent in the Calvin cycle, where it participates in the conversion of carbon dioxide into carbohydrates. Concurrently with electron transfer, by virtue of its PC oxidation, PSI generates a proton gradient across the thylakoid membrane by pumping protons (H^+ ions) from the stroma into the thylakoid lumen. This proton gradient is utilized by ATP synthase to drive the synthesis of ATP from ADP and inorganic phosphate (Pi) through a process known as chemiosmosis.

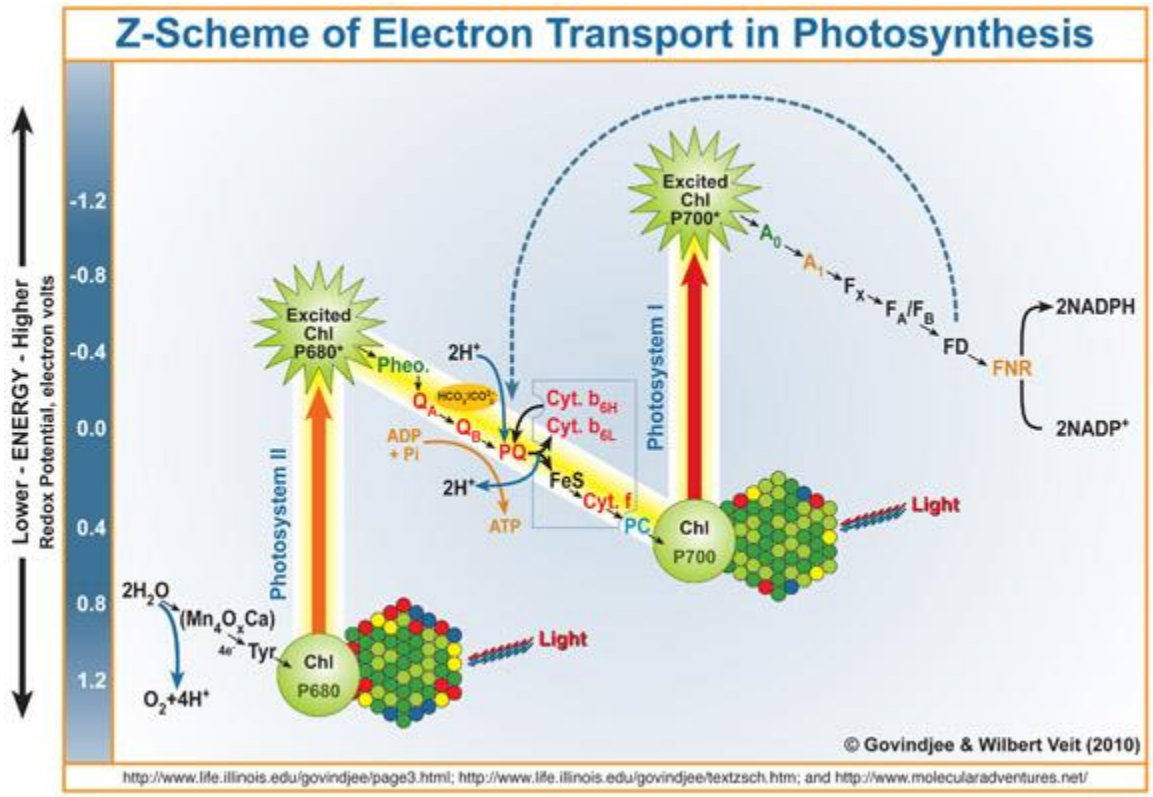

Figure 1.2. Z-Scheme of Electron Transport in Photosynthesis. . The energetic scheme of electron transport during the light reactions of photosynthesis illustrates the pathway of electrons from their extraction from water molecules by PSII to the reduction of NADP+ to NADPH by Ferredoxin-NADP reductase (FNR). Via the absorption of the light energy, the energy level of PSII and PSI show a vertical elevation on their reaction center. Oxygenic photosynthesis operates the redox potentials to the highest over +1.0 and lowest to −1.0 V, but the reactions in these extremes won't last over 1 ns because of fast energy transfer among them. Figure reproduced with permission of G. Govindjee and W. Viet (https://www.life.illinois.edu/govindjee/Z-Scheme.html)

Cyclic electron flow is a process in photosynthesis where electrons circulate within the photosynthetic electron transport chain without being transferred to $NADP^+$. Unlike linear electron flow, which involves the transfer of electrons from water to $NADP^+$ to produce NADPH, cyclic electron flow occurs when electrons are redirected back to the PSI complex

(DalCorso et al. 2008; Munekage et al. 2004). Cyclic electron flow (CEF) serves a significant function in photoprotection by inducing non-photochemical quenching and regulates the rate-limiting step of linear electron flow (LEF) (Allen 2003).

Antennae

In most cases, PSI and PSII associate with an outer antennae systems that enhances their light-harvesting capacity. From cyanobacteria to higher plants, the core complexes of PSI and PSII are primarily conserved. However, the composition of the outer antennae varies among different species (Thomas S. Bibby et al. 2003; Chmeliov et al. 2016; Mirkovic et al. 2017).

Cyanobacteria contain an additional light-harvesting antennae known as the phycobilisome (PBS), which enlarge the absorption of sunlight, particularly in the 575–675 nm range. Typically, the phycobilisome (PBS) is a supercomplex composed of rod and core subcomplexes, which encompass various phycobilin-binding proteins interconnected by several classes of unpigmented linker proteins. Phycocyanin (PC) serves as the predominant phycobiliprotein within the rod, while allophycocyanin (APC) predominates within the core cylinders. A critical player in PBS assembly is the rod–core linker protein known as cyanobacterial phycocyanin protein G (CpcG), which facilitates the connection between the rod and the core components (Grossman et al. 1993; J. Zhang et al. 2017). Because of structural homology of phycolilins to heme, heme is thought to be a precursor on the synthesis of phycobilins (Beale 1993). However, due to the limitation of iron in the ocean, IsiA serves as the primary antennae for marine cyanobacteria, enabling them to increase the proportion of light absorption (Gao et al. 2001). We will talk about IsiA in the next paragraph.

The core of cyanobacterial PSI comprise of 12 subunits, forming a monomer. In many species these monomers associate to from a trimer with a total molecular weight of 1068 kDa. In contrast, PSI in higher plants exists in a monomeric state and is encircled by four transmembrane subunits of the light-harvesting complex I (LHCI), Lhca1 to Lhca4, forming a PSI-LHCI supercomplex with 16 subunits and around 200 pigments, with a molecular weight exceeding 600 kDa. The pigment network maintains high quantum efficiency, arising from the optimal orientation of the pigments, for efficient energy transfer and their interaction with the surrounding protein environment (Mazor et al. 2015, 2017). Recent years, a great flow of eukaryotic PSI supercomplex has been solved with cryo-EM (Figure 1.3). It becomes much important to understand how PSI interacts with antennae in cyanobacteria.

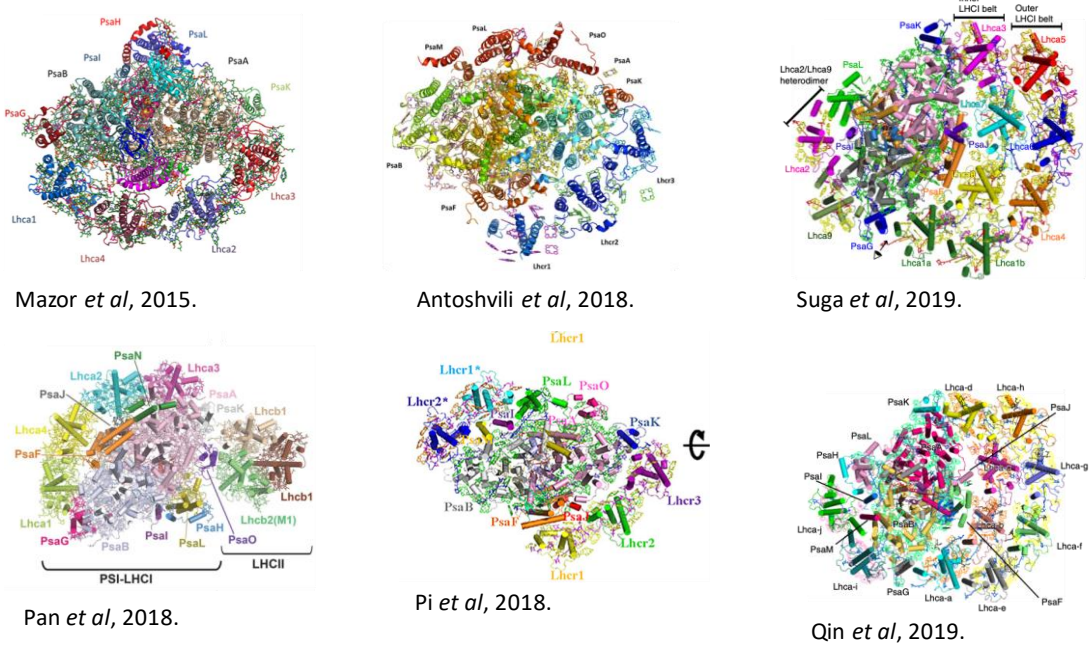

Mazor *et al*, 2015.

Antoshvili *et al*, 2018.

Suga *et al*, 2019.

Pan *et al*, 2018.

Pi *et al*, 2018.

Qin *et al*, 2019.

Figure 1.3. In eukaryotes, great varieties of PSI antennae supercomplexes among species. From left to right, PSI-LHCI supercomplexes from *pisum sativum* (Mazor et al. 2015). PSI antennae complexes with Lhca from *Cyanidioschyzon merolae* (Antoshvili et al. 2019). Structure of the green

algal PSI supercomplex (Suga et al. 2020). PSI-LHCI-LHCII supercomplex (Pan et al. 2018). PSI attached 2 LHCR site (Pi et al. 2018). PSI complexes from green algal PSI in complex (Qin et al. 2019).

Similarly, plants and algae evolved different Lhcb proteins which binds chlorophyll and carotenoid molecules, forming Light-Harvesting Complexes II (LHCII). In vascular plants, these apoproteins are labeled as Lhcb1-3, or major lhcb's, while in green algae and nonvascular plants, they are referred to as LhcbMs. Additionally, there are minor lhcb's proteins known as CP29 (Lhcb4), CP26 (Lhcb5), and CP24 (Lhcb6). To supply excitation energy to PSII, the LHCII proteins (Lhcb1-3), along with CP29, CP26, and CP24, must assemble closely with PSII to form the PSII–LHCII supercomplexes. This close arrangement facilitates the establishment of energy transfer pathways from the peripheral antennae to the core of PSII. The high-resolution structure of PSII–LHCII supercomplexes was recently observed through cryo-EM technology. Based on their structure, excitation energy transfer from the peripheral antennae complexes (LHCII, CP26, and CP29) to the core antennae complexes (CP43 or CP47) occurs through the interfacial chlorophyll pairs (Su et al. 2017; Wei et al. 2016).

Cyanobacteria

Known as ancient oxygenic photosynthetic bacteria, cyanobacteria has been thought to play a significant role in introducing oxygen into the atmosphere of early Earth and it has been found in almost every habitat on earth (Whitton and Potts 2007). As we mentioned in the history of photosynthesis, cyanobacteria played a vital role in transforming Earth's early reducing atmosphere into an oxidizing one approximately 2.4 billion years ago. In addtion, cyanobacteria living in tropical marine regions are responsible for approximately

50% of the earth's biological nitrogen fixation (Kruse et al. 2005). The energy flowing through all cyanobacteria surpasses the energy demand of human society by more than 25 times (approximately 15 TW), exceeding roughly 1,000 times the energy generated by all nuclear plants on Earth (Pisciotta, Zou, and Baskakov 2010).

Cyanobacteria shares the conserved biochemical reaction and photosynthetic protein, PSII, cytochrome b_6f, PSI and ATP synthase, (Figure 1.4) embedded in the thylakoid membrane. Due to the similarity betwee chloroplasts from eukaryotic organisms and cyanobacteria, cyanobacteria are an ideal system for studying the molecular mechanisms that underlie stress responses and stress adaptation in higher plants (Los et al. 2010). Consequently, studying these processes in cyanobacteria offers a more efficient approach, given their rapid growth rates, minimal space requirements, and the conclusions drawn from such investigations are applicable to high plants.

Among all cyanobacterial species, *Synechocystis* sp. PCC 6803, commonly referred to as *Synechocystis* 6803, is a unicellular cyanobacterium that has garnered significant attention as a model organism for research in various fields, including photosynthesis, stress biology, and biotechnology (Kaneko and Tabata 1997) (Figure 1.4). Under transmission electron microscope, the overall morphology of this organism and the thylakoid membrane arrangement could be observed.

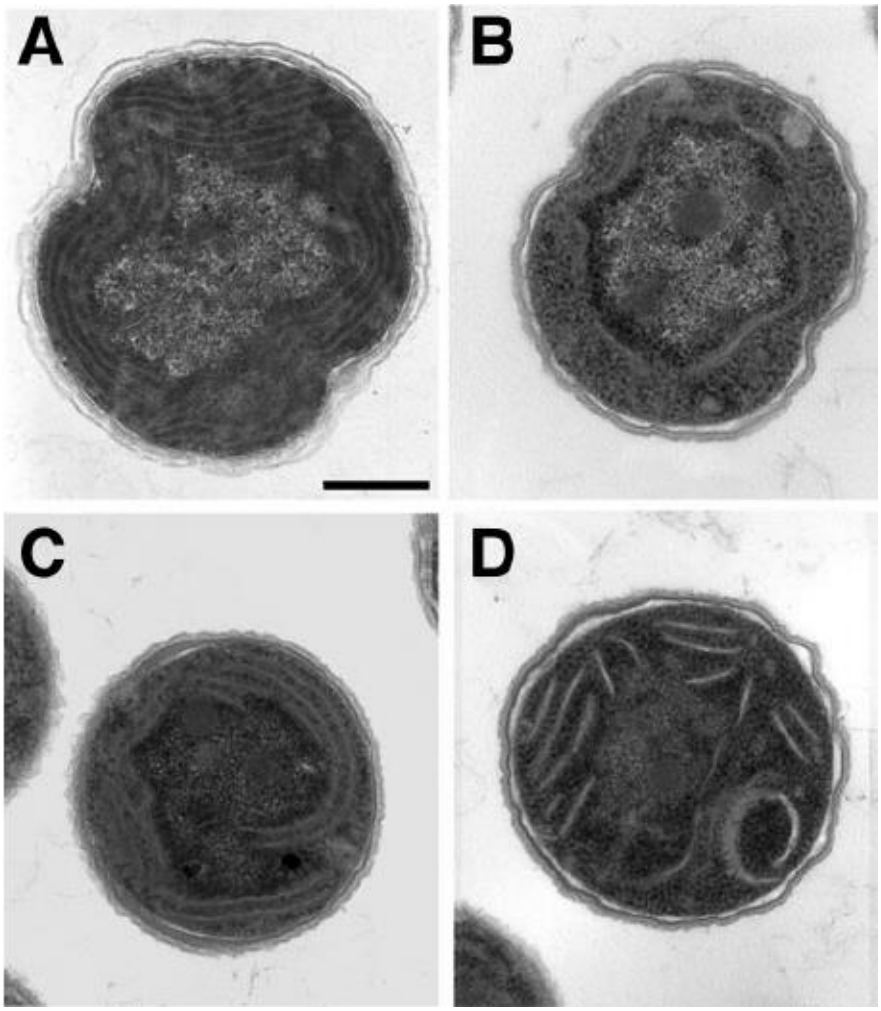

Figure 1.4. Transmission electron microscopy of *Synechocystis* 6803 cells. A. wild-type cells grown aerobically under medium light conditions. B. mutant cells grown aerobically under medium light intensity. C. mutant cells grow aerobically under low light intensity. D. mutant cells grown microaerobically under medium light conditions. Scale bar is 500 nm. Reproduced under the terms of the Creative Commons CC-BY license (Sobotka et al. 2008).

As a model organism, numerous studies have been conducted to reveal *Synechocystis* 6803 physiology under both nutrient "replete" and "deplete" conditions, as well as its metabolic responses to various environmental factors (Battchikova et al. 2010; Xu et al. 2008). *Synechocystis* 6803 can conduct oxygenic photosynthesis and CO_2 fixation

processes. Moreover, *Synechocystis* 6803 is a naturally competent strain which made genetic modification possible via recombination (Zang et al. 2007). Synthetic biology has propelled the development of various genetic and molecular biology tools tailored for model microbial hosts like *E. coli* and *S. cerevisiae*. Similarly, comparable tools were designed for *Synechocystis* 6803, enabling genetic manipulation at multiple levels including transcriptional, translational, and posttranslational regulation. A comprehensive understanding of cell-wide metabolism of *Synechocystis* 6803 is necessary. To achieve this, high-throughput "omics" tools such as transcriptomics, proteomics, and metabolomics have been extensively utilized to analyze the dynamic processes of *Synechocystis* 6803 under various physiological conditions (Nakajima et al. 2014; Pathania et al. 2022).

This dissertation focuses on photosynthetic complex PSI-IsiA, in *Synechocystis* 6803. Its isolation, purification, functional characterization and structural determination.

Spectroscopy of Photosynthetic Systems

As we have mentioned, plants, algae and cyanobacteria excel in capturing light energy and utilizing it in photosynthesis. The initial process of photosynthesis starts with the absorption of light by pigment molecules, which reside in thylakoid membraes in cyanobacteria or plant chloroplasts.

Within the thylakoid membranes of photosynthetic organisms, four membrane complexes play crucial roles in the light reactions of photosynthesis. Among these, PSII and PSI utilize light to initiate a sequence of electron transfer events. In photosynthetic organisms, various chlorophylls (Chl) such as a, b, c, d, and f, along with carotenoids, have been identified as the primary sources of light absorption, each possessing distinct

spectroscopic properties. (Blankenship and Blankenship 1992b). The term "chlorophyll" originates from two Greek words: "khloros," meaning pale green, and "phyllon," meaning leaves. Plants contain chlorophyll a and b as their only primary chlorophylls. Most cyanobacteria contain Chl a as the only chlorophyll type, however some cyanobacteria contain multiple types of Chls, such as chlorophyll c and d (Blankenship 2021).

The chlorophyll molecule comprises a central magnesium (replaced by Zinc in some rare cases) atom ligated by four nitrogen-containing pyrrole rings, forming a porphyrin (tetrapyrroles). All chlorophyll molecules contain an additional fifth ring and are differentiated by several modifications around their ring systems (figure 1.5).

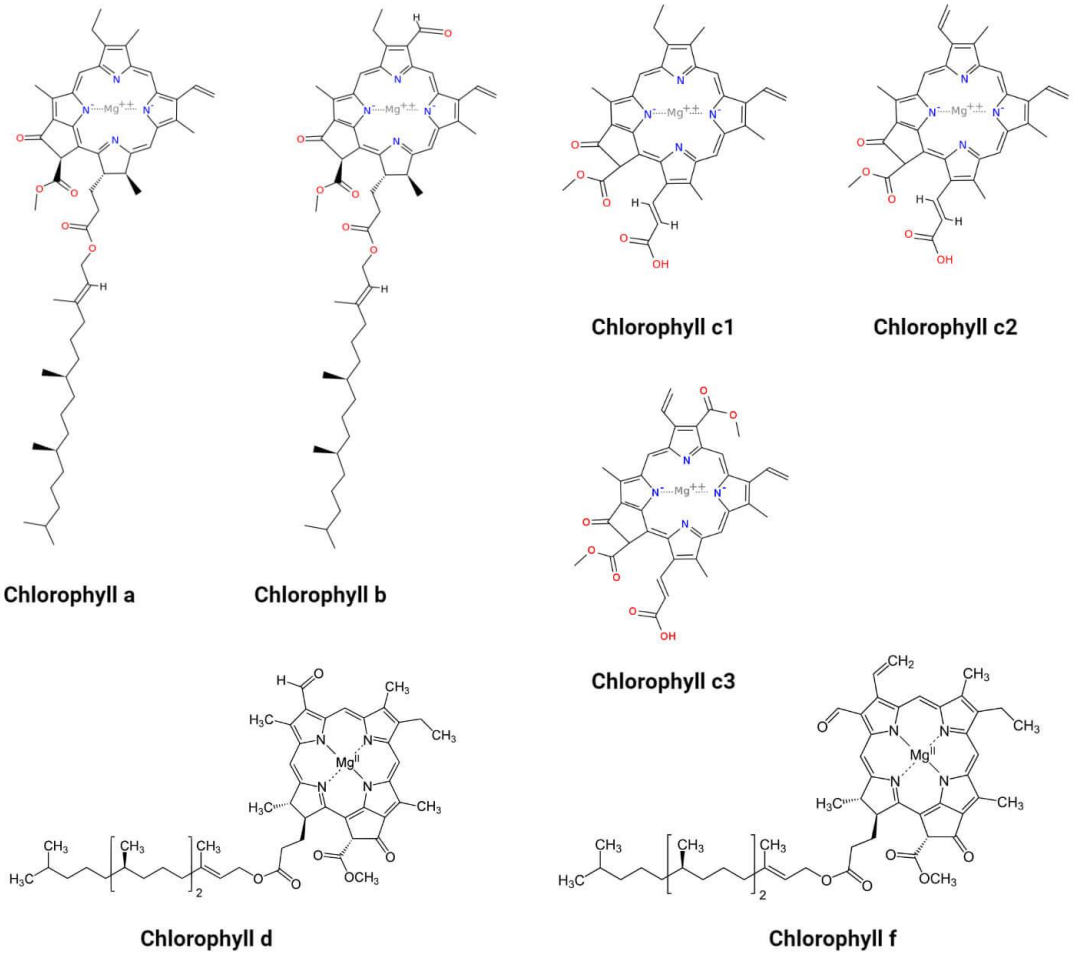

Figure 1.5. Chemical Structures of Chlorophylls, Chlorophyll e is reserved for a pigment that has been extracted from algae in 1966 but not chemically described. The structure of chlorophylls a-f are shown here, different sidechain modifications on chlorophyll structures found in nature (Wikipedia contributors 2024).

Chlorophyll a (Chl a) stands as the most widely distributed type of chlorophyll, present in all living organisms capable of oxygenic photosynthesis (Figure 1.5 and 1.6). Chl a primarily absorbs wavelengths in the blue-violet and orange-red regions of the light spectrum, while reflecting yellow-green light. This absorption and reflection pattern contributes to the green coloration observed in Chl containing organisms. Notably, an important epimer known as Chl a', differing from Chl a solely in stereochemistry at the C-13 position, exists. Chl a' is exclusively found in the P700 reaction center, forming the special chlorophyll pair to conduct charge separation (Blankenship 2021).

Chlorophyll b (Chl b) differs from Chl a only at the C-7 position of ring B (Figure 1.5). In Chl b, this position features a formyl group, inducing a blue shift in the absorbance maximum compared to Chl a. While Chl b is prevalent in most plants and green algae, it is exclusively found in the prochlorophytes within the cyanobacteria clade (Blankenship 2021).

Chlorophyll c (Chl c) stands out as the most distinctive among all chlorophylls found in oxygenic photosynthetic organisms. Unlike other chlorophyll derivatives, it lacks a tail and consists only of the tetrapyrrole ring (Figure 1.5). Additionally, ring D is not reduced in Chl c, and various structural variations exist (Blankenship 2021). Chlorophyll c1, c2, c3 are prevalent types of chlorophyll c distinguished by the presence of a special group at the C-8 position (Figure 1.5).

Chlorophyll d (Chl d) closely resembles Chl a, except for the C-3 position, which is occupied by a formyl group. (Figure 1.5) The formyl group on ring A induces a red shift compared to Chl a, contrary to the blue shift observed in Chl b on ring B. Chl d has only been identified in cyanobacteria (Blankenship 2021).

Chlorophyll f (Chl f) also features a formyl group on ring A, but it is located at the C-2 position, resulting in a larger red shift compared to Chl d, with a maximum absorption at 706 nm Like Chl d, Chl f has only been identified in cyanobacteria (M. Chen et al. 2010). In this dissertation, we mainly focus on chlorophyll a because it's the only chlorophyll within *Synechocystis* 6803.

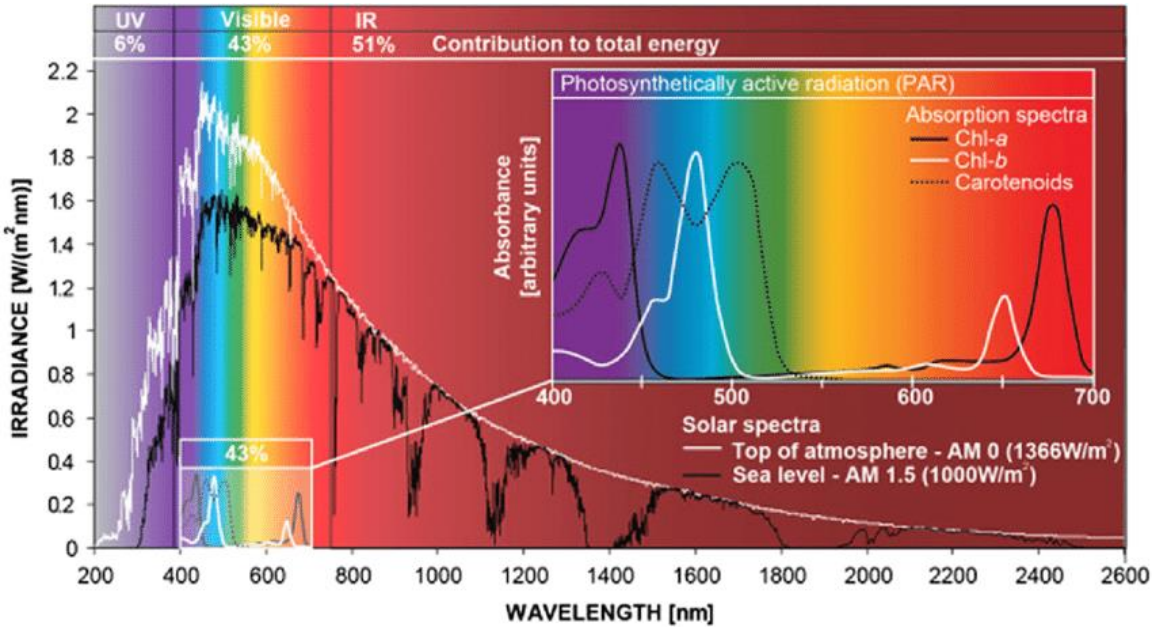

Figure 1.6. Terrestrial solar irradiance and photosynthetic absorption spectra. Standard solar spectra at the top of the atmosphere are depicted in white, while those at sea level are represented in black. The inset focuses on the absorption from major light harvesting pigments, chl-a, chl-b and carotenoids within photosynthetic organisms. Reprinted from "Can photosynthesis enable a global

transition from fossil fuels to solar fuels, to mitigate climate change and fuel-supply limitations?" (Ringsmuth, Landsberg, and Hankamer 2016).

Light, a form of electromagnetic radiation, traverses in wave form, embodying a unique energy.

The sun emits a broad spectrum of wavelengths, including those within the visible range, spanning approximately 300 nm to 2600 nm (Figure 1.6). The visible spectrum encompasses the range of electromagnetic radiation visible to the human eye, with wavelengths falling between approximately 400 nm to 700 nm. Photosynthetic organisms appear green to our eyes because the pigments they contain strongly absorb most wavelengths within the visible range, except for those in the green region. Similarly, the other pigment, carotenoid mainly absorbs the green and blue light except for the red and orange region (Figure 1.6).

As we have mentioned, different wavelengths of light have particular energy associated with it. Not all light could be absorbed because the atom can only absorb specific amounts of energy. As a molecule, the photosynthesis' pigments discussed earlier selectively absorb particular wavelengths of light (Figure 1.6). To understand the principles of absorption effectively, a simplified diagram can be used (Figure 1.7).

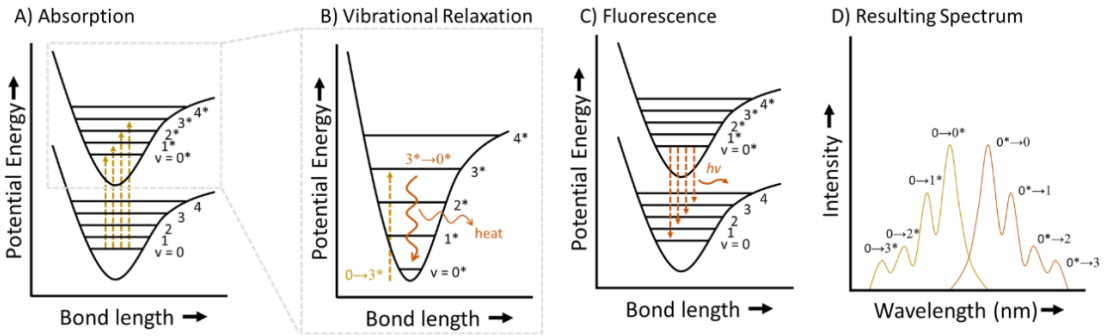

Figure 1.7. Schematic Potential Energy Diagrams and Spectra for Energy Transitions. (A) depicts an absorption diagram illustrating the transition from the ground electronic and vibrational state to an excited electronic and excited vibrational energy level. (B) illustrates vibrational relaxation, which occurs following an equilibration period where the excited molecule relaxes to the ground vibrational state of the excited electronic state. (C) showcases fluorescence, which arises from the ground vibrational state of the excited electronic energy level. The molecule then relaxes to a vibrational energy level within the ground state electronic energy level, emitting a photon in the process. (D) presents theoretical absorption and fluorescence spectra corresponding to the examples in (A) and (C) (Dobson 2022).

In Schematic Potential Energy Diagrams (Figure 1.7), an electron in the ground state electronic and vibrational energy level (v = 0) absorbs a photon of light, becoming excited to a higher vibrational mode within the excited electronic energy level (v = 0 → v = 1*, 2*, or 3*) (Figure 1.7A). Subsequently, the energy of the photon will be transferred to a particular electron within 10^{-15} seconds. We showed 4 possible absorption transitions in this schematic diagram. Once an electron becomes excited, it can dissipate its energy through various pathways (Figure 1.7BD). One well-known pathway is vibrational relaxation, which is a non-radiative process depicted on this diagram as a small arrow between vibrational levels within the excited state electronic energy well (v = 0*). During vibrational relaxation, the energy initially absorbed by the electron from the photon is dissipated as heat and the electron relaxes back to the ground state vibrational energy level. Vibrational relaxation is a rapid process, occurring within the timescale of 10^{-14} to 10^{-11} seconds, making it highly likely to occur immediately following absorption. (Figure 1.7B). Another pathway to return to the ground state electronic energy level is emitting a photon equivalent to the energy gap distance (Figure 1.7C). This process is called

fluorescence, which is a slower pathway on the order of 10^{-9} to 10^{-7} seconds. This emitted photon, detected in fluorescence measurements, leads to the formation of a simple spectrum (Figure 1.7D). Fluorescence is predominantly observed between the first excited electron state and the ground state of a molecule (Figure 1.7D). This preference arises because at higher energy levels, it becomes more probable for energy to dissipate through vibrational relaxation processes. Notably, fluorescence is observed to be red shifted compared to absorption, a phenomenon known as a Stokes shift. Alternatively, energy loss can occur through processes like vibrational or electronic-translational collisional interactions with surrounding atoms or molecules. In cases where the emitted photon has less energy than the absorbed photon, the difference in energy between the absorbed and emitted photons is known as the Stokes shift. This shift represents the energy lost by the system during relaxation from the excited state to the ground state (Figure 1.7D).

While this simplified diagram illustrates only a few transitions, molecules exhibit far greater complexity and may interact with each other, resulting in an infinite number of unique transitions that contribute to broad spectra representing an average of all transitions. In this dissertation, we will use a series of spectroscopy techniques, including absorption and fluorescence, to study the structure-function relationships in photosynthetic energy conversion.

Spectroscopy investigates how electromagnetic radiation interacts with matter, enabling scientists to explore the structures of quantized energy levels. A range of spectroscopic techniques have been employed to understand photosynthetic systems. Ultrafast spectroscopy, including fluorescence upconversion and transient absorption, has been used to investigate excitation energy transfer and electron transfer in these systems. (Jimenez and Fleming 1996). Time-resolved spectroscopy has revealed the presence of an intermediate species in the energy transfer chain of PSI (Sparrow et al. 1990). Ultrafast

infrared spectroscopy has provided new insights into the photo-dynamics of photosynthetic complexes, including energy transfer and electron transfer processes (Di Donato and Groot 2015).

Kinetics of the $P700^+$ signal

The oxidation-reduction potential of P700, a key component of PSI in photosynthesis, has been extensively studied. People have found that the midpoint potential of P700 is around +490 mV in chloroplast lamellae and sub-chloroplast particles. In this paper P700 was found to be half-oxidized at ferricyanide/ferrocyanide ratios of about 60 at 21°C (Setif and Mathis 1980). In 1988, another group found the observed kinetic changes at 830 nm in response to single turnover or multiple turnover saturating flashes are practically identical to those previously measured around 700 nm, providing a practical tool for plant physiological research (Schreiber, Klughammer, and Neubauer 1988). Generally, via monitoring the oxidation state of the primary donor P700 of PSI at infrared absorption spectroscopy (830 nm), energy-transfer related information could be found on PSI-related photosynthetic electron transport in vivo (Klughammer and Schreiber 1998).

By using a Joliot-type spectrophotometer, the induction kinetics of P700 oxidation upon illumination could be observed. In high light conditions, photosynthesis is primarily limited at the level of the Calvin cycle. Electron carriers preceding this cycle should ideally be in a reduced state. However, under intense light, P700, a critical component involved in PSI, becomes oxidized. This observation indicates the presence of a regulatory mechanism that restricts the rate of electron flow before reaching P700 (Alric, Lavergne, and Rappaport 2010; Joliot and Johnson 2011).

Ultrafast spectroscopy

Ultrafast spectroscopy techniques use sequences of ultra-short light pulses to study photo-induced dynamical processes in atoms, molecules, nanostructures and solids. (Maiuri, Garavelli, and Cerullo 2019) Ultrafast spectroscopy can be applied to studies of excitation energy transfer in light harvesting complexes and electron transfer in bacterial reaction centers (Jimenez and Fleming 1996). Energy transfer within a photosynthetic membrane typically occurs over a timescale ranging from less than 100 femtoseconds (fs) to hundreds of picoseconds (ps) (van Amerongen and van Grondelle 2001). Simulations analyzing protein structures can aid in clarifying ambiguous and incomplete experimental results to identifying underlying rules to create efficient light-initiated charge separation at high efficiency (Gunner 2008).

One of the most important ultrafast spectroscopy techniques is transient absorption spectroscopy. The initial stages of the photosynthetic process occur after the absorption of a photon by an antennae system. This system functions to harvest light energy and subsequently transfer it to the reaction center (Nelson et al. 2015). The high time resolution, typically below 50 femtoseconds (fs), has enabled the real-time investigation of the early events occurring within a light-harvesting antennae (Sundström 2008).

Time-resolved fluorescence spectroscopy, a powerful ultrafast spectroscopy tool for studying molecular interactions and dynamics, has seen significant advancements in recent years. Time-resolved fluorescence spectroscopy was performed with Photosystem particles isolated from a series of species with widely varying antennae sizes (Mullineaux et al. 1993). However, not only the thylakoid itself or isolated complexes can be used in these measurments, a few groups have utilized time-resolved fluorescence spectroscopy in cyanobacteria cells to understand ultrafast photosynthetic kinetics (Akimoto et al. 2012; Chukhutsina, Holzwarth, and Croce 2019; Mullineaux et al. 1993). In this dissertation, we

used time-resolved fluorescence spectroscopy to measure the kinetics of an antennae mutant in *Synechocystis* 6803 to reveal its interesting dynamics in PSI-IsiA system.

In recent years, two ultrafast kinetic techniques have been employed to study complex fluorescence kinetics in biological samples: "time-correlated single photon counting" (TCSPC) and streak camera technique. Each method offers distinct advantages and disadvantages.

TCSPC, also known as single-photon timing (SPT), boasts the highest sensitivity and the largest dynamic range, spanning over 4–5 orders of magnitude in both time and amplitude. This wide dynamic range is particularly advantageous for analyzing intricate kinetics. TCSPC also allows for very low excitation intensities, crucial for maintaining distinct photosynthetic states, such as measuring with open PSII RCs. However, TCSPC typically has a lower time resolution compared to the streak camera technique, with resolutions around 2–3 ps in the best instruments, as opposed to sub-ps resolution using a streak camera. Additionally, in typical TCSPC instruments, each decay wavelength is measured separately, although some designs enable simultaneous recording of kinetics at several wavelengths, albeit at the expense of time resolution.

In the other hand, the streak camera typically records the entire spectral-kinetic surface at once, offering higher intrinsic time resolution compared to TCSPC, although at the cost of a substantially lower dynamic range in both time and amplitude. For measuring intact photosynthetic tissue, the highest time resolution is not usually required, making resolutions of a few picoseconds sufficient. However, the complexity of kinetics necessitates very high signal-to-noise ratios and dynamic ranges, which TCSPC often provides more effectively than the streak camera system. Therefore, in general, a well-designed TCSPC instrument offers several advantages over the streak camera system for the measurement of complex fluorescence kinetics.

After the measurement, the measured fluorescence decay traces were globally analyzed using multiple parallel, non-interacting decays. Global analysis fits measurments over multiple emission wavelengths using identical decay times to achieve higher confidance in the fit result. The experimental kinetics function, denoted as $\mathrm{I}(\lambda, \mathrm{t})$, was fitted as follows:

$$\mathrm{I}(\lambda, \mathrm{t}) = \sum_{i}^{n} \alpha_{\mathrm{i}}(\lambda) \exp\left(\frac{-t}{\tau_{\mathrm{i}}}\right)$$

DAS (Decay-Associated Spectra) represents the amplitude factor linked to decay component i with a decay lifetime of τ. In this dissertation we used global analysis in Chapter 3 to analyze TCSPC measurments done on whole cells.

Iron limitation in the ocean.

Cyanobacteria play a crucial role as primary sources of oxygen and as nitrogen-fixing agents in aquatic environments. Figure 1.8 illustrates the average ocean chlorophyll concentration measured by SeaWiFS since its launch. This measure can be used to estimated the abundance of photosynthetic organisms in ocean waters. The image highlights the interconnectedness between physical and chemical ocean processes, such as temperature variations and nutrient upwelling from the deep ocean near coastlines, and the presence of oceanic plant life. Chlorophyll concentrations, and consequently the level of photosynthetic organisms, tend to be higher in coastal regions compared to open ocean areas. Additionally, they are generally higher in the northern oceans compared to the southern ones.

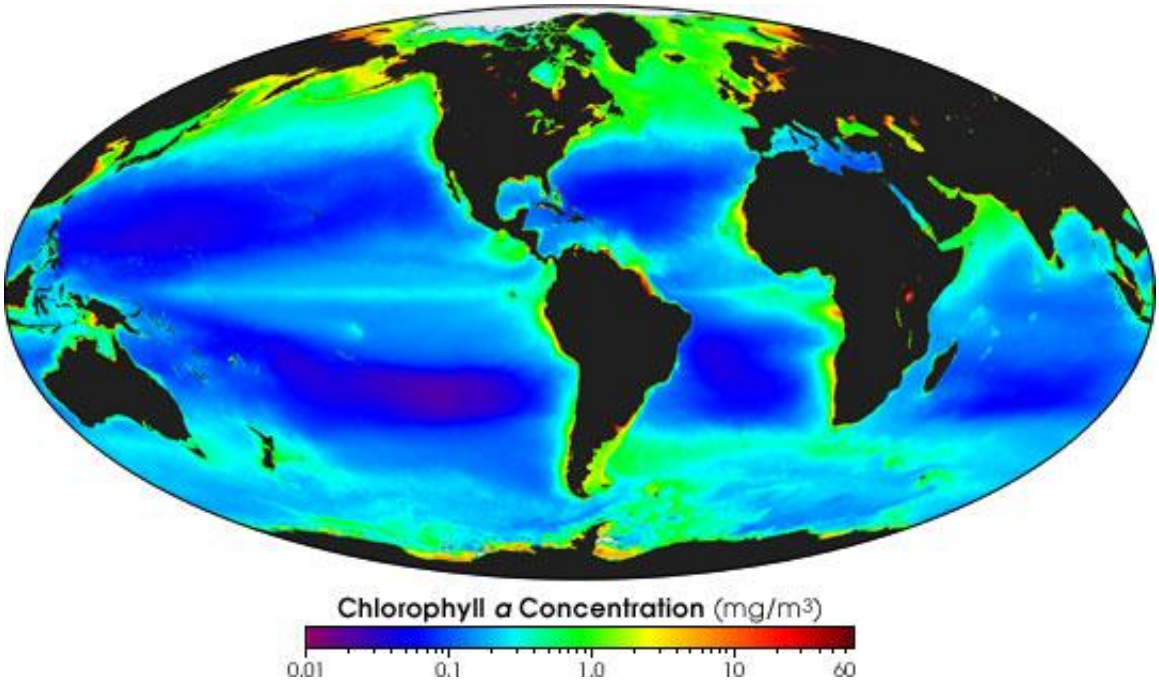

Figure 1.8. Chlorophyll α concentration map in 1997 from NASA. Data was collected by the Sea-viewing Wide Field-of-View Sensor (SeaWiFS).

More than 50% of global primary production takes place in the ocean. However, compared to laboratory conditions, iron is more likely to get oxidized and limited in the ocean (Figure 1.9). Figure 1.9 highlights the importance of iron stress in the ocean. This underscores the necessity for photosynthetic organisms to develop survival strategies in iron-limited environments.

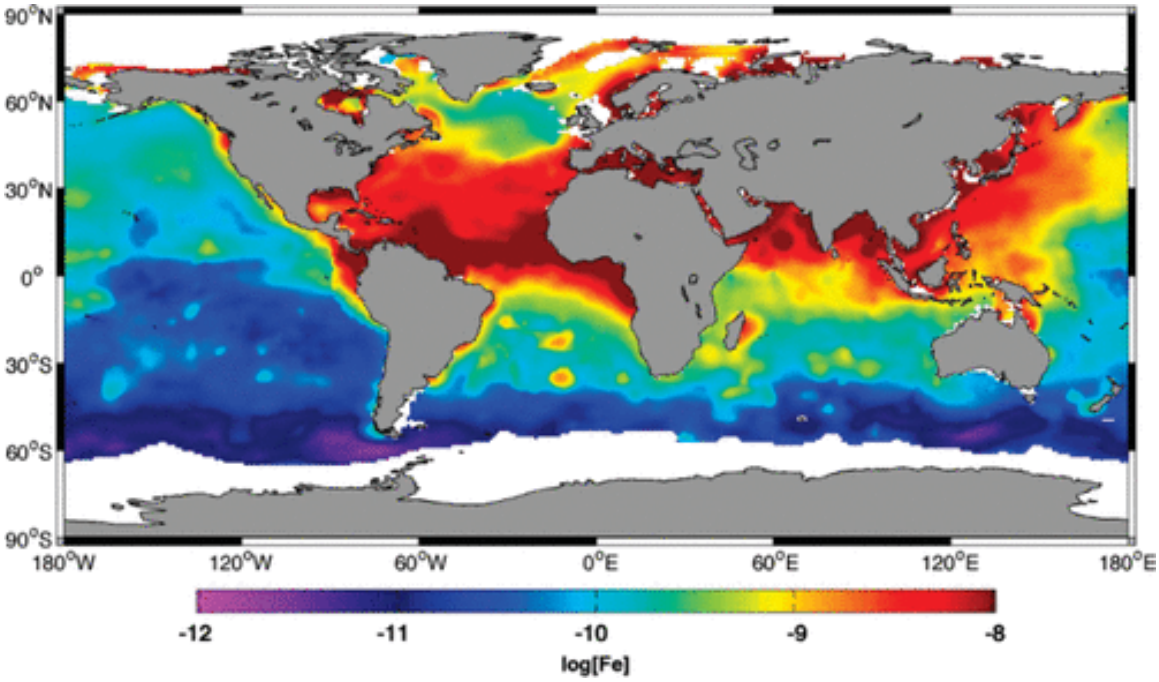

Figure 1.9. The global distribution of iron (Fe) in the world's oceans reveals a pattern where cooler colors represent low Fe levels, typically associated with regions of reduced photosynthetic activity. Conversely, warmer colors indicate higher concentrations of Fe, predominantly found in coastal oceans, upwelling regions of the Atlantic and Eastern Pacific Oceans, and areas with significant aeolian dust supply from the Sahara and Gobi Deserts. These warmer color regions generally correspond to areas of elevated photosynthetic activity. Reprinted with permission from (Chauhan et al. 2011)

To adapt low-iron environments, cyanobacteria express IsiA, a PSI antennae, critical to their survival. In this dissertation, we aimed to understand the regulation of the interactions between IsiA and PSI.

Introduction to Cryo-EM

The history of the electron microscope is a testament to the ingenuity and collaboration of scientists and engineers over the years. It began in 1926 when Hans Busch developed

the first electromagnetic lens, laying the foundation for focusing electron beams. Ernst Ruska and Max Knoll then built the prototype electron microscope in 1931, followed by Ruska's creation of the first transmission electron microscope in 1933. Throughout the 1940s and 1950s, advancements continued, leading to the development of the scanning electron microscope by Manfred von Ardenne in 1938 and improvements in resolution and sample preparation techniques. Commercial production began in the 1950s, with companies like Siemens and Philips leading the way. In 1986, Ruska was awarded the Nobel Prize in Physics for his contributions to electron optics and the invention of the electron microscope. Today, electron microscopes remain indispensable tools in various fields, enabling researchers to study materials at the atomic scale and beyond, driving innovation and discovery.

Cryo-electron microscopy (cryo-EM) is a powerful imaging technique used to visualize biological macromolecules at near-atomic resolution. It involves rapidly freezing a thin film of the sample in a vitrified ice layer to preserve its native structure. This method has revolutionized structural biology by providing detailed insights into the three-dimensional architecture of proteins, nucleic acids, and their complexes. In 1968, First 3D reconstruction from the electron micrograph appears by David DeRosier & Aaron Klug on Bacteriophage T4 (Nogales 2016). As a basis of cryo-EM, people realized that 3D reconstruction make it possible to solve the structure by collecting data from electron microscope. 1974, known as golden year of cryo-EM, group of Unwin & Henderson start to use membrane crystals with sugar embedding which made the structure into atomic resolutions (Henderson and Unwin 1975; P. N. T. Unwin and Henderson 1975). Same time Parsons group use hydrated specimens under electron beam illumination in the EM column. Taylor & Glaser group introduce plunge freezing as a significant tool for sample preparation in cryo-EM (Figure 1.10).

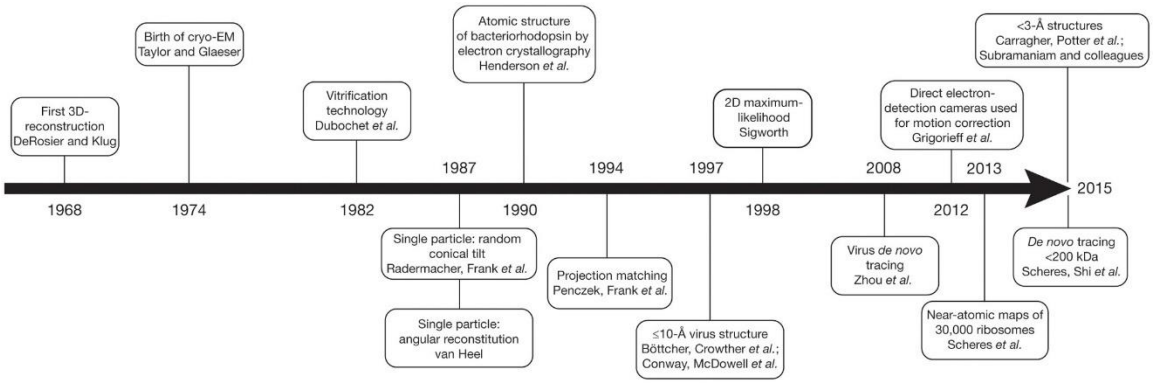

Figure 1.10. The development of cryo-EM into a mainstream structural biology technique. Reprint with permission from (Nogales 2016)

Vitrification refers to the rapid cooling of a liquid sample, typically containing biological molecules or complexes, to form an amorphous solid without the formation of ice crystals. This process is crucial for preserving the native structure of the sample, as ice crystals can disrupt the delicate molecular architecture and introduce artifacts during imaging (Dubochet et al. 1988). The technology of vitrification has revolutionized cryo-EM by enabling the visualization of biological specimens at high resolution and in their near-native state, leading to significant advances in structural biology and our understanding of complex biological processes.

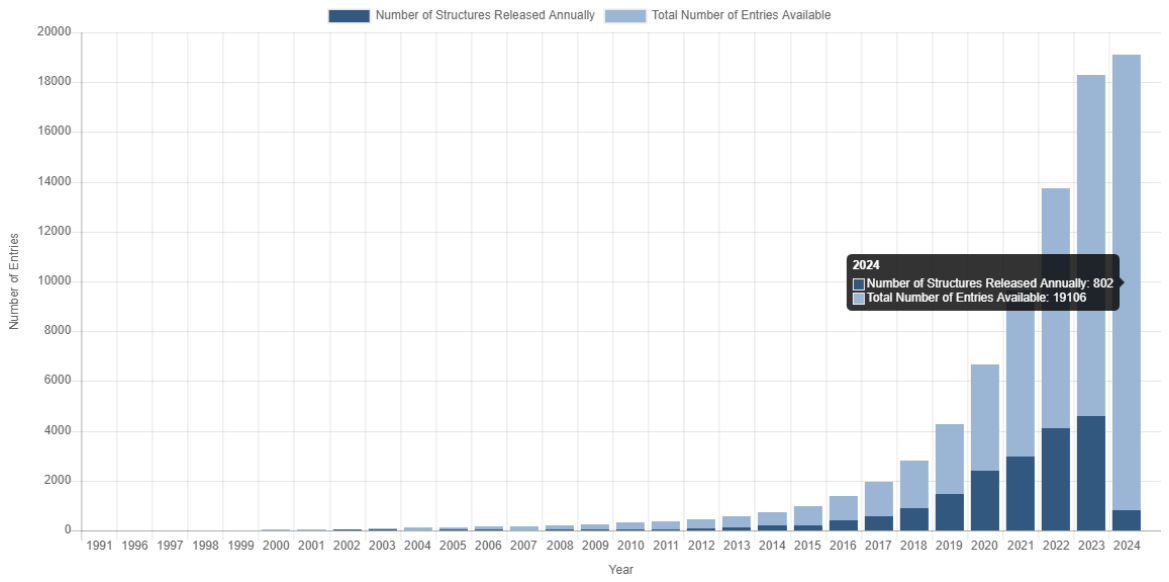

Figure 1.11. Growth of Structures Solved by Electron Microscopy to the PDB released per Year. From 2020, numerous structures and entries became available on pdb. Statistics retrieved on 4 March, 2024 from http://www.rcsb.org

From 1990, the first atomic structure of bacteriorhodopsin by electron crystallography (Henderson et al. 1990), a great number structures were solved in resolutions that near atomic resolution. Figure 1.11 illustrates the growth numbers of structures solved by electron microscopy.

X-ray crystallography, NMR and cryo-electron microscopy (cryo-EM) are powerful techniques for determining protein structures, each with its own advantages and limitations. X-ray crystallography requires crystallized samples and provides high-resolution structures of proteins in their crystal state, requiring the supply of phases for structure determination. In contrast, cryo-EM allows for the visualization of protein structures in near-native conditions without the need for crystallization, overcoming size limitations observed in nuclear magnetic resonance (NMR) spectroscopy. Cryo-EM also offers the advantage of observing phases from images, although there are still limitations

on the size of proteins that can be resolved. Additionally, free electron lasers offer larger beam tolerance but also require crystal samples and phase supply, while NMR spectroscopy determines solution structures close to native conditions but is limited by size constraints. Each method contributes uniquely to the understanding of protein structure and function, with cryo-EM increasingly recognized for its ability to provide native-like structures of larger protein complexes (Dubochet et al. 1988; Keeler 2010; Thompson, Maskery, and Leach 2016).

In this dissertation, we utilized cryo-EM as our primary method to solve PSI-IsiA structure.

Cryo-EM Workflow

The typical workflow for determining the structure of a protein using cryo-EM include protein purification, sample preparation, cryo-EM data collection, image processing and structure determination (Y. Cheng 2015). Initially, cyanobacteria cells are cultured and PSI-IsiA supercomplex is isolated and purified.

In electron microscopy, preparing biological specimens involves several crucial steps. First, the specimen must be stabilized within the high vacuum environment of the electron microscope column to ensure its integrity during imaging. Additionally, it's essential to preserve the biological sample in a hydrated condition to maintain its natural state as much as possible. Furthermore, measures must be taken to prevent radiation damage to the specimen caused by the electron beam. Finally, various techniques are employed to enhance the quality or contrast of the image obtained from the specimen(Y. Cheng 2015; Murata and Wolf 2018) .Therefore, EM grids technique is prepared. To prepare an EM copper grid with a thin amorphous carbon film, a multi-step process is followed to ensure optimal conditions for sample mounting and imaging in electron microscopy. (Figure 1.12) Initially, a thin carbon film is deposited onto the copper grid, serving as a substrate for the

biological sample. However, due to the inherent hydrophobicity of the carbon film, evenly depositing solutions onto its surface can be challenging. To address this issue, residual air and gas particles are eliminated through glow discharge treatment, temporarily altering the surface properties of the carbon film to become hydrophilic. This treatment allows for more effective deposition of aqueous solutions or biological samples onto the carbon-coated grid. Overall, this method ensures that the EM grid is adequately prepared, providing a suitable platform for sample visualization and analysis in electron microscopy studies (Glaeser 2018; Palovcak et al. 2018).

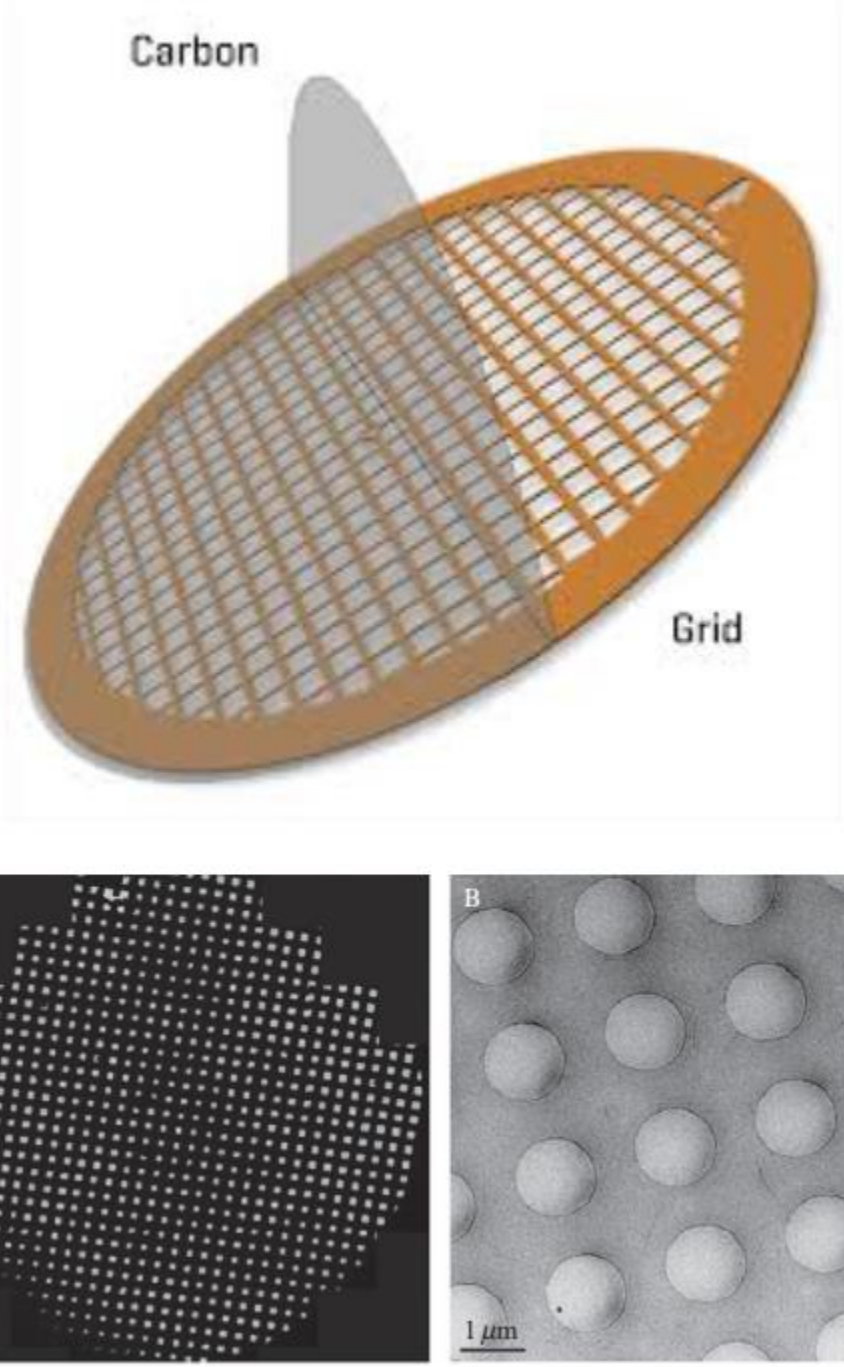

Figure 1.12. A schematic image of a grid, a carbon film was attached on the copper EM grid. A: a grid carbon film under 40x microscope. B: a grid carbon film under electron microscope. One rule bar stands for 1 μm.

When preparing samples for electron microscopy (EM), several factors must be carefully considered to ensure optimal results. First and foremost is the choice of preservation medium, which should maintain the integrity of the biological specimen. Buffer conditions play a crucial role in preserving the native state of the sample and must be carefully optimized. Glycerol or polyethylene glycol (PEG) should be avoided due to their potential interference with imaging. Trehalose and glucose are preferred for their contrast-matching properties, particularly suitable for 2D crystal samples. The distribution of the object within the sample, as well as its density and homogeneity, are important considerations for achieving high-quality images. Ice thickness, object size, and the electron dose applied during imaging are additional factors that need to be carefully controlled to obtain accurate and detailed results.

Water vitrification refers to the rapid cooling of water-containing samples to such low temperatures that instead of forming ice crystals, the water transitions into a glass-like or vitreous state. For water to vitrify effectively, the temperature drop rate must exceed 10^5 - 10^6 Kelvin per second (Dubochet et al. 1988). When it comes to biological specimens, the cooling rate needs to be even faster, ranging from 5×10^3 to 2×10^6 Kelvin per second. Liquid ethane presents itself as a suitable alternative for cryo-vitrification due to its comparable melting temperature to liquid nitrogen but with a higher specific heat capacity. (Dubochet et al. 1988) A plunge freezing robot was designed to vitrificated water. (Figure 1.13) In conclusion, vitrification encompasses several key factors that influence the successful preservation of specimen in a vitreous state for imaging. These factors include the speed at which the sample is plunged into the cryogen, the duration of blotting and draining to remove excess liquid, the type of blotting surface used, the temperature of the cryogen, and the humidity of the surrounding environment. (Figure 1.14) Optimizing these parameters is essential to achieve rapid cooling of the sample, prevent ice crystal

formation, and maintain the native structure of biological specimens, ultimately enabling high-resolution imaging in cryo-EM studies (N. Unwin and Fujiyoshi 2012).

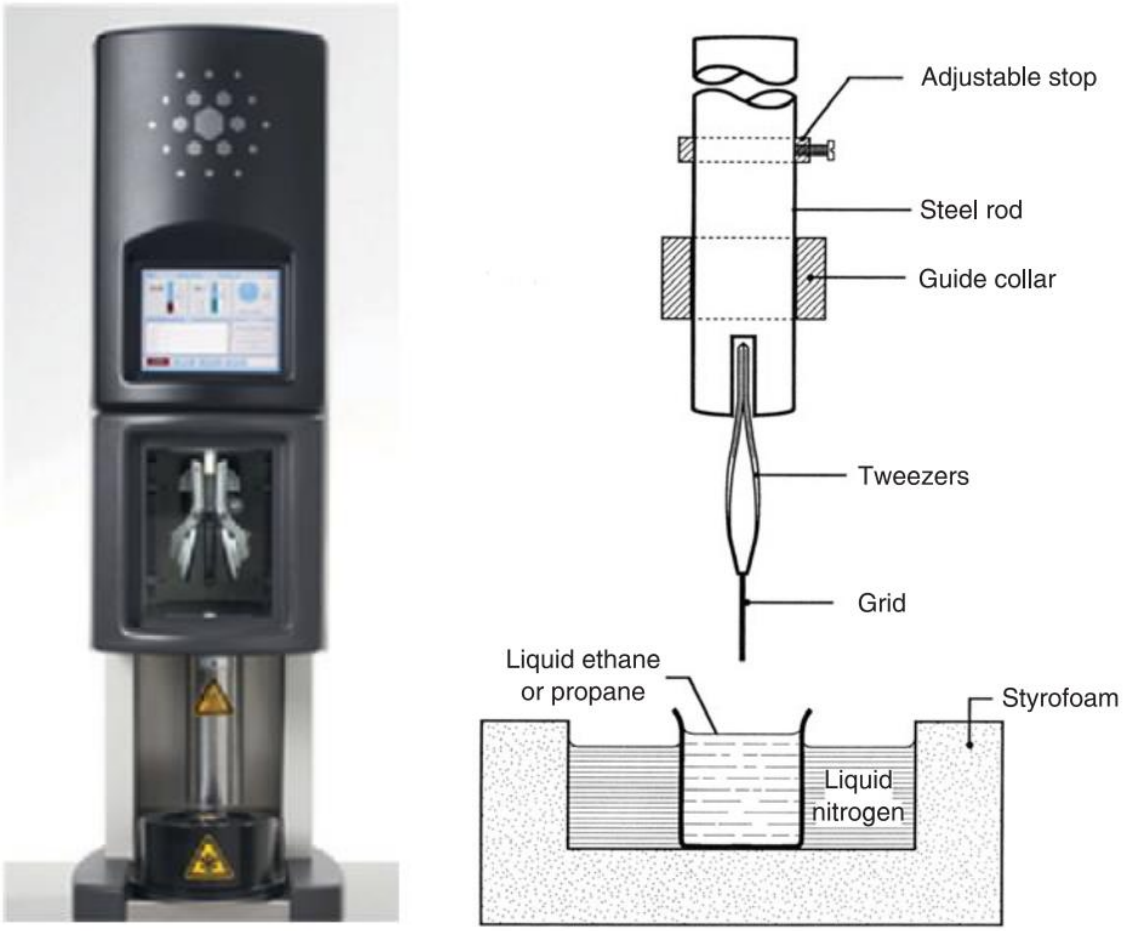

Figure 1.13. A plunge-freezing robot in ASU and a schematic image of how plunge freezing worked. Reprint with permission from (Mitra and Frank 2006).

Advantages of cryo-EM include its ability to preserve biological specimens in their native state, providing high-resolution structural information without the need for sample staining or fixation. Additionally, cryo-EM allows for the visualization of dynamic processes and heterogeneous samples. However, there are also several disadvantages to consider. The ice used to preserve the specimen is highly sensitive to radiation damage, necessitating

low-dose imaging techniques to minimize sample degradation. Furthermore, cryo-EM images often exhibit low contrast and signal-to-noise ratio (SNR), requiring sophisticated image processing techniques for data interpretation. Another challenge is the preparation of cryo-EM grids, which can be complex and not always reproducible, leading to variability in sample quality and data acquisition.

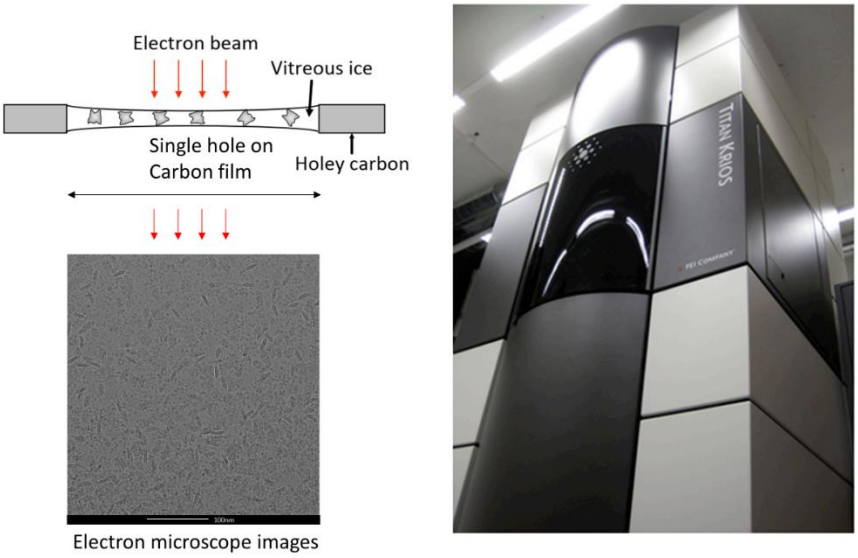

Figure 1.14. The schematic illustrates the process of preparing biological specimens on grids. After the specimen is placed on the grid, it is rapidly cooled by plunging into liquid ethane through the small hole in the carbon film. This rapid cooling results in the formation of thin, vitreous ice, preserving the specimen's structure. Subsequently, electron beams are directed onto these samples to capture images. The right side of the image shows a Titan Krios transmission electron microscope (Thermo Fisher – FEI), the equipment used for imaging the prepared specimens.

EM imaging involves several critical parameters that need to be carefully adjusted to achieve optimal imaging conditions. These parameters include dosage, magnification, defocus, beam alignment, and detector settings. Dosage refers to the amount of electron dose applied to the sample during imaging. It must be carefully controlled to avoid radiation damage while still providing sufficient signal for image acquisition. Magnification determines the level of enlargement of the sample image. Higher magnification allows for detailed examination of smaller features but may also decrease the field of view and increase imaging time. Defocus refers to intentionally blurring the image by adjusting the focal plane. It is used to enhance contrast and improve resolution in electron microscopy imaging. Beam alignment ensures that the electron beam is properly focused and aligned with the sample. Precise alignment is crucial for obtaining clear and accurate images. Detector settings include parameters such as gain, exposure time, and pixel size, which affect the sensitivity and resolution of the imaging system. These settings must be optimized to maximize signal-to-noise ratio and achieve the desired image quality. Overall, careful adjustment of these parameters is essential for obtaining high-quality images in electron microscopy imaging, allowing for detailed visualization and analysis of biological specimens at the nanoscale(Bai, McMullan, and Scheres 2015; A. Cheng et al. 2018; Mitra and Frank 2006).

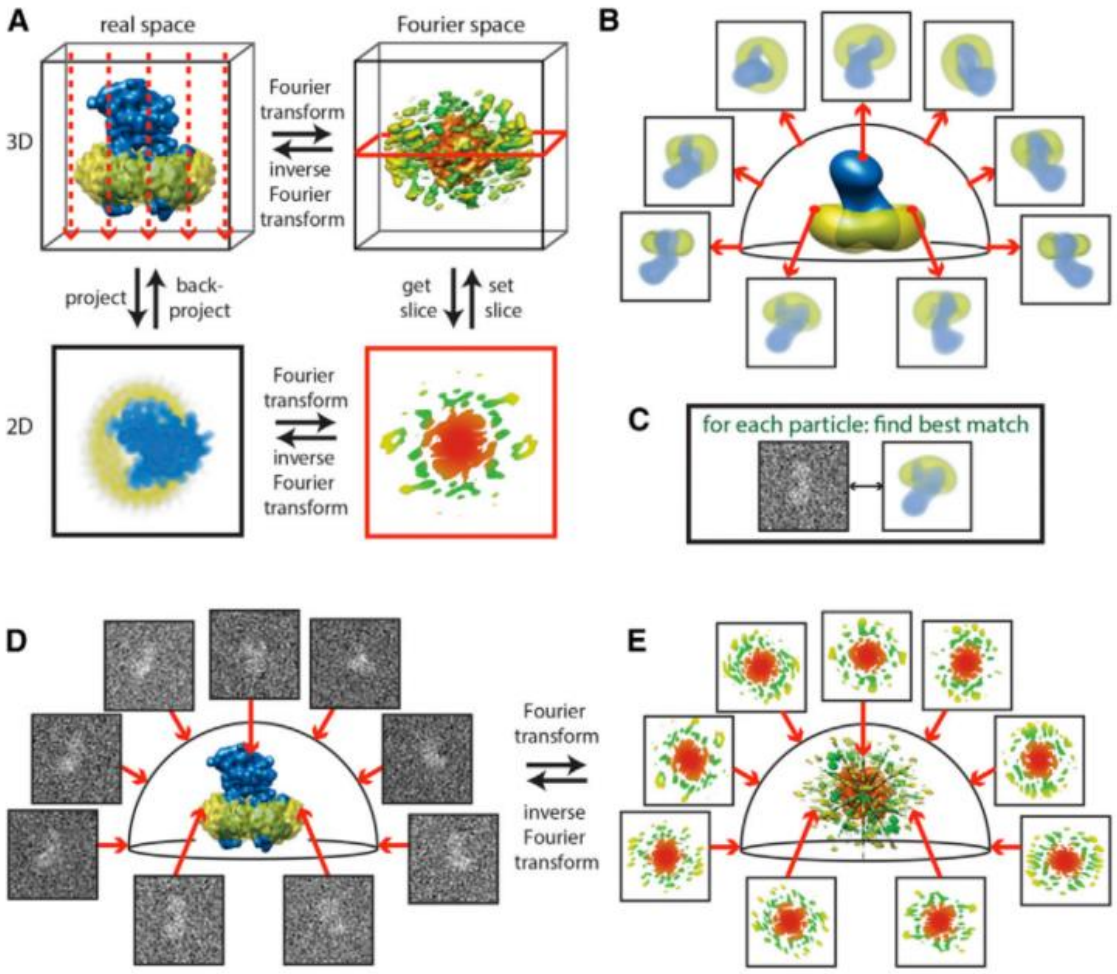

Figure 1.15. The basic process for image processing in cryo-EM. A: The projection-slice the two-dimensional projection of a three-dimensional object in real space corresponds to extracting a central two-dimensional slice from the three-dimensional Fourier transform of the same object. (B-E) The workflow of image process. Each experimental projection allows for the calculation of all experimental two-dimensional projections into a three-dimensional reconstruction through iterative procedures. Reprint with permission from (Nogales 2016).

Single-particle reconstruction in cryo-EM involves several key steps to generate high-resolution 3D structures from 2D projection images of individual particles. With the help of

new computer hardware and software, like Relion, data processing has dramatically advanced. (Fernandez-Leiro and Scheres 2017; S. H. W. Scheres and Scheres 2012; Zivanov et al. 2018) Specifically, software packages such as Cryosparc have played a crucial role in reducing computation time and introducing novel data processing techniques (Punjani et al. 2017). However, we mainly talk about the workflow from Relion in this dissertation. (Figure 1.15)

The process typically begins with motion correction in Relion. Motion correction involves aligning individual frames of a movie stack to correct for sample drift or beam-induced motion during data acquisition. This correction ensures that the images are properly registered, allowing for accurate reconstruction of the three-dimensional structure of the specimen (Baker and Rubinstein 2010; S. H. Scheres 2012, 2019).

The next step is to find contrast transfer function (CTF) correction, applied to compensate for imaging distortions caused by the electron microscopes optics. (Glaeser 2016; Li et al. 2013) CTF correction is applied to compensate for imaging distortions caused by the electron microscope's optics. Image alignment techniques are then used to correct for sample drift and particle orientation variations(Rohou and Grigorieff 2015) .

Then, image registration and particle picking, where individual particle images are identified and extracted from the raw micrographs. The main objective of manual particle picking is to ensure that the selected particle projections encompass the entire angle range and are evenly distributed across all angles. (Figure 1.15) Multiple software enables automated particle picking but it varies in different functions. In Relion, we choose Topaz (Bepler et al. 2019, 2020) using neural networks and positive-unlabeled learning to auto-pick particles on all micrographs from https://github.com/tbepler/topaz. Following by the first auto-picking, as a result, approximately 20-100 particles with similar orientations are obtained and averaged together, producing high-quality templates. These templates are

then utilized by the auto-picking algorithm, which is applied to the entire dataset, resulting in the selection of tens of thousands to millions of individual particles. (S. H. Scheres 2012) Initially, only a few classes from the auto-picking process may be distinguished from background noise. Subsequently, multiple rounds of two-dimensional classification are performed, gradually improving the resolution frequencies employed in each iteration by selecting additional particles oriented in different directions (S. H. Scheres 2012).

Subsequently, 3D image classification methods are employed to group similar particle images together based on structural features. Even after an initial selection for high-quality particles, datasets often exhibit heterogeneity. To address this issue, three-dimensional classification is employed, leveraging the low-resolution model generated earlier to assess how individual particles fit into it and categorize them into distinct classes. These classified images are then used for 3D reconstruction, where a 3D density map of the particle is generated using computational algorithms. (Figure 1.15) The resulting map is refined iteratively to improve its quality and resolution. (S. H. Scheres 2012)

Finally, atomic or pseudo-atomic models are built into the density map, and the structure is validated, and its resolution estimated through various methods. This comprehensive workflow enables the determination of high-resolution structures of macromolecular complexes using cryo-EM single-particle reconstruction techniques(S. H. Scheres 2012).

Scope of Thesis

This dissertation investigates the role of photosynthetic antennae IsiA, forming supercomplex PSI-IsiA via cryo-EM to understand the structure-function relationship, with a focus on Cyanobacteria *Synechocystis* 6803. IsiA is closely associated with the adaption to iron stress, a condition prevalent in the majority of the Earth's oceans, covering over

70% of the planet's surface. The distinctive characteristics of IsiA are investigated in connection with structural insights into PSI. Chapter 2 reports the characterization and structure of PSI-IsiA isolated from Cyanobacteria *Synechocystis* 6803, revealing how IsiA forms 18 subunits with PSI trimer. Chapter 3 discusses serial spectroscopic and time-resolved fluorescence experiments conducted in vivo, examining the influence of the C-terminus of IsiA on its expression and how it alters the spectroscopic properties of IsiA. Chapter 4 delves into the characterization of PSI-IsiA extracted from mutated Cyanobacteria *Synechocystis* 6803, shedding light on the importance of point mutations at Chl8 and Chl17 for its viability. Chapter 5 provides a comprehensive review of PSI-IsiA, setting the stage for subsequent analyses. Finally, chapter 6 discusses further investigations into the impact of specific chlorophyll and C-terminus on the spectroscopic properties of chlorophylls, providing insights into the broader implications of structural variations in photosynthetic proteins.

CHAPTER 2

THE STRUCTURE OF STRESS-INDUCED PSI-ISIA ANTENNAE SUPERCOMPLEX

Hila Toporik[1], Jin Li[1,2], Yuval Mazor[1,2]

[1]Biodesign Center for Applied Structural Discover, Arizona State University, Tempe, Arizona, USA

[2]School of molecular Sciences, Arizona State University, Tempe, Arizona, USA

Abstract

Photochemical conversion in oxygenic photosynthesis takes place in two large protein–pigment complexes named PSII and PSI. Photosystems associate with antennae in vivo to increase the size of photosynthetic units to hundreds or thousands of pigments. Regulation of the interactions between antennae and photosystems allows photosynthetic organisms to adapt to their environment. In low-iron environments, cyanobacteria express IsiA, a PSI antennae, critical to their survival. Here we describe the structure of the PSI–IsiA complex isolated from the mesophilic cyanobacterium *Synechocystis* sp. PCC 6803. This 2-MDa photosystem–antennae supercomplex structure reveals more than 700 pigments coordinated by 51 subunits, as well as the mechanisms facilitating the self-assembly and association of IsiA with multiple PSI assemblies.

Introduction

The light reactions of oxygenic photosynthesis are carried out in specialized membranes called thylakoids. The core enzymatic machinery of light reactions is made up of four large membrane complexes, PSII and PSI, the cytochrome b6f complex and ATP synthase (Nelson and Yocum 2006). These four core complexes are conserved from cyanobacteria

to higher plants. The first reaction in photosynthesis, light-induced charge separation, is catalyzed by PSI and PSII. While PSI and PSII contain core antennae systems, most of the light is captured by light-harvesting proteins, or antennae, which form supercomplexes with photosystems (Croce and Van Amerongen 2014). An important layer of regulation is found in the interactions between antennae systems and photosystems which, together, form the functional photosynthetic units in cells. Both the physical association and the energy transfer efficiency between antennae and photosystems can change as photosynthetic cells respond to changes in their environment. In the green lineage leading to higher plants, membrane-bound light-harvesting antennae proteins (LHCs) diversified from a common core into a large family with multiple functions (Büchel and Büchel 2015). In cyanobacteria two main antennae families evolved, the phycobilisome, a large soluble protein–pigment complex (Saer et al. 2017) and a membrane-embedded family of proteins sharing a general architecture with the PSII subunit CP43, called IsiA and Pcb (Roche et al. 1996).

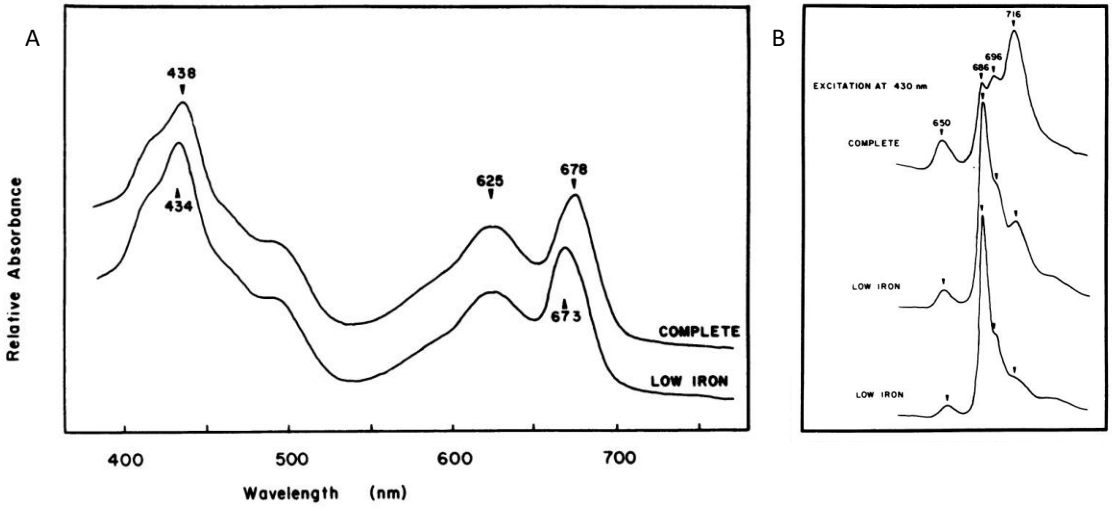

Figure 2.1. The initial discovered on IsiA. A: Absorbance of *Synechococcus cedrorum* under complete iron condition and low iron condition, low iron condition *Synechococcus cedrorum* showed a blue-shift on Qy peak. B: 77K fluorescence of *Synechococcus cedrorum* under complete iron condition and 2 different low iron condition. Reprint with permission from (Guikema and Sherman 1983)

The role of the IsiA antennae in adaptation to stress was discovered when the response of cyanobacteria to low-iron growth showed a decrease in the abundance of phycobilisomes together with a blue shift in the absorption peak of cellular chlorophyll (Guikema and Sherman 1983)(Figure 2.1). This was accompanied by the appearance of a large, chlorophyll-containing membrane complex. After subjecting cells to low iron treatment, a blue-shifted absorbance was observed, accompanied by an additional fluorescence peak adjacent to CP43.

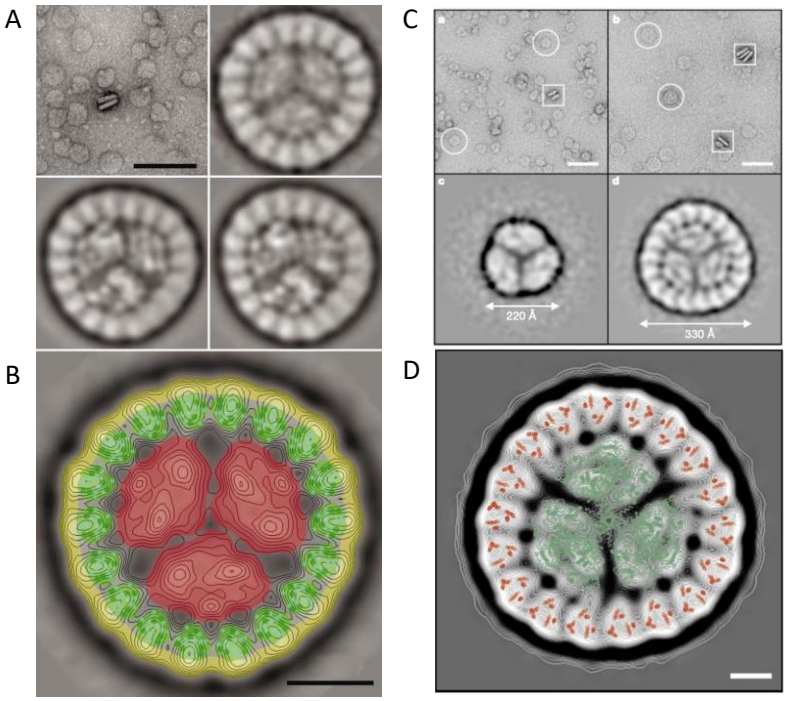

Figure 2.2. Electron microscope image of PSI-IsiA. Under iron starvation, IsiA forms a massive 2-MDa membrane complex with the PSI trimer. A and B: Electron micrograph and projection maps and modeling of the CP43′-PSI supercomplex of the mutant of *Synechocystis* 6803. A: Scale bar=1000Å. B: Scale bar=150Å. C&D: Electron micrograph of PSI trimer within the centre of an 18-member ring of CP43′from *Synechocystis* sp. PCC 6803 C: Scale bar= 50 nm. D: Scale bar= 5 nm. Reprint with permission from(Thomas S. Bibby et al. 2001; Duncan et al. 2003)

Later studies identified an iron stress-inducible operon containing IsiA (Laudenbach et al. 1988). IsiA was found to be the major component of the structural changes associated with the photosynthetic membranes under iron starvation (Burnap, Troyan, and Sherman 1993). The role of IsiA in the adaptation of cyanobacteria to stress is not limited to low-iron conditions—IsiA is induced and is required for growth in multiple stress conditions, including high-light and oxidative stress (Havaux et al. 2005; Singh, Li, and Sherman

2004). Models of IsiA based on the sequence similarity to CP43 suggested that IsiA contains six transmembrane helices and coordinates 13 chlorophylls (T S Bibby, Nield, and Barber 2001)(Figure 2.2).

Electron microscopy studies revealed that, under iron starvation, IsiA forms a massive ~2-MDa membrane complex with the PSI trimer (Thomas S. Bibby et al. 2001; Duncan et al. 2003) (Figure 2.2). Later studies uncovered the complexity of the IsiA system, showing a myriad of IsiA complexes including single and double IsiA rings devoid of PSI in addition to various assemblies surrounding PSI forms (Kouřil, Arteni, et al. 2005). The largest known IsiA complex consists of 43 IsiA monomers surrounding the PSI trimer as a double ring (Chauhan et al. 2011; Yeremenko et al. 2004).

Fluorescence decay from coupled and uncoupled IsiA assemblies was found to be much faster than other membrane-bound chlorophyll antennae (Ihalainen et al. 2005), suggesting that IsiA contains a quenched chlorophyll form, the nature of which is undermined and that may play a role in photoprotection. These rapid fluorescence decay kinetics (for an antennae) do not prevent IsiA from forming an efficient energy transfer system with PSI when coupled to it (Andrizhiyevskaya et al. 2004; Chauhan et al. 2011; Melkozernov et al. 2003).

Several low-light-adapted species of Prochlorococcus, the most abundant photosynthetic organism on Earth, contain multiple Pcb genes highly similar to IsiA (Garczarek et al. 2000). These antennae were shown to associated with both PSI and PSII in supercomplexes, thereby demonstrating that IsiA and Pcb antennae systems are highly abundant and absorb a substantial portion of photons in the oceans (Thomas S. Bibby et al. 2003). The IsiA antennae paradigm is one of the most important and least understood systems in oxygenic photosynthesis. Here we report the structure of the PSI–IsiA

supercomplex determined at a resolution of 3.5 Å using single-particle cryo-electron microscopy (cryo-EM).

Methods

Culture conditions

Cyanobacteria were cultured in glass bottles in 10 L batches using BG11 medium supplemented with 12 ng ml^{-1} ferric ammonium citrate and 5 mM glucose at 30 °C and bubbled with air after optimization of iron concentration (Figure 2.3). Light was supplied from a light-emitting diode array (Fluence RAY) at very low intensity (~15 µE).

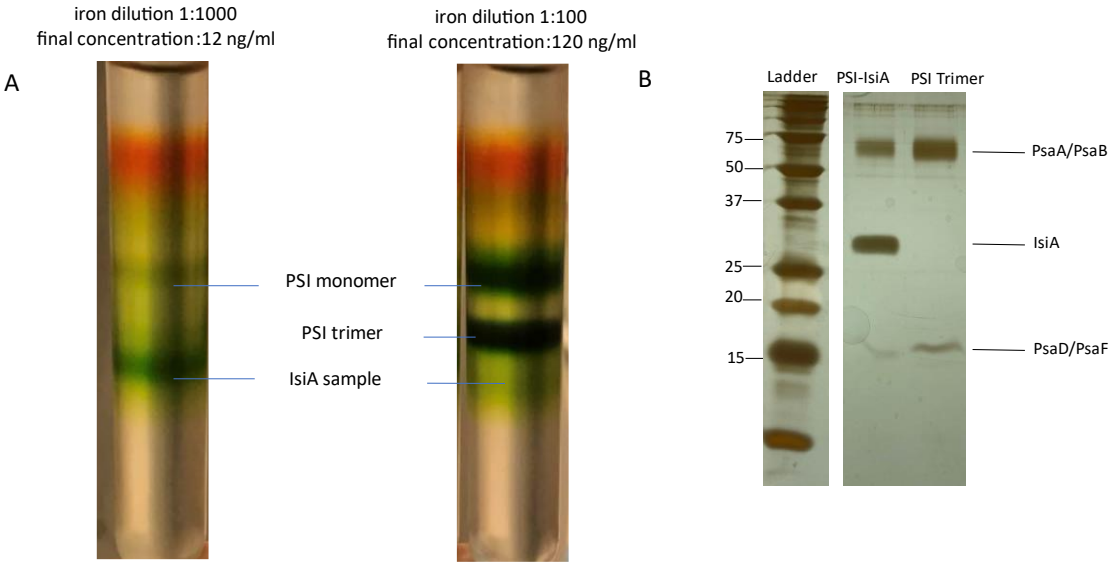

Figure 2.3. Iron optimization of PSI-IsiA and PSI-IsiA characterization. A: sucrose gradient tube of PSI-IsiA supercomplex under different iron starvation, IsiA forms heavier band on 12 ng/ml iron concentration. B: sodium dodecyl sulfate–polyacrylamide gel electrophoresis(SDS-PAGE) result of PSI-IsiA supercomplex validate the expression of IsiA.

PSI–IsiA purification

Between 20 and 40 liters of culture were harvested by centrifugation and washed once with STN1 buffer (30 mM Tricine-NaOH pH 8, 15 mM NaCl, 0.4 M sucrose). Cells were resuspended in STN1 and broken with two cycles at 30,000 psi. in a cell disruptor (Constant Systems Ltd). The lysate was cleared by centrifugation in a F20-12 × 50 LEX rotor (Thermo Scientific) for 10 min at 12,000 r.p.m. Membranes in the supernatant were pelleted using ultracentrifugation (Ti70 rotor, 45,000 r.p.m. for 2 h) and resuspended in STN2 buffer (30 mM Tricine-NaOH pH 8, 100 mM NaCl, 0.4 M sucrose). After resuspension in STN2, the membranes were incubated on ice for 30 min then collected again (Ti70 rotor, 45,000 r.p.m., 2 h) and resuspended in STN1. n-Dodecyl β-D-maltoside (DDM, Glycon) was added to the membranes at a 10:1 DDM–chlorophyll ratio. The suspension was gently mixed manually a few times then incubated on ice for 30 min. After solubilization, the insoluble material was discarded using ultracentrifugation (Ti70, 45,000 r.p.m., 30 min). The solubilized membranes were loaded onto a diethylamino ethanol column (Toyopearl DEAE-650C). The complexes were eluted using a linear NaCl gradient (15–500 mM NaCl) in 30 mM Tricine-NaOH pH 8, 0.2% DDM. Dark green fractions were collected and precipitated using 6% PEG3350 (Hampton Research). After centrifugation in a F20-12 × 50 LEX rotor for 5 min at 5,000 r.p.m., the green precipitate was resuspended in 30 mM Tricine-NaOH pH 8, 75 mM NaCl with 0.05% DDM and loaded onto a 12–60% sucrose density gradient prepared with the same buffer. Following centrifugation (Beckman SW40 rotor, 37,000 r.p.m., 16 h), the appropriate green band was precipitated using 10% PEG3350 (Hampton Research). After centrifugation in Eppendorf tabletop for 5 min at 10,000 r.p.m., the green precipitate was resuspended in 30 mM Tricine-NaOH pH 8, 75 mM NaCl with 0.05% DDM and loaded onto a 12–60% sucrose density gradient prepared with the same buffer. Following centrifugation (Beckman SW60

rotor, 56,000 r.p.m., 4 h), the appropriate green band was collected and used for subsequent experiments.

Sample preparation for single-particle cryo-EM analysis

The PSI–IsiA band (Figure 2.3) from the sucrose gradient was collected and the buffer was exchanged to 30 mM Tricine-NaOH pH 8, 75 mM NaCl and 0.02% DDM using a Sephadex G-50 gel filtration column. The PSI–IsiA complex was concentrated using a spin column (Spin-X UF 100k, Corning) to 1.5 mg chlorophyll ml^{-1}. A 3-µl drop of the PSI–IsiA complex was applied on to a holey carbon grid (C-flat 1.2/1.3 Cu 400-mesh grids, Protochips) after soaking the grid in buffer. The sample was vitrified by flash-plunging the grid into liquid ethane using an automated plunge freezer, a Vitrobot Mark IV (ThermoFisher/FEI) with a blotting time of 6 s. The grids were stored in liquid nitrogen before data acquisition.

Data acquisition

The cryo-EM specimens were imaged on a Titan Krios transmission electron microscope (ThermoFisher/FEI). Electron images were recorded using a K2 Summit direct electron detect camera (Gatan) at super-resolution counting mode. The defocus was set to −2 µm and the nominal magnification was ×47,600, corresponding to a super-resolution pixel size of 0.5252 Å at the specimen level. The counting rate was adjusted to 7.37 $e^{-}/Å^2s$. Total exposure time was 8 s, accumulating to a dose of 59 $e^{-}/Å^2$.

Data processing

A flowchart describing data handling is shown in Figure2.4. MotionCor2 was used to register the translation of each sub-frame, and the generated averages were Fourier-

cropped to ×1.5 and dose-weighted (Zheng et al. 2016). Contrast transfer function parameters for each movie were determined using CTFFIND4 (Rohou and Grigorieff 2015). Relion was then utilized for the subsequent data processing (S. H. Scheres 2012). A set of manually picked particles (~1,000) was subjected to several rounds of unsupervised 2D classification. Six class averages representing different orientations of the expected particle were selected and used as templates for the automated particle selection procedure as implemented in Relion, which yielded 572,000 particles. This particle set was subjected to several rounds of unsupervised 2D classification (Relion), leading to a set of 120,817 particles which were extracted from the original micrographs as boxes of 650 pixels and downsampled to 500 pixels, yielding a final pixel size of 1.0244 Å Px^{-1}. This particle set was subjected to 3D classification using an initial PSI–IsiA volume from a previous dataset sampled at 60 Å. This procedure yielded two classes which clearly showed the complete PSI–IsiA (I and IV) and were grouped together to yield 77,764 particles. Several further rounds of 2D classification resulted in the final set which contained 74,220 particles. Three-dimensional reconstructions using this set yielded volumes at a resolution of 3.8 Å. Finally, two cycles of per-particle contrast transfer function refinement, followed by 3D reconstruction, were carried out to give the final volume, which contained information to 3.48 Å according to the gold standard FSC test. The final map was sharpened using the postprocessing procedure in Relion, the b-factor used for sharpening being −95. Local resolution was estimated using ResMap (Kucukelbir et al. 2014).

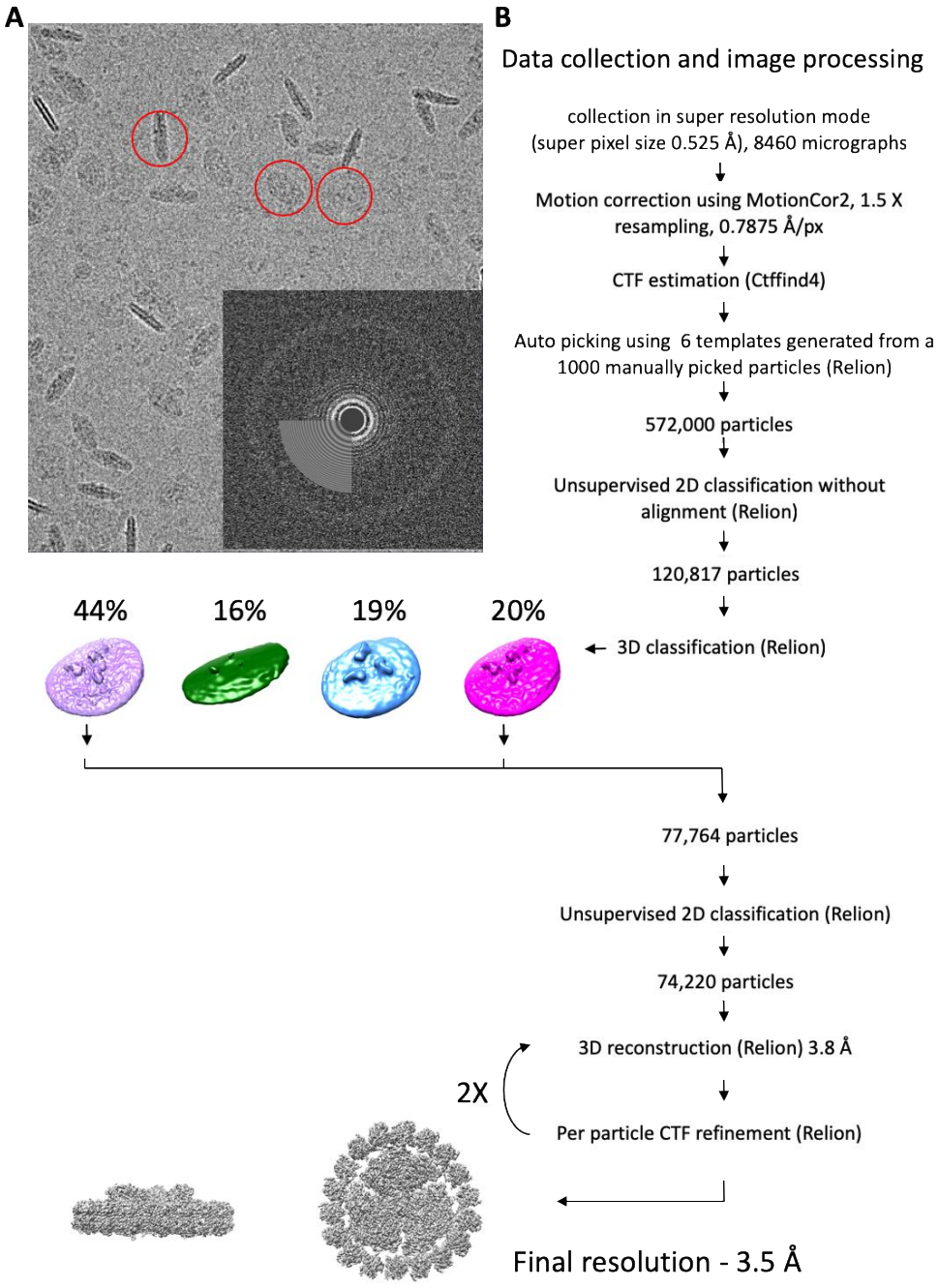

Figure 2.4. Image processing strategy. A. A representative micrograph together with the power spectrum and CTF fit. In vitreous ice, PSI-IsiA particles are visible in different orientations as projections (a subset is surrounded by a red ring). B. Flow chart describing the workflow of image processing.

Model building and refinement

The initial PSI model was taken from the 2.5-Å X-ray structure of the trimeric PSI from Synechocystis (PDB: 5OY0) (Malavath et al. 2018). The model was docked into the map using UCSF Chimera (Pettersen et al. 2004). Monomeric IsiA was built manually using Coot(Emsley et al. 2010) based on the atomic model of CP43 from the cyanobacterial PSII structure (PDB: 3WU2), whenever appropriate (Umena et al. 2011). The final model was refined against the cryo-EM density map using phenix.real_space_refine (Adams et al. 2010; Afonine et al. 2013). Final model statistics are shown in Figure 2.5 and Table 1. PyMOL and UCSF Chimera were used to generate all images.

Dipole orientation calculation

We calculated the squared dipole orientation factor as defined in Förster theory (Förster and Förster 1947), similarly to (Mazor et al. 2017). The Förster energy transfer rate, KDA, between a donor (D) and an acceptor molecule (A) is defined as

$$K_{\mathrm{DA}} = \frac{C_{\mathrm{DA}} K^2}{N^4 R_{\mathrm{DA}}^6}$$

, where CDA is a factor calculated from the overlap integral between the donor emission and acceptor absorbance. N is the refractive index of the medium. K2 is the dipole orientation factor, defined as

$$K^2 = (\hat{\mu}_{\mathrm{D}} \cdot \hat{\mu}_{\mathrm{A}} - 3(\hat{\mu}_{\mathrm{D}} \cdot \hat{R}_{\mathrm{DA}})(\hat{\mu}_{\mathrm{A}} \cdot \hat{R}_{\mathrm{DA}}))^2$$

$\hat{\mu}_{\mathrm{D}}$and $\hat{\mu}_{\mathrm{A}}$ are the dipole unit vectors (taken as the vector between the NB and ND atoms of the specific chlorophyll molecule), and $\hat{R}_{\mathrm{DA}}$ is the distance between the two pigments

(taken as the Mg–Mg distance between each pair of chlorophylls). The calculation was carried out using an R script.

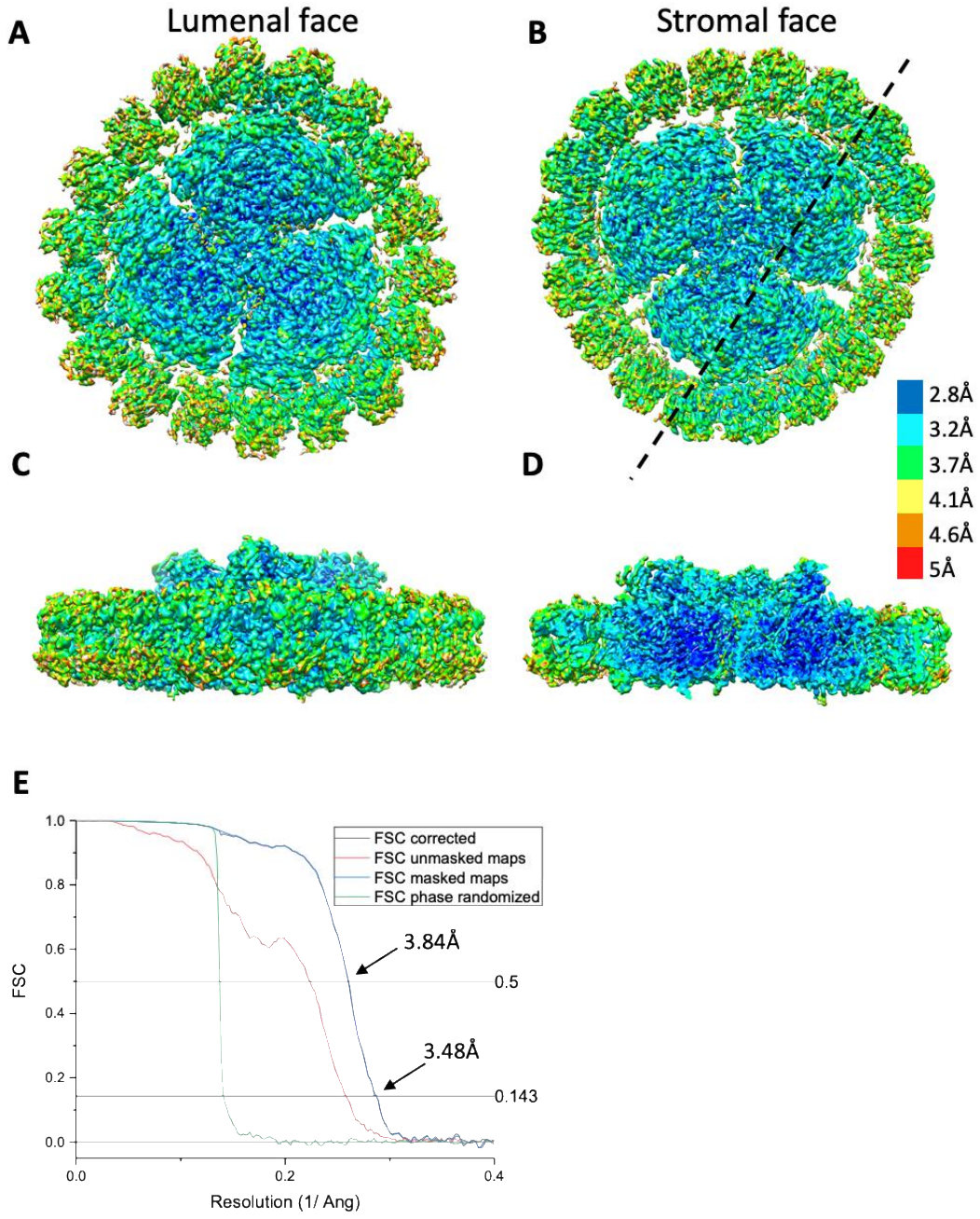

Figure 2.5. Global and local resolution. A, B, C and D: The final 3D map colored according to the local resolution estimates obtained from ResMap, seen from the Lumen 'A', Stroma 'B', membrane

‘C’ and membrane section with surface capping along the dashed line ‘D’ orientations. E. Plots of Fourier shell correlation (FSC) against resolution.

Results

Structure determination and modeling.

The structure of the PSI–IsiA complex was determined using single-particle cryo-EM (Fig. 2.4 and table 1). The PSI–IsiA complex was purified from the mesophilic cyanobacterium Synechocystis sp. PCC 6803. Careful optimization of growth conditions resulted in a nearly homogeneous appearance of the PSI–IsiA complex in sucrose gradients Figure 2.3). An initial three-dimensional (3D) density map was ab initio calculated from single-particle images. Representative two-dimensional (2D) class averages showed a homogeneous particle population with clear features of a PSI trimer enclosed by an outer IsiA ring. The final map was determined to 3.5-Å resolution as assessed by the gold standard Fourier shell correlation (FSC) criteria (S. H. W. Scheres et al. 2012). The membrane-bound parts of the complex were resolved at higher resolutions (up to 2.8 Å), and the surface-exposed loops and outer faces of the IsiA ring showed local resolution values of 4.6 Å. The location and orientation of all 591 chlorophyll molecules, as well as those of 135 carotenoid molecules, were determined (Fig. 2.4).

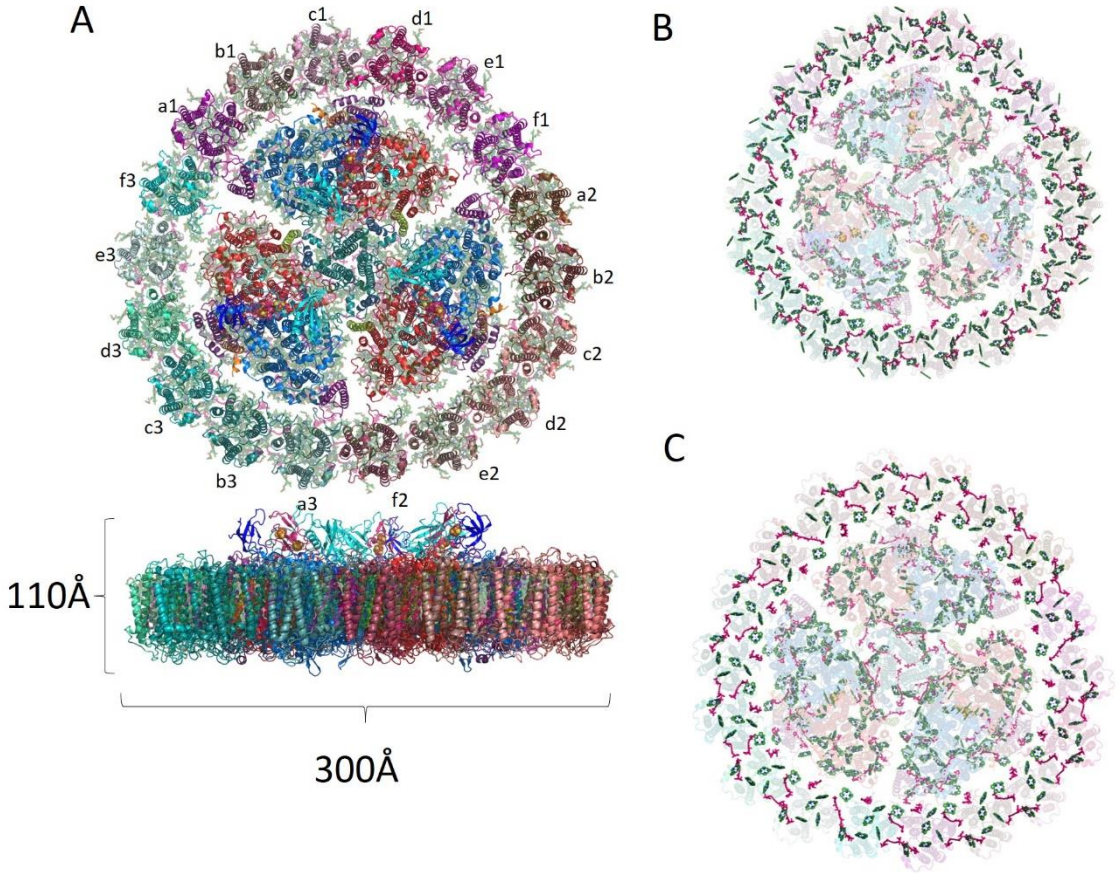

Figure 2.6. An overview of PSI-IsiA: A. Stromal view of stress-induced photosystem I-IsiA super complex (PDBID:6NWA). 18 IsiA monomer form a ring around PSI trimer. Every IsiA is labelled by its location of PSI. All protein subunit colored individually, chlorophylls are green, carotenoids are pink. B, C. Pigments organization of PSI-IsiA complex. Carotenoids are colored pink and chlorophylls are colored pink. B. Stromal view of pigments organization. In total, 198 chlorophylls are located on this side. C. Luminal view of pigments organization. 108 chlorophylls are located on this side.

Data collection and processing	
Electron microscope	Titan Krios
Electron detector	K2 Summit
Magnification	47,600
Voltage (kV)	300
Dose rate ($e^-/Å^2$ s)	7.37
Average Defocus (μm)	2
Super pixel size (Å)	0.5252
Symmetry imposed	C3
Initial number of particles	572,000
Final number of particles	74,220
Resolution by 0.143-criteria	3.48
Map resolution range (Å)	2.8 – 5
Map sharpening B factor (Å)	-95

Table 2.1. Data collection and processing statistics.

Overall structure and organization

The complete PSI–IsiA complex appears as an almost round disk with threefold rotational symmetry (Fig. 2.6A). Eighteen individual IsiA subunits are clearly resolved in our density map. The entire complex measures 300 Å in diameter, with a height of 110 Å (Fig. 2.6A). Previous negative-stain and cryo-EM studies assigned transmembrane helices V and VI as being closest to PSI in the supercomplex (Thomas S. Bibby et al. 2001; Duncan et al. 2003). Our higher-resolution map clearly shows that four helices, I,II,V,VI, face PSI, with each IsiA monomer being rotated approximately 60° compared to the previously assigned configuration (Fig. 2.6A). This has far-reaching consequences regarding the identity of the connecting pigments between neighboring IsiA monomers and between the entire 18-mer ring and PSI (discussed below). The C3 symmetry observed in PSI–IsiA is probably determined by interaction of the IsiA ring with the PSI trimer. We refer to each IsiA monomer in the three IsiA hexamers as a–f, starting at the PsaK pole of each PSI monomer (Fig. 2.6A).

There are 591 chlorophylls in the PSI–IsiA supercomplex, by far the largest number of bound pigments in any of the photosynthetic supercomplexes with known structure (Fig. 2.6B&C). These 591 chlorophylls are split almost equally between the IsiA ring (306 chlorophylls) and the PSI trimer (285 chlorophylls), and this agrees well with spectroscopic measurements (Andrizhiyevskaya et al. 2002). The organization of the 306 chlorophylls bound by the IsiA ring stands out in two respects. First, there is a striking asymmetry in pigment distribution between the stromal and luminal sides of the membrane, with 198 chlorophylls on the former and 108 on the latter (Fig. 2.6B&C). Second, the stromal-side chlorophylls form a continuous layer of pigments surrounding PSI (Fig. 2.7A–C) while on the luminal side distinct chlorophyll clusters are readily observed (Figs. 2.6C

and 2.7D–F). The tight connectivity on the stromal side stands out when compared with eukaryotic antennae systems, which appear as sparsely connected pigment clusters(Mazor et al. 2017; Pi et al. 2018; Qin et al. 2015; Su et al. 2017). This connectivity may be one of the reasons for the rapid fluorescence decay observed in IsiA that was suggested to play an important part in its photoprotective function(Ihalainen et al. 2005).

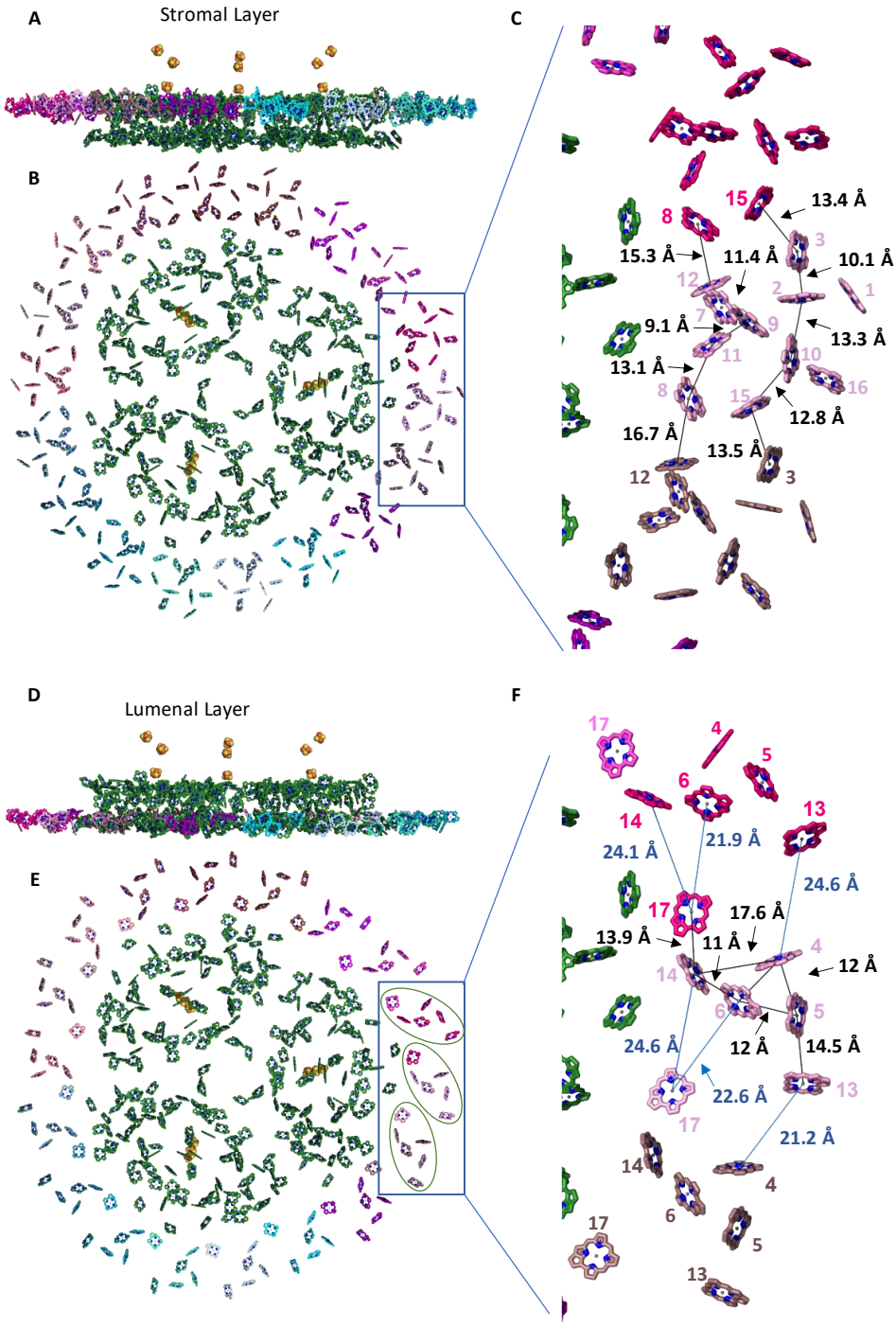

Figure 2.7. Organization of two chlorophyll layers in PSI-IsiA. A. Side view of the PSI-IsiA chlorophyll rings. Chlorophylls coordinated by PSI are colored green. Only IsiA chlorophylls belonging to the stromal layer are shown. IsiA chlorophylls are colored according to their

coordinating IsiA subunit. The three PSI iron sulfur clusters are shown as spheres to indicate the orientation of PSI-IsiA. B. A view from the lumenal side of the membrane of the stromal chlorophylls layer showing the overall organization. Three IsiA stromal clusters are presented in 'E' with selected distances between individual chlorophylls. C. Side view of the Lumenal chlorophylls in PSI-IsiA, colored as in 'A'. B. A view from the luminal side, three lumenal clusters are highlighted and magnified in 'F'. E. A view of three stromal IsiA chlorophyll clusters. A subset of Mg-to-Mg distances are shown, demonstrating that pigments on this layer are relatively well connected across the entire IsiA ring. F.The lumenal pigment layer in PSI-IsiA is separated into distinct clusters. Three lumenal IsiA clusters are shown. Distances separating the two clusters are shown in blue.

The overall structure of IsiA follows the general fold of CP43, with six transmembrane helices. Unique to IsiA is the configuration of the E loop (nomenclature is from(T S Bibby, Nield, and Barber 2001)) linking transmembrane helices V and VI. Our structure shows that this luminal-side loop extends into the membrane space and coordinates a new chlorophyll position (numbered 17; Fig. 2.8a,b). Each IsiA monomer coordinates 17 chlorophyll molecules, 13 of which occupy similar positions to CP43 chlorophylls while four are unique to IsiA (Fig. 2.8B). A complete list of all chlorophyll-coordinating side chains in IsiA is presented in Supplementary Table 1. Previous studies suggested that each IsiA monomer binds a total of four carotenoids—two beta-carotenes, one echinenone and one zeaxanthin(Melkozernov et al. 2003). We identified four carotenoid molecules, modeled as beta-carotenes, in most of the IsiA monomers (a total of 69 carotenoids in the entire IsiA ring), in good agreement with these measurements. Three of these carotenoids occupy similar positions to CP43 (B2, B3 and B4 in Fig. 2.8c,d) and bind at the IsiA–IsiA interface. An additional carotenoid, B1, lines the interface between IsiA and PSI. A similar configuration, where a carotenoid is positioned in the gap between PSI and its antennae, is found in the plant PSI–light-harvesting complex I LHCI) structure(Mazor et al. 2015; Qin

et al. 2015). It is possible that this configuration serves a photoprotective function. There has been some disagreement regarding the occurrence of energy transfer between carotenoids and chlorophylls in IsiA(H.-Y. S. Chen et al. 2017). The close proximity observed between all four carotenoids and their neighboring chlorophylls (~4 Å, Fig. 2.8c,d) suggests that excitation energy transfer to chlorophylls should occur as efficiently as it does in all other photosynthetic complexes(Berera et al. 2010). Such close distances also support a role for these carotenoids in photoprotection as quenchers of chlorophyll triplets. Interestingly, all of these chlorophyll–carotenoid interactions occur at the stromal pigment layer, adding to the asymmetric distribution of pigments between the two faces of the membrane.

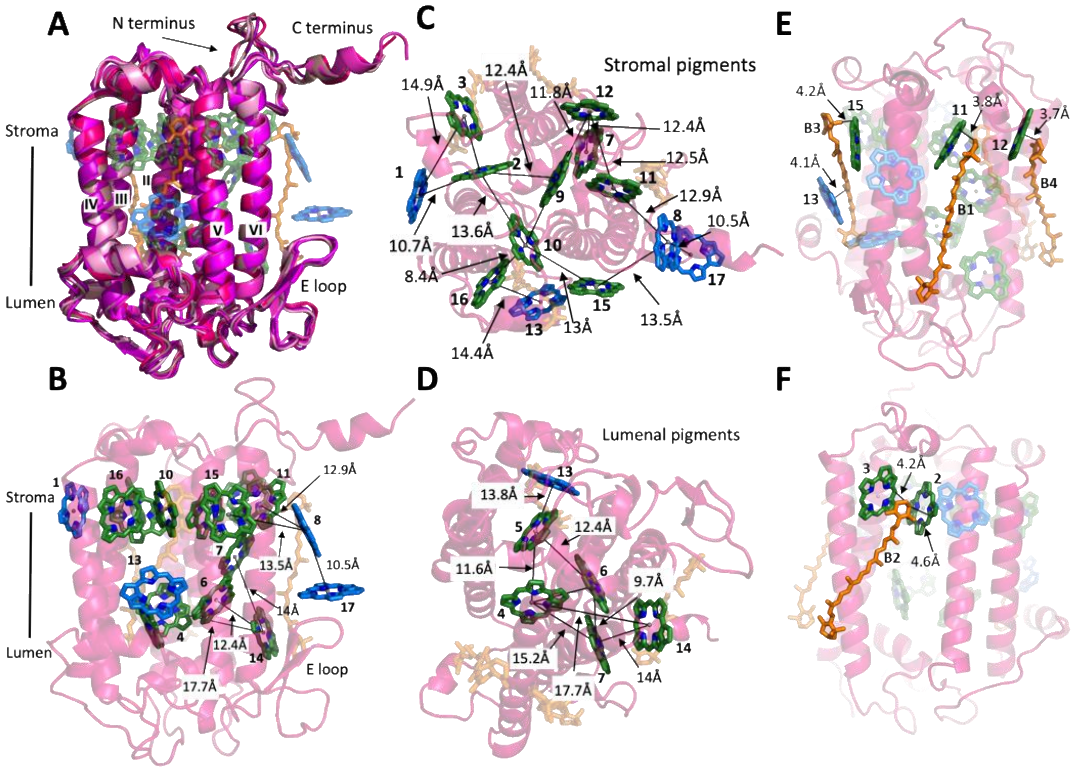

Figure 2.8. Structure of IsiA. (A) Superposition of all six IsiA monomers (a-f) showing similar conformations with small differences in the protein backbone. Each of the six TM helices is labeled

according to its sequence position. Loop E, unique to IsiA is also labeled. (B) Each IsiA monomer coordinates 17 chlorophylls, 13 of them (green) occupy similar positions to CP43. The remaining four chlorophylls, numbered 1, 8, 13 and 17 (blue), are unique to IsiA. Chlorophylls 17 and 8 which face PSI are especially important for energy transfer in the complex. (C) Stromal side chlorophylls of IsiA, with the shortest Mg to Mg distances drawn, form a tight cluster. Chlorophyll 8 is the closest neighbor of chlorophyll 17. (D) Lumenal chlorophylls of IsiA with Mg to Mg distances. Chlorophylls 7 and 13 are shown in both C and D as they appear to connect both clusters. (E) and (F) The four carotene molecules (orange) in IsiA with their adjacent chlorophylls. Positions B2, B3 and B4 are similar to CP43, while B1 is unique to IsiA.

One of the most important structural elements in IsiA is the E loop and its coordinated chlorophylls—these are strategically located to connect each IsiA monomer with its neighbor, and also play a role in the interaction between IsiA and PSI (discussed in Chapter 3 Figs. 2.8a,b). Supplementary Tables 2.1 and 2.2 list Mg–Mg distances and the dipole orientations between the 17 chlorophylls coordinated by IsiA, respectively. Chlorophyll 17 is linked to the main pigment cluster via chlorophyll 8, which is also unique to IsiA (Fig. 3b,e). However, the low value of the dipole orientation factor between chlorophylls 8 and 17 (0.02) suggests that these are nearly orthogonal, which should slow the transfer rate considerably. This orientation effect may be compensated by the optical properties of the individual chlorophylls, which are unknown. In addition, chlorophyll 17 closely associates with the neighbor IsiA luminal chlorophyll cluster (Fig. 2f) and may interact with chlorophylls from the adjacent subunit more favorably. These two new chlorophylls create the interface needed for energy transfer in the PSI–IsiA supercomplex.

The 17 chlorophylls coordinated by IsiA form a tightly linked cluster with an average nearest neighbor Mg–Mg distance of 10.9 Å (Supplementary Table 2.1). The chlorophyll

distribution is markedly asymmetric, with ten chlorophylls located at the stromal side of the membrane, four at the luminal side and three occupying middle positions (chlorophylls 7, 13 and 17; Fig. 2.8b,e,f).

Discussion

In photosynthetic cells, photosynthesis is carried out in photosynthetic units, antennae–photosystems supercomplexes. While photosystems display almost absolute conservation across domains, antennae systems have evolved considerably. IsiA is a member of a large family of membrane-bound antennae, similar to the PSII subunit CP43 that evolved in cyanobacteria. IsiA is induced under multiple stress conditions, although low iron concentration, in the environmentally relevant nanomolar range, is the most potent inducer. As PSI is one of the largest iron sinks in the cell, one of the proposed primary roles of IsiA is to increase the absorbance cross-section of PSI. This is clearly accomplished as the number of bound chlorophylls in PSI–IsiA is more than doubled compared to PSI alone. The benefits of increased PSI cross-sections are not so easily explained when considering additional environmental cues that result in IsiA induction, such as oxidative stress and high light levels. It is likely that the role of IsiA as a stress resistance factor is more complicated and is not limited to light harvesting(Havaux et al. 2005; Singh, Li, and Sherman 2004; Yeremenko et al. 2004). The IsiA system stands out by its ability to form an incredibly large number of assemblies using a single building block(Kouřil, Arteni, et al. 2005; Yeremenko et al. 2004). Some of these assemblies include PSI while others consist of IsiA alone. The basis for this architectural flexibility is found in the physical interactions between the N and C termini of adjacent subunits. The flexibility of the C-terminal helix enables a range of IsiA dimers that still preserve efficient excitation energy transfer in the IsiA ring.

One of the four additional chlorophylls identified in IsiA (No. 13) is positioned on the ring periphery, and it is probable that this chlorophyll is important for interactions between different IsiA layers, a feature of the even larger PSI–IsiA double-ring complex and some of the IsiA-only assemblies.

Two additional chlorophylls (8 and 17) constitute a clear connection between adjacent IsiA subunits and between the ring and the PSI trimer. Chlorophyll 17 in particular is positioned in a favorable orientation and distance to interact with chlorophyll 14, coordinated by the adjacent IsiA monomer (Fig. 2.8f). This interaction may increase substantially (as chlorophylls 17 and 14 are brought closer together) in IsiA-only assemblies that form tighter rings, and this can have functional consequences with regards to excitation energy quenching. The heterogenous nature of IsiA assemblies in vivo and in vitro presents a major barrier towards answering these questions in a precise manner.

PSI–IsiA stands out in regard to the size, flexibility and diversity of functions among the known photosynthetic supercomplexes. Overall, chlorophyll distribution in the IsiA ring is highly biased towards the stromal side of the membrane, which may facilitate interactions with soluble phycobilisomes that are still present in iron-deprived cells.

The current structure uncovers the basic, most crucial, details of this enormous machine in the first example from the cyanobacterial branch of the membrane-embedded antennae proteins, and lays a path for evaluating the light-harvesting and photoprotection mechanisms in cyanobacteria.

Figure supplements

1	501	502	503	507	508	509	510	511	512	515	516	513	517	504	505	506	514
501		10.66	14.97	28.17	40.42	22.47	18.80	31.19	30.62	31.68	17.86	28.84	46.14	22.50	23.70	28.26	38.35
502	10.66		9.32	17.97	31.80	12.38	13.58	21.40	20.18	25.75	18.57	25.75	38.02	16.57	20.36	20.20	29.50
503	14.97	9.32		21.17	37.86	17.48	22.46	25.96	19.78	33.96	26.74	35.60	44.34	20.05	27.44	25.65	31.91
507	28.17	17.97	21.17		19.98	9.37	18.82	11.30	11.90	22.31	26.22	27.14	24.63	15.15	20.51	9.72	17.04
508	40.42	31.80	37.86	19.98		20.44	22.71	12.92	24.58	13.54	29.00	26.02	10.47	31.44	29.32	20.87	25.36
509	22.47	12.38	17.48	9.37	20.44		11.82	9.07	11.78	18.33	19.95	25.31	27.79	18.62	21.63	15.00	23.16
510	18.80	13.58	22.46	18.82	22.71	11.82		16.68	23.45	12.97	8.43	16.88	29.12	21.52	18.41	18.44	30.09
511	31.19	21.40	25.96	11.30	12.92	9.07	16.68		12.49	16.11	24.94	27.49	21.65	24.80	26.49	17.72	22.93
512	30.62	20.18	19.78	11.90	24.58	11.78	23.45	12.49		27.80	31.60	36.42	32.05	24.49	31.06	21.54	23.61
515	31.68	25.75	33.96	22.31	13.54	18.33	12.97	16.11	27.80		16.85	16.14	19.42	28.90	23.51	20.80	30.71
516	17.86	18.57	26.74	26.22	29.00	19.95	8.43	24.94	31.60	16.85		14.34	34.01	24.87	18.77	23.59	35.92
513	28.84	25.75	35.60	27.14	26.02	25.31	16.88	27.49	36.42	16.14	14.34		26.37	24.56	13.94	20.16	31.48
517	46.14	38.02	44.34	24.63	10.47	27.79	29.12	21.65	32.05	19.42	34.01	26.37		33.21	29.68	22.07	24.18
504	22.50	16.57	20.05	15.15	31.44	18.62	21.52	24.80	24.49	28.90	24.87	24.56	33.21		11.66	11.18	17.72
505	23.70	20.36	27.44	20.51	29.32	21.63	18.41	26.49	31.06	23.51	18.77	13.94	29.68	11.66		12.39	22.85
506	28.26	20.20	25.65	9.72	20.87	15.00	18.44	17.72	21.54	20.80	23.59	20.16	22.07	11.18	12.39		12.40
514	38.35	29.50	31.91	17.04	25.36	23.16	30.09	22.93	23.61	30.71	35.92	31.48	24.18	17.72	22.85	12.40	

Table S2.1. Mg to Mg distances in the IsiA monomer. Distances are colored on a color scale from red (8 Å) to white (30 Å). The top ten rows contain the stromal side pigment and the bottom four rows the lumenal side pigments, the middle pigments are shown in between.

Chlorophyll coordinating residues in IsiA	
Chl 1	His 144
Chl 2	His 145
Chl 3	His 110
Chl 4	His 96
Chl 5	His 207
Chl 6	His 307
Chl 7	Gln 34
Chl 8	Gln 316
Chl 9	His 31
Chl 10	Probable H_2O (observed in chain C of PDBID 3WUC)
Chl 11	His 321
Chl 12	Asn 17
Chl 13	Gln 191
Chl 14	Probable H_2O (observed in chain C of PDBID 3WUC)
Chl 15	His 318
Chl 16	His 221
Chl 17	Ile 282 (backbone carbonyl)

Table S2.2. Chlorophyll coordination in IsiA.

CHAPTER 3

A role for the IsiA C terminus in the assembly of PSI-IsiA.

Jin Li[1,2], Anton Khmelnitskiy[1], Yuval Mazor[1,2]

[1]Biodesign Center for Applied Structural Discover, Arizona State University, Tempe, Arizona, USA

[2]School of molecular Sciences, Arizona State University, Tempe, Arizona, USA

Introduction

To increase the absorption cross section, PSI and PSII associate with antennae systems (Croce and Van Amerongen 2014). In cyanobacteria, phycobilisomes act as the major antennae system for PSII and PSI in iron rich conditions (Mullineaux and Emlyn-Jones 2005). However, bioavailable iron is scarce outside of laboratory conditions. When iron is not readily available, cyanobacteria utilize an antennae belonging to a family known as the iron stress induced (IsiA) proteins, specifically IsiA (Burnap, Troyan, and Sherman 1993).

IsiA was discovered when cyanobacteria were being studied in low iron conditions (Guikema and Sherman 1983). IsiA was later shown to be responsible for the structural changes in the thylakoid membranes observed under low iron conditions (Burnap, Troyan, and Sherman 1993). Although these discoveries were made in iron stressed cells, leading to the name IsiA, the expression of this antennae is not limited to low iron conditions. Under other stress conditions, such as high light and oxidative stress, IsiA expression is also induced (Havaux et al. 2005; Singh, Li, and Sherman 2004).

In chapter2 we talked we solved a high resolution structure of the PSI-IsiA antennae super complex from *Synechocystis* sp. PCC 6803 to 3.5 Å by cryogenic transmission electron

microscope (Cryo-EM) (Toporik et al. 2019).The structure of the PSI-IsiA super complex is disk shaped with a diameter of 300 Å, and height of 100 Å and three-fold rotational symmetry (Figure 2.6). Compared to the previously assigned configuration of IsiA, the new structure provides insights into the PSI-IsiA relationship by clearly showing that the four helices I, II, V, VI, face PSI (Toporik et al. 2019). In addition, the structure shows there are 591 chlorophylls in the PSI-IsiA super-complex, with 306 chlorophylls located in the IsiA ring and 285 chlorophylls located in the PSI trimer. The association of IsiA to PSI more than doubles the number of chlorophylls, thus significantly increasing the light harvesting capabilities of the PSI trimer.

IsiA has been called CP43' since it was discovered because of highly homology to CP43 in PSII(T S Bibby, Nield, and Barber 2001; Duncan et al. 2003). While the IsiA monomer closely resembles the overall conformation of the CP43 subunit found in PSII, there are three notable differences in IsiA, a shortened E loop between helixes V and VI, a different confirmation of the C-terminus and 4 additional chlorophylls and 1 additional carotenoid in IsiA (Figure 3.1). The C terminus of IsiA was found to be important for interactions with neighboring IsiA monomers for the formation of the ring structures seen around PSI (Toporik et al. 2019). It is shown in the recently solved structure that the C-terminus of an IsiA monomer coordinates with the N-terminus of the adjacent IsiA monomer, allowing for larger ring structures to form.

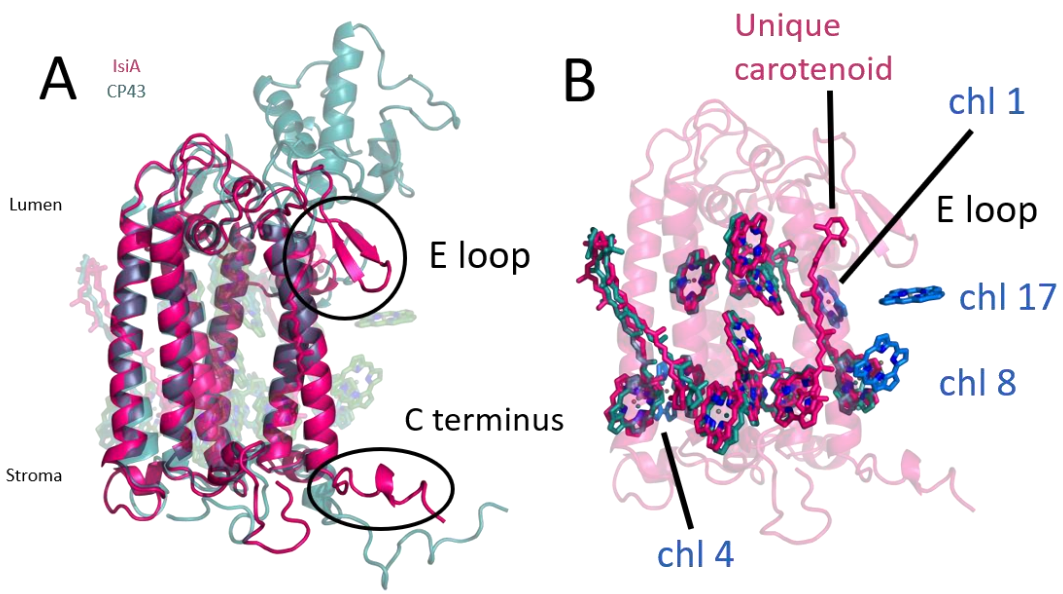

Figure 3.1. An overview of the IsiA monomer: Comparison of IsiA monomer and CP43. A. Superposition of IsiA monomer (PDBID:6NWA) and CP43 (chain C of PDBID:3WU2). IsiA shows highly conserved transmembrane helices core with CP43. The E loop (located between helices V and helices VI) and a short C terminus are unique to IsiA. E loop is located between helices V and helices VI. B. Four unique chlorophylls (in blue) and one extra carotenoid on IsiA monomer.

In Chapter 2 we have talked about a range of dimer IsiA formed*(Toporik et al. 2019)*. IsiA stands out as a unique antennae due to the multitude of interactions formed by a single monomer. However, this exceptional flexibility does not arise from the structural adaptability of IsiA itself. Despite all six IsiA monomers adopting a similar conformation with a mean square deviation of ~0.5 Å calculated over all backbone atoms, these subtle conformational changes in individual IsiA monomers fail to explain the flexibility observed in IsiA assemblies. In our previous study, we investigated the flexibility within the IsiA ring by dissecting each hexamer into adjacent IsiA dimers ('ab', 'bc', 'cd', ..., 'fa')

and aligning the leading IsiA subunit of these dimers(Figure 3.2A). This analysis revealed significant movement in the second subunit of each dimer (Figure 3.2B). Specifically, the inwardly rotated conformation observed in the 'cd' dimer interacts with the PsaF and PsaJ subunits of PSI, while the outwardly rotated 'ef' dimer faces the PsaB subunit (Figure 3.2B). Notably, the 'ef' dimer in the outward configuration exhibits the largest IsiA–IsiA chlorophyll distances. Compared to IsiAd, IsiAf missed a part of C-terminus. To examine the role of the IsiA C-terminus in complex assembly and energy transfer we generated a C-terminus deletion in IsiA.

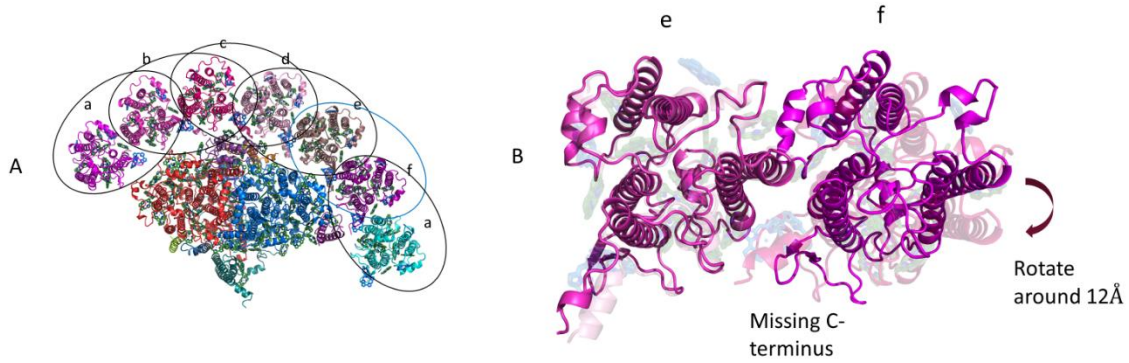

Figure 3.2. Conformational flexibility among IsiA dimers.: A: luminal view of PSI-IsiA supercomplex, one PSI monomer with its corresponding IsiA hexamer, one IsiA monomer also interact with its neighbor IsiA. B: Superposition of Stromal IsiA pairs cd and ef, shows the largest rotation of IsiA dimer has 12Å. One the IsiA monomer named f, lost C-terminus.

Methods

Construction of IsiA mutations

All mutations were made in *Synechocystis* sp. PCC 6803. A plasmid, pIsiA-Cm was constructed containing gene fragments comprising an upstream fragment of IsiA, the IsiA operon (including IsiA, IsiB (flavodoxin), IsiC (encoding a hydrolase)) (Kojima et al. 2006;

Shen, Gan, and Bryant 2016) and the downstream sequence of the operon (Supplement Figures 3.1, 3.2, 3.3). Upstream and downstream sequences (0.8 kb in each direction) are used to direct the integration of the new cassettes to the Isi operon. Furthermore, chloramphenicol (Cm) resistance was inserted 300 bases upstream of the IsiA promoter. This plasmid will be the base for all future mutations made on IsiA chlorophylls and used to make a Cm marked strain as positive control (WT) (Supplement Fig3.1) for all experiments.

IsiAΔC construction (Supplement Fig3.2) The IsiAΔC mutation was constructed into pIsiA-Cm by deleting last 10 amino acid (30 base pairs) of IsiA with P60_Forward_insert and P60_Reverse_insert primers and p60 as a template. The two fragments were assembled using the NEBuilder® HiFi DNA Assembly Master Mix(Thomas, Maynard, and Gill 2015). All plasmids were sequenced before being used to transform *Synechocystis sp. PCC6803* according to standard protocols. Complete segregation and correct replacement of IsiA to IsiAΔC was verified by PCR and sequencing (Supplementary Figure3.2).

ΔIsiA strain (Supplement Fig3.3) was constructed by a knock-out mutation on WT plasmid on IsiA using DisiA_UP and DisiA_down primer pairs. All fragments amplified by PCR will also be assembled using the NEBuilder® HiFi DNA Assembly Master Mix.
All primer sequences are listed in Supplementary.

Culture conditions

Same as Chapter 2, cyanobacteria were cultured in glass flasks in 50 ml then transfer to glass bottles in 10 L batches using BG11 medium supplemented with 6ng ml^{-1} ferric ammonium citrate and 5 mM glucose at 30 °C and bubbled with air after optimization of

iron concentration. Light was supplied from a light-emitting diode array (Fluence RAY) at very low intensity (~6 µE).

Spectroscopic analysis In Vivo

Cyanobacteria were harvested after 7 days of culturing in BG11 medium. Absorption spectra were recorded on a Cary 4000 UV–Vis spectrophotometer (Agilent Technologies). Fluorescence spectra were recorded on a Fluoromax-4 spectrofluorometer (HORIBA Jobin-Yvon). The slit width was set to 5 nm on both the entrance and exit monochromators for room temperature measurements. In vivo absorption Spectroscopy was measured under an integrating diffuse reflectance sphere (DRA 900) to correct for scattering by the cells as mentioned in (Kortüm, Braun, and Herzog 1963). Figures were prepared using OriginPro (OriginLab)

Time-resolved fluorescence

For fluorescence decay measurements using TCSPC, fiber supercontinuum laser (Fianium SC450) was used to generate excitation pulses at 440 nm with a repetition rate of 20 MHz. Fluorescence emission from the samples was collected using a 90° excitation-detection geometry and fluorescence was passed through a double grating monochromator (Jobin-Yvon, Gemini-180) and detected by a microchannel plate photomultiplier tube (Hamamatsu R3809U-50). The samples were diluted to an optical density (OD) of 0.1 at the Qy maximum, then diluted in a 3.5-ml cuvette with a 1 cm path length and maintained at room temperature. The emission polarizer was set to the magic angle (54.7°) relative to that of excitation polarizer. Data acquisition was performed using a single photon counting card (Becker-Hickl, SPC830). The instrument response function FWHM was 20 ps, as verified by scattering.

Global Analysis.

The streak camera data were analyzed with matlab based on the approach (van Stokkum, Larsen, and Van Grondelle 2004).

JTS-10 time-resolved spectroscopy

The kinetics of PSI special pair (P700) oxidation were assessed using a Joliot-type spectrophotometer (Bio-Logic SAS JTS-10). Measurements were conducted employing actinic light at various intensities, as detailed in the "Results" section. P700 activity was quantified by monitoring the transient decrease in 705-nm absorption, indicative of P700 oxidation. For measurements performed on isolated PSI–IsiAΔC complexes, 500 µM methyl-viologen (Sigma-Aldrich) was added to the sample. The estimation of PSI antennae size was inferred inversely from the time taken to achieve half of the maximum P700 oxidation.(Ballottari et al. 2014)

PSI–IsiAΔC purification, sample preparation for cryo-EM analysis and cryo-EM data acquisition were conducted in a similar manner to PSI-IsiA isolation (described in chapter 2).

Data processing

A flowchart describing data handling is shown in Supplement table 3.1. MotionCor2 was used to register the translation of each sub-frame, and the generated averages were Fourier-cropped and dose-weighted (Zheng et al. 2016). Contrast transfer function parameters for each movie were determined using CTFFIND4 (Rohou and Grigorieff 2015). Relion was then utilized for the subsequent data processing (S. H. Scheres 2012). Topaz(Bepler et al. 2020) was used in picking particles to several rounds of unsupervised 2D classification. 3 different size as 360 Å, 400 Å and 440 Å were chosen in topaz autopicking for different orientation of PSI-IsiAΔC which yielded 75083, 90274, 75613 particles. This particle set was subjected to several rounds of unsupervised 2D classification (Relion), leading to a set of 88175 particles which were extracted from the

original micrographs as boxes of 650 pixels and downsampled to 500 pixels, yielding a final pixel size of 1.03 Å Px^{-1}. This particle set was subjected to 3D classification using an initial PSI–IsiA volume from a previous dataset sampled. This procedure yielded 4 classes which clearly showed the complete PSI–IsiAΔC and were grouped together to yield 6460 particles. Due to low number of particles, three-dimensional reconstructions using this set yielded volumes at a resolution of 11.2 Å.

Results

IsiAΔC decrease the growth rate under low iron condition.

To check a mutated IsiA strain that affect the function of IsiA to grow under low iron environments, IsiAΔC strain, WT strain and ΔIsiA strain were taken from BG11 plates (an iron rich environment) into BG11 liquid culture with 6µg/ml concentration of iron. The WT strain will be used as positive control and ΔIsiA strain as negative control.

All strain were cultivated in BG-11 growth media supplemented with 6µg/ml concentration of iron and exposed to light intensities under 6 µmol photon m^{-2} s^{-1} of white light at 30° C for a week to measure the growth rate of these strains under low iron condition. The optical density of the culture at 730 nm (OD_{730}) was chosen to estimate the growth rate and was recorded through Cary 4000 spectrometer on 1 cm cuvette (Figure 3.3). The ability of IsiAΔC strain of grow under low iron condition was compared to WT and ΔIsiA strains.

Within limited iron supplement, IsiAΔC grew notably slower than WT from day 3 to day 9. This suggests a function for the C-terminus of IsiA in iron limited growth. The IsiAΔC strain exhibited a higher growth rate compared to the ΔIsiA strain, indicating that IsiAΔC assemblies still contribute to growth. After day 9, all 3 strains, WT, IsiAΔC, ΔIsiA reached the stationary phase of growth curve.

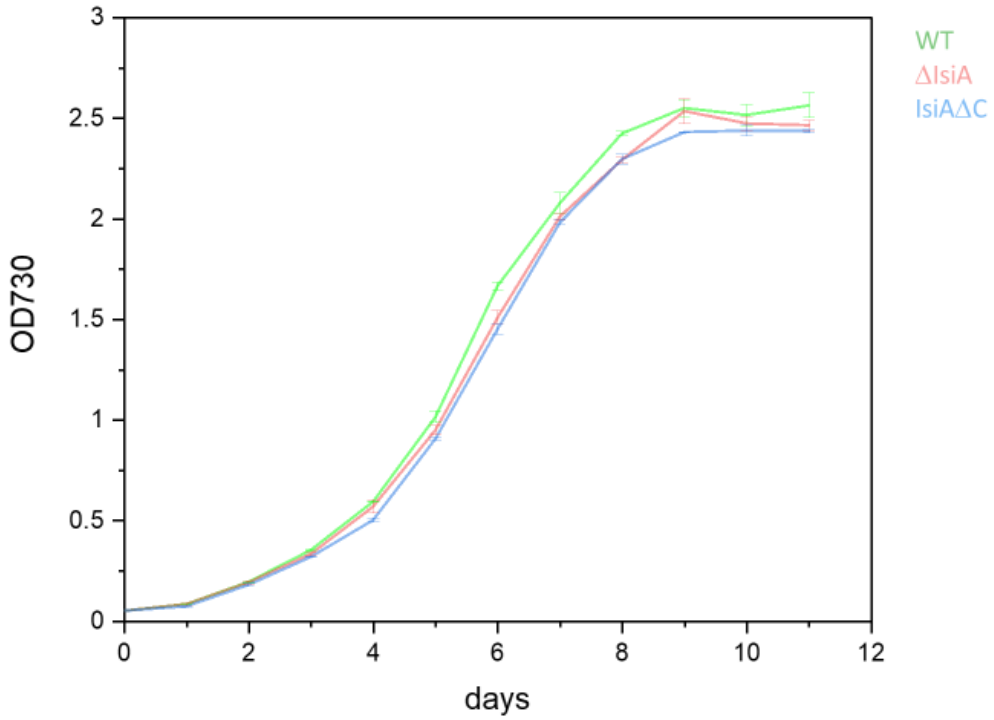

Figure 3.3. Growth rate among WT, IsiAΔC and ΔisiA. Growth curve for *Synechocystis* sp. PCC 6803 wild-type-CM (WT, green), IsiAΔC strains (red) and ΔIsiA strains over the first 7 days of growth. Cells enter early exponential growth at approximately day 3 and continue logarithmic growth until approximately dat 6. All O.D. 730 reading recorded by Cary 4000. Experimental error bars are shown for n = 3.

IsiAΔC expression during iron limited growth.

The response of *Synechocystis SP PCC.6803* to low iron can be measured as a blue-shift of the Qy peak in the cellular absorbance spectrum indicating the expression of IsiA (Andrizhiyevskaya et al. 2002; Duncan et al. 2003). Similarly, IsiAΔC also shows a blue-shifted absorbance from 680 nm to 673 nm on the Qy peak region, validating the expression of IsiA. However, ΔIsiA strain doesn't have this blue-shifted absorbance after iron-starvation of 6 days which is in the logarithm phase of growth rate. (FIGURE 3.4)

The amount of oxidizable P700 can be used to estimate the quantity of PSI in cell and could be measured by a JTS-10 spectrometer (Alric 2010; Alric, Lavergne, and Rappaport 2010). After normalization to OD_{730}, WT, IsiAΔC and ΔIsiA strains at day 0 show similar level of $P700^{+}$, indicating the amount of PSI is similar in all 3 strains under iron-deplete conditions (Figure 3.4C and D). After 6 days of iron starvation, a remarkable drop in PSI quantity (per cellular chl) is observed due to the suppression of PSI expression under iron limited growth. However, no significant changes in the amount of PSI complex per cell was found when comparing among WT, IsiAΔC and ΔIsiA strains, proving that IsiA have no influence on the amount of PSI (Figure 3.4C and D).

When normalized to phycobilisome (PBS) absorbance peak at 625 nm, absorption spectra from all 3 strains show a similar chlorophyll Qy peak with a maximum at 680 nm at day 0. After 6 days of iron starvation, a significant drop in Qy peak intensity was observed in the ΔIsiA compared to WT strains, indicating the chlorophyll loss per PBS. IsiAΔC strains also show a much small drop on Qy peak intensity compared to WT strains suggesting that IsiAΔC is expressed at comparable or slightly slower levels to IsiA. Similarly to wt strains, IsiAΔC strains also has a blue-shift Qy peak (Figure 3.4AB) indicating that the expressed IsiAΔC has a similar effect on cellular absorption to IsiA. Next, we investigated excitation energy distribution IsiAΔC.

Fluorescence can be used to estimate the efficiency of energy transfer between all the components absorbing light, especially from the photoexcited antennae to PSII or PSI. In day 0 WT, IsiAΔC and ΔIsiA strains have similarly shaped cellular chlorophyll fluorescence (Figure 3.5). In day 6, IsiAΔC strain shows a remarkable increasing on the peak as a result of IsiAΔC expression (Figure 3.5). Based on the increasing fluorescence from IsiAΔC, the energy transfer between IsiA and PSI is disrupted.

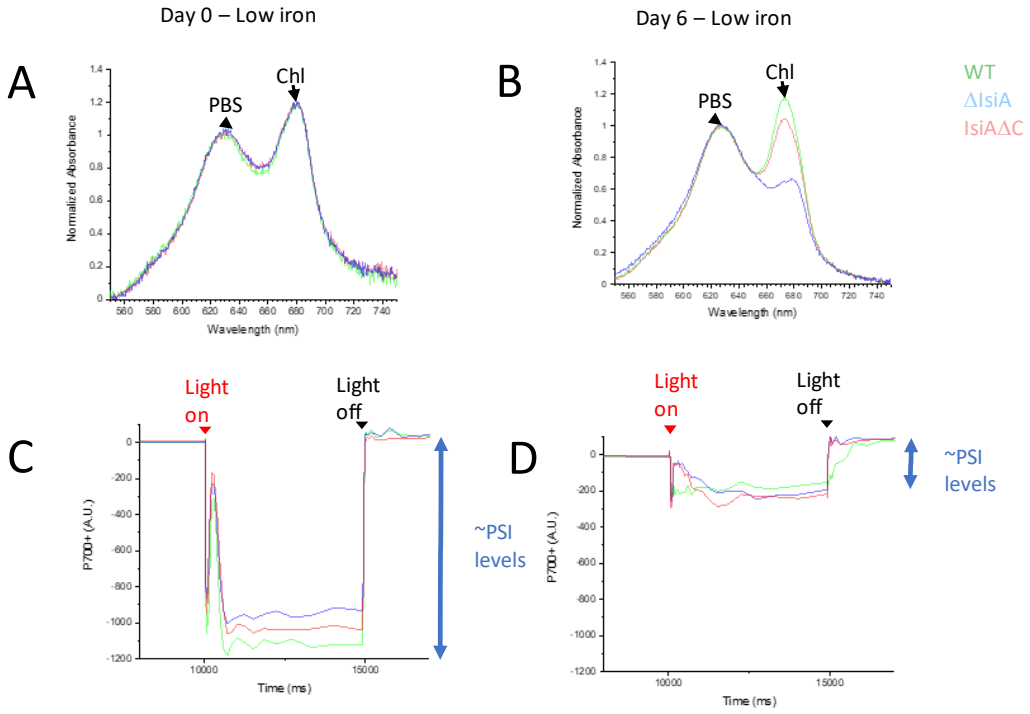

Figure 3.4. Spectroscopic Measurements of WT, IsiAΔC and ΔisiA. A and B: Cell absorbance of wild-type-CM (WT, green), IsiAΔC strains (red) and ΔIsiA strains measurement with integrating sphere. Cell grows under iron deplete condition measured by Cary4000 with integrating sphere. Over 6 days of IsiA induction, after normalized by PBS peak, IsiAΔC shows a drop on Qy peak. C&D: $P700^+$ kinetics measured on JTS-10 pump probe spectrometer. Over 5 days of IsiA induction, PSI levels droped to 1/5 level compared to iron sufficient condition.

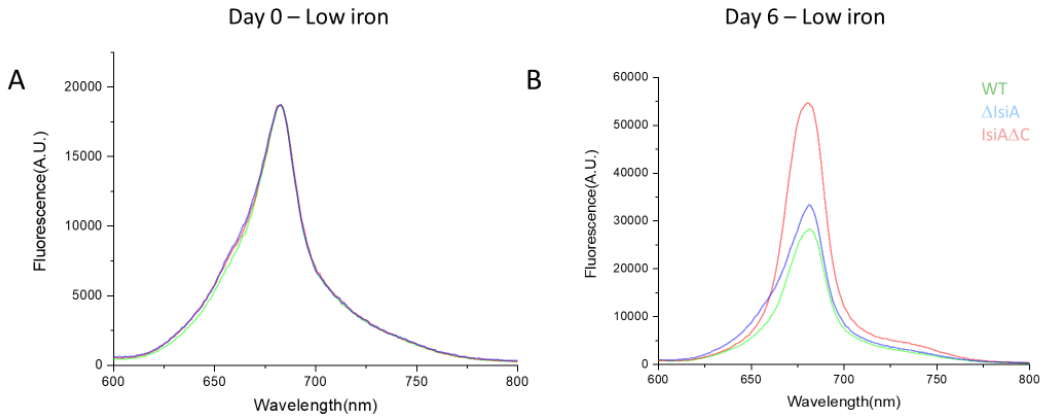

Figure 3.5. Fluorescence of WT, IsiAΔC and ΔisiA. Fluorescence measurement of wild-type-CM (WT, green), IsiAΔC strains (red) and ΔIsiA strains over the first 7 days of growth. All cell normalized by O.D. 730. At first day wild-type-CM (WT, green), IsiAΔC strains (red) and ΔIsiA strain appear to have close fluorescence peak and after 6 days, compared to wild-type-CM (WT, green) and ΔIsiA strains, IsiAΔC strains (red) show high peak of fluorescence.

Energy transfer in IsiAΔC cells

As shown in Figure 3.4 C and D, no significant changes in the amount of PSI per cell could be detected when comparing WT and IsiAΔC strains. The rate of rise of the $P700^+$ signal can be used to measure the functional antennae size of PSI (Bonente et al. 2012, Ballottari et al. 2014). Under limiting light (20 $\mu mol \cdot m^{-2} \cdot s-^{1}$) $P700^+$ kinetic is inversely related to the functional antennae size of PSI-IsiA (Bonente et al. 2012).

Fig. 3.6 shows the kinetics of P700 oxidation by plotting the P700 activity as a function of time. After iron starvation of 7 days, P700 rise kinetics clearly are slower for IsiAΔC strain than for WT strain. Kinetics were fitted with growth functions, and the associated time constants τ were used to calculate the size of the functional antennae (expressed as $1/\tau$) in IsiAΔC samples.

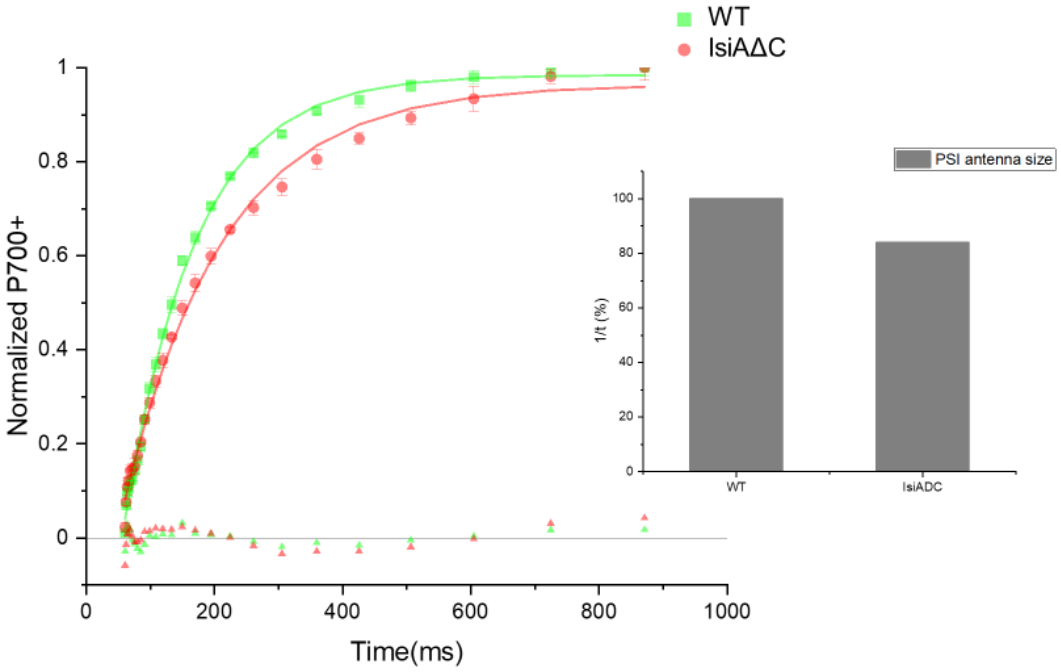

Figure 3.6. Functional antennae size of WT and IsiAΔC. The PSI-related antennae size in WT and IsiAΔC cell was determined by measuring the kinetics of P700 oxidation upon illumination with 15 µmol·m^{-2}·s^{-1}. The kinetics curve was fitted with growth curve characterized by a time constant τ (τWT=1.326 and τIsiAΔC=1.578). Estimation of WT and IsiAΔC antennae size as 1/τ normalized to 100 in the case of WT.

The P700^{+} kinetics of IsiAΔC indicate a 20% decrease in the PSI antennae size compared to the WT. As discussed in the introduction, the C-terminus of IsiA is important in IsiA dimer binding, and this experiment confirms that a deletion of the C-terminus prevents IsiAΔC from forming the full-size antennae with PSI. However, to comprehensively understand the impact of the C-terminus on energy transfer, we employed time-resolved spectroscopy.

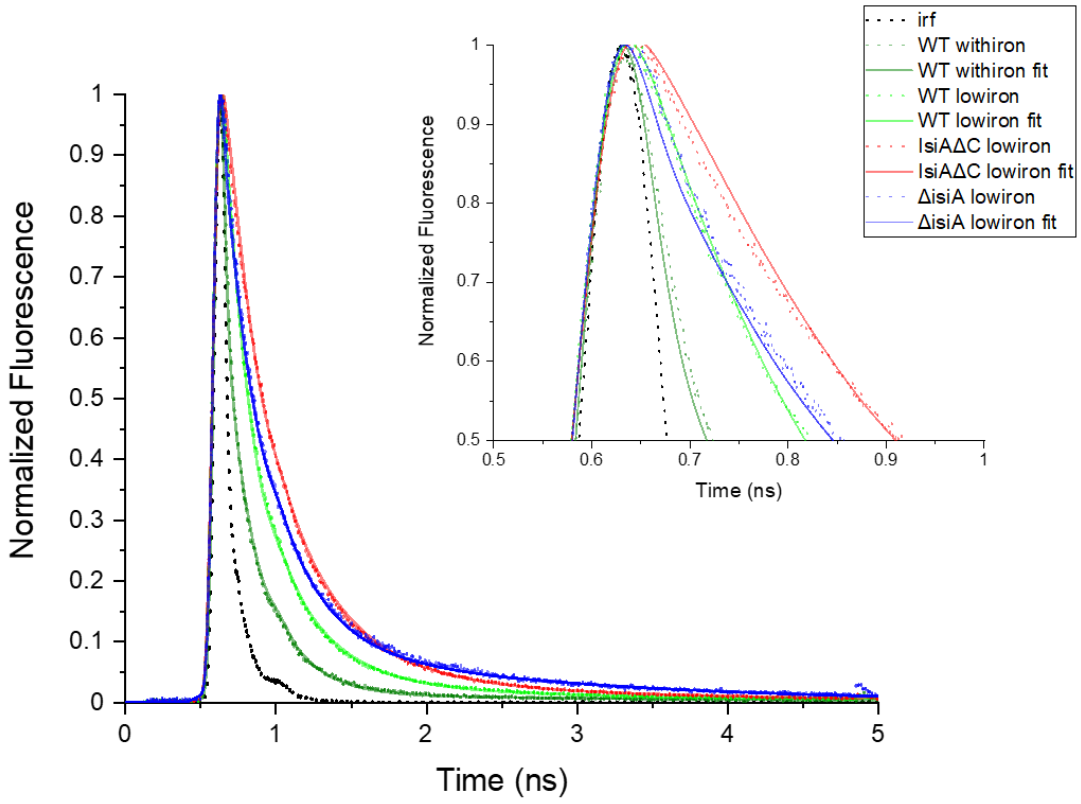

Figure 3.7. Time-resolved fluorescence spectral of WT (iron replete), WT, IsiAΔC and ΔisiA Fluorescence decay measurement of wild-type-CM (WT, iron replete, dark green), wild-type-CM (WT, green), IsiAΔC strains (red) and ΔIsiA strains after 7 days of iron deplete condition. Cells normalized by OD_{730}. Time-resolved fluorescence measured by TCSPC.

	Wild type with iron			Wild type			IsiAΔC			ΔIsiA		
	Life time (ps)	C.I	Amp	Life time (ps)	C.I	Amp	Life time (ps)	C.I	Amp	Life time (ps)	C.I	Amp
t1	18.3	12.2 24.2	0.07382 (92.2%)	66.9	56.5 77.6	0.04601 (79.20%)	78.3	64.8 92.7	0.03835 (64.90%)	32.4	19.7 47.2	0.07682 (78.10%)
t2	227	188 274	0.00606 (7.60%)	360	320 406	0.0114 (19.70%)	406.9	379.5 440.6	0.01945 (32.90%)	286	236.6 352.3	0.01857 (18.90%)
t3	2345	1426 7363	0.0002 (0.20%)	2219	1818 2845	0.0006 (0.10%)	1866	1639.4 2144.7	0.0013 (0.20%)	1713.4	1491.3 2112.6	0.00294 (3%)

Table 3.1. Fit results of Fluorescence Decay measured on WT (iron replete), WT, IsiAΔC and ΔisiA (iron limited). life-times values are indicated in the first column for each measurement, followed by the confidence interval and the amplitude of the component.

To prove that the functional size of PSI antennae from IsiAΔC strain, we decided to use time-resolved fluorescence in vivo. We measured the fluorescence decay kinetics of WT strain and IsiAΔC strain cells in the wavelength regions of 643, 663, 683, 703 and 723 nm at room temperature using TCSPC. The decay kinetics was fitted with three decay components using global analysis and lifetime could be estimated by the fitted fluorescence decay (Holzwarth 1996; van Stokkum, Larsen, and Van Grondelle 2004). Total decay, over all wavelengths, is showed in Figure 3.7 and clearly shows a slower decay on IsiAΔC cells.

Table 1 shows the estimated lifetime from fitted fluorescence decay of WT and IsiAΔC strain cells after global analysis (van Stokkum, Larsen, and Van Grondelle 2004). In the iron-replete, wild type control, (Figure 3.7 dark green) the fastest lifetime, 18.3 ps, is assigned to PSI trapping (Table 3.1). The fastest component in iron limited growth is much longer (66.9 ps) and is associated with trapping in the PSI-IsiA complex. In the IsiAΔC

sample this component increases to 78.3 ps, a 15% increase, suggesting the corresponding decrease in the PSI antennae size, highly similar to the decrease we observed in our $P700^+$ assay for antennaee size.

The second lifetime we observed is typically associated with PSII trapping. Interestingly this lifetime increases in wild type cells from 227 ps in iron replete cultures to 360 ps in iron limited growth. This suggest that transfer to PSII is also modified to some extent under iron limited growth. While IsiA is not known to be associated with PSII, we do observe that this increase in the PSII associated lifetime is reduced in ΔIsiA cells, suggesting that IsiA affects in some way the transfer processes into PSII. In the IsiAΔC sample this second lifetime is even longer then the wild-type sample and was measured at 406 ps. This may reflect some uncoupled IsiA in the thylakoid membranes of these cells as this lifetime resembles measurements that were done on the monomeric form of IsiA (unpublished results from the Mazor lab).

In summary, during logarithm phase of growth curve, IsiAΔC cells exhibit a blue-shift on Qy absorption indicated IsiAΔC expressing. Additionally, compared to WT strain, IsiAΔC strain has higher fluorescence emission, suggesting decreased energy transfer inside PSI-IsiA antenna. The time-resolved fluorescence analysis of IsiAΔC strain reveals that PSI-IsiAΔC antennae have longer lifetime than PSI-IsiA antennae. So, the C-terminus on IsiA is important to form an efficient connection between PSI to IsiA. To further understand the mechanism underlying these interactions within the antenna complex, isolation and purification of the PSI-IsiAΔC complex are necessary.

Isolation of PSI-IsiAΔC

To explore the effect of energy transfer in C-terminus from PSI-IsiAΔC, we isolated the complex through anion exchange chromatography of solubilized thylakoid membranes. The sucrose density gradient analysis revealed chlorophyll-containing proteins, PSI-IsiAΔC, as illustrated in Figure 3.8A. When compared to PSI-trimer sample and PSI-IsiA supercomplex sample from *Synechocystis* 6803, SDS-PAGE analysis displayed similar bands for PSI (PsaA/PsaB) subunits, as depicted in Figure 3.8B. Compared to PSI-IsiA supercomplex, noticeable shifts on IsiA subunits could be observed due to the removal of the last ten amino acids. Additionally, the PSI-IsiAΔC sample exhibited a lower IsiA/PSI ratio, suggesting a potential relationship between the C-terminus and the ability of IsiA to associate with PSI. Further investigation into the differences in PSI-IsiA and PSI-IsiAΔC was conducted on absorption spectra (Figure 3.8C). Compared to the PSI trimer with a Qy maximum at 679 nm, PSI-IsiAΔC exhibit moderate Qy blue-shift (between 675 to 676nm) while PSI-IsiA has the largest Qy blue shift with a maximum at 673 nm. Interestingly, Figure 3.8 shows that PSI-IsiAΔC sample has similar fluorescent emission as PSI-IsiA, we think probably most dropped IsiAΔC compensate the fluorescent emission on PSI-IsiAΔC and we will talk about it in discussion part.

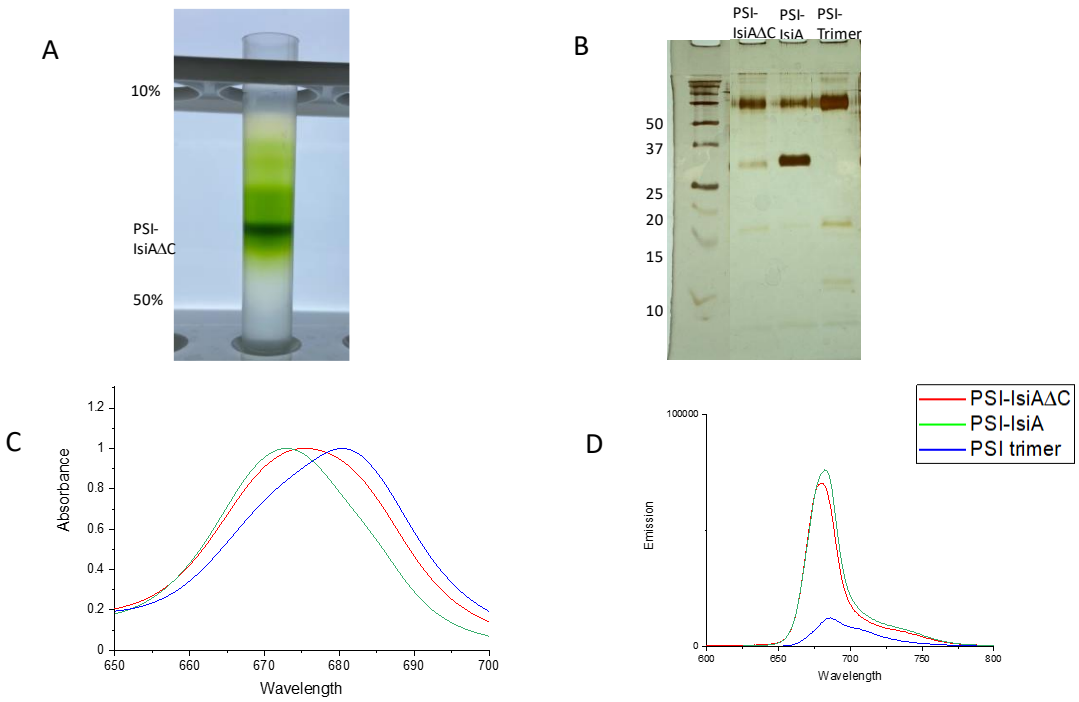

Figure 3.8. Isolation of PSI-IsiAΔC from strain IsiAΔC. Synechocystis SP PCC.6803 IsiAΔC was cultured in glass bottles in 10-L batches using BG11 medium supplemented with 12ng/ml ferric ammonium citrate and 5mM glucose at 30 °C and low intensity light (~15 µE). The cells are harvested after 2.5 weeks. PSI-IsiAΔC complex is isolation by ion exchange column and sucrose gradient. A: sucrose gradient of PSI-IsiAΔC. B: SDS-PAGE gel of PSI-IsiAΔC with PSI-trimer and PSI-IsiA wt. C: Absorbance of PSI-IsiAΔC shows it has the less “blue shift” compared to PSI-IsiA wt. D: Emission of PSI-IsiAΔC was recorded after excitation at 440nm, the fluorescence is similar to PSI-IsiA wt.

The structure of PSI-IsiAΔC

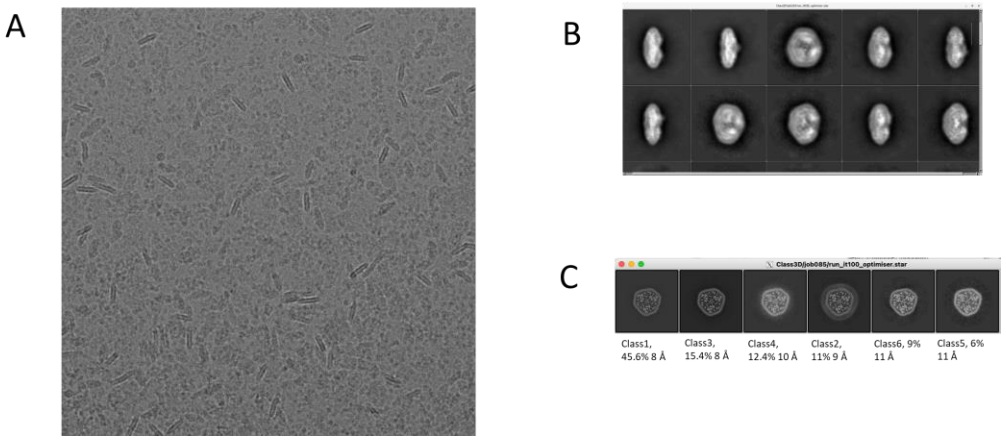

Figure 3.9. The structure of PSI-IsiAΔC. A: A representative micrograph from the Titan Krios electron microscope showing PSI-IsiAΔC in different orientation in vitreous ice. B: 2D-classification results of PSI-IsiAΔC shows different conformation of PSI-IsiAΔC. C: class-3D with alignment of PSI-IsiAΔC.

We used the sample from Figure 3.8A and determined the structure of the PSI-IsiAΔC complex using Cryo-EM (Figure 3.9). We collected 5047 micrographs from Titan Krios electron microscope and the majority of the micrographs contained particles in different orientation in vitreous ice (Figure 3.9A). After several steps of 2D classification we successfully select 10 classes (Figure 3.9b) and extract it from the original micrograph resulting in a set of 88,175 particles as boxes of 650 pixels. This particle set was subjected to 3D classification using an initial PSI–IsiA volume from PSI-IsiA sampled at 60 Å resolution. This procedure yielded 6 classes which clearly showed the complete PSI–IsiAΔC and were grouped together to yield 6460 particles. Due to the low number of

particles, three-dimensional reconstructions using this set yielded volumes at a resolution of 11 Å (Figure 3.9C).

Discussion

Since Joachim Frank developed computational techniques for image analysis (Mitra and Frank 2006) and Richard Henderson contributed to the development of electron microscopy hardware (Henderson et al. 1990), Cryo-EM technology has been utilized for many scientific discoveries. Particularly for structural biologists, Cryo-EM revolutionized the study of protein dynamics, including those involved in photosynthetic antennae such as PSI (Opatíková et al. 2023; Pi et al. 2018; Suga et al. 2020). To adapt to the environment, cyanobacteria utilize a special protein, IsiA to compensate the low iron stress (Yeremenko et al. 2004). After 2001, many group noticed the structure of IsiA, it became evident that the IsiA system possesses a remarkable capacity to form a multitude of assemblies utilizing a single building block (Kouřil, Kouril, et al. 2005). From our last research in chapter 2, we noticed that the architectural flexibility of the IsiA system results from the physical interactions between the N and C terminus of adjacent subunits. The flexibility of the C-terminal helix allows for a variety of IsiA dimers, all while maintaining efficient excitation energy transfer within the IsiA ring (Toporik et al. 2019).

We successfully created IsiAΔC strain and finish a series of spectroscopic measurements. Upon normalized to OD_{730} and excitation at 440 nm, the remarkably high fluorescence of IsiAΔC strain was demonstrated and compared to WT strain. The high fluorescence arises from the antennae difference between WT and IsiAΔC strain. To quantitatively determine the antennae differences between IsiAΔC strain and WT strain, we calculated the size of antennae via measuring the $P700^+$ rise kinetics of IsiAΔC strain and WT strain. After fitting

kinetics curve constant, IsiAΔC strain exhibited 20% decrease in functional antennae size compared to wt strains.

To gain a comprehensive understanding of the influence of the C-terminus on energy transfer, time-resolved spectroscopy was implemented. The fluorescence decay was fitted with three decay components using global analysis. IsiAΔC shows significant slower lifetime (78.3 ps) on the fastest component (τ1) than 66.9 ps in WT. We also noticed an increase lifetime on the second fast component (τ2) from 360 ps to 400 ps in IsiAΔC. From previous studies on fluorescence lifetime in photosystems, it is established that τ1 represents the lifetime of PSI, while τ2 corresponds to PSII.

After removing the final 10 amino acids from IsiA, IsiAΔC demonstrated a slower lifetime of the PSI antennae reflecting disrupted energy transfer between PSI and the IsiA antennae. Though IsiAΔC exhibits a C-terminus similar to that of its homologous PSII subunit, CP43, it remains uncertain if IsiA was associated with PSII in prior investigations (Michel and Pistorius 2004; Y. Zhang et al. 2010). The prolonged τ2 might be attributed to variations in the orientation of the phycobilisomes because lowering the iron concentration affects the expression of phycobilisomes and soluble phycobilisomes are still present in iron-deprived cells. Thus far, no evidence has been obtained to support the utilization of IsiA as an antennae in PSII.

We isolated and purified the PSI-IsiAΔC supercomplexes, which exhibited a diminished blue-shift on the Qy peak compared to PSI-IsiA. Additionally, PSI-IsiAΔC supercomplexes displayed a lower PSI/IsiA ratio, indicating changes in antennae orientation within the PSI-IsiAΔC supercomplexes. The attachment between PSI and IsiAΔC was found to be less tight than in PSI-IsiA, resulting in some IsiAΔC dissociating from PSI. Consequently, PSI-IsiAΔC supercomplexes exhibited similar fluorescence emission to PSI-IsiA when excited at 440nm.

When we put the PSI-IsiAΔC supercomplexes under cryo-EM and process with auto picking and several steps of 2D/3D classification, we only collected 6460 particles from 5047 micrographs due to the dissociation of IsiAΔC from PSI.

In summary, the C-terminus of IsiA is involved in its association with PSI-IsiA and IsiA-IsiA interactions. IsiAΔC demonstrated a reduced antennae size and slower energy transfer rate within PSI-IsiAΔC supercomplexes. However, the deletion of the C-terminus resulted in the dissociation of IsiAΔC, posing challenges in its imaging.

.

Figure supplements

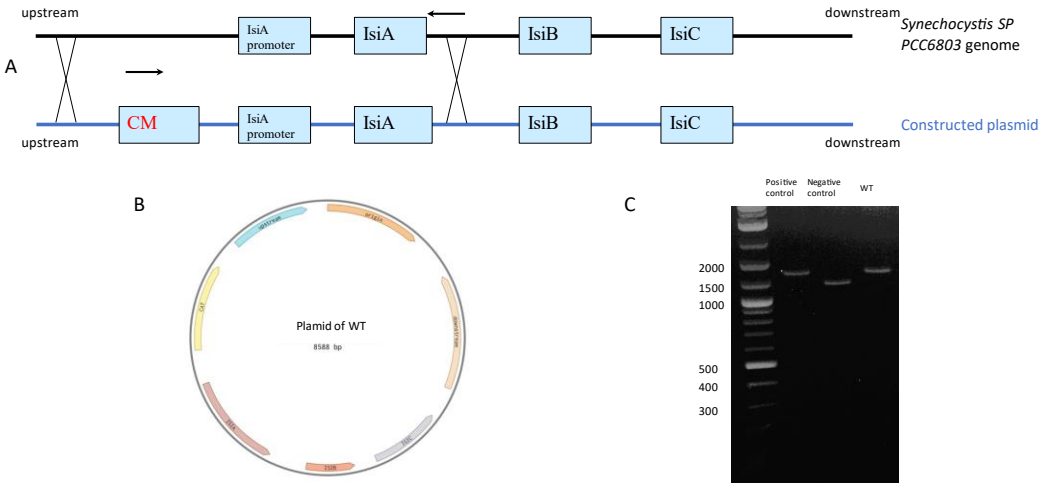

Supplement Figure 3.1. Schematic diagram of WT transformation and agarose gel valiadation: A. Black line as Wild-type synechocystis PCC SP.6803 genome and blue line as constructed plasmid. In constructed plasmid, a Chloramphenicol resistant gene was inserted after IsiA promoter as WT. B. Schematic diagram of plasmids WT map. C: Agarose gel validate chloramphenicol is inserted into genome.

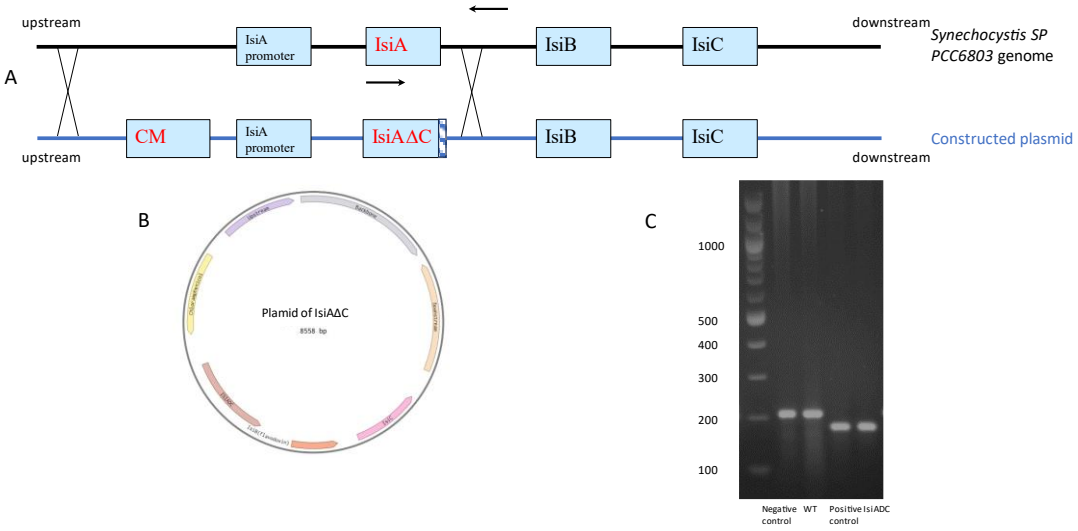

Supplement Figure 3.2. Schematic diagram of IsiAΔC transformation and agarose gel valiadation: A. Black line as Wild-type synechocystis PCC SP.6803 genome and blue line as constructed plasmid. In constructed plasmid, a Chloramphenicol resistant gene was inserted after IsiA promoter and IsiAΔC was inserted to replace IsiA. B. Schematic diagram of plasmids IsiAΔC map. C: Agarose gel validate the IsiAΔC is lack of 30 base pair in the end of IsiA.

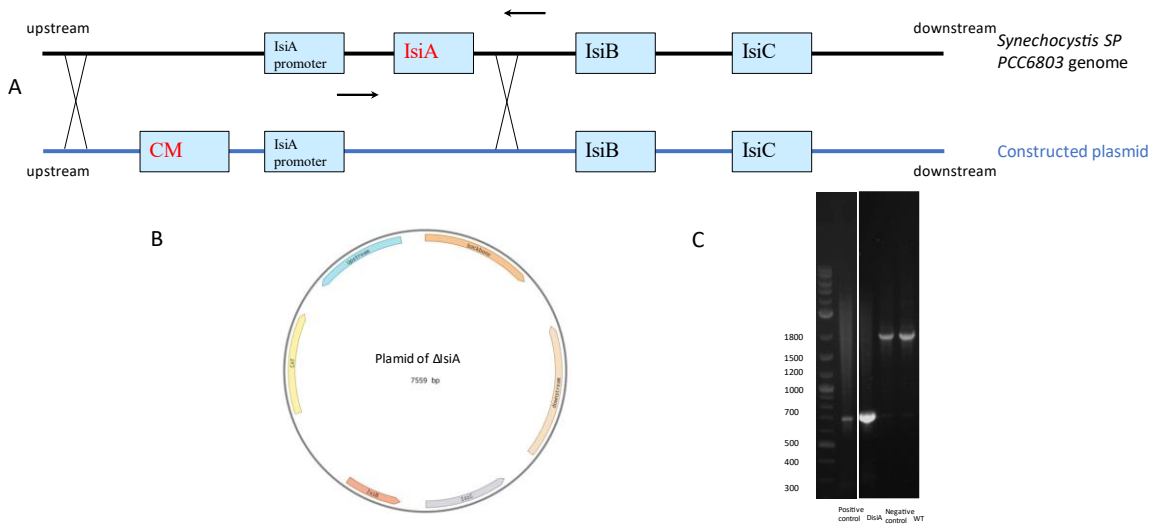

Supplement Figure 3.3. Schematic diagram of ΔIsiA transformation and agarose gel validation: A. Black line as Wild-type *Synechocystis* PCC SP.6803 genome and blue line as constructed plasmid. In constructed plasmid, a Chloramphenicol resistant gene was inserted after IsiA promoter as WT. B. Schematic diagram of plasmids ΔIsiA map. C: Agarose gel validate ΔIsiA missed 1kb bp as IsiA.

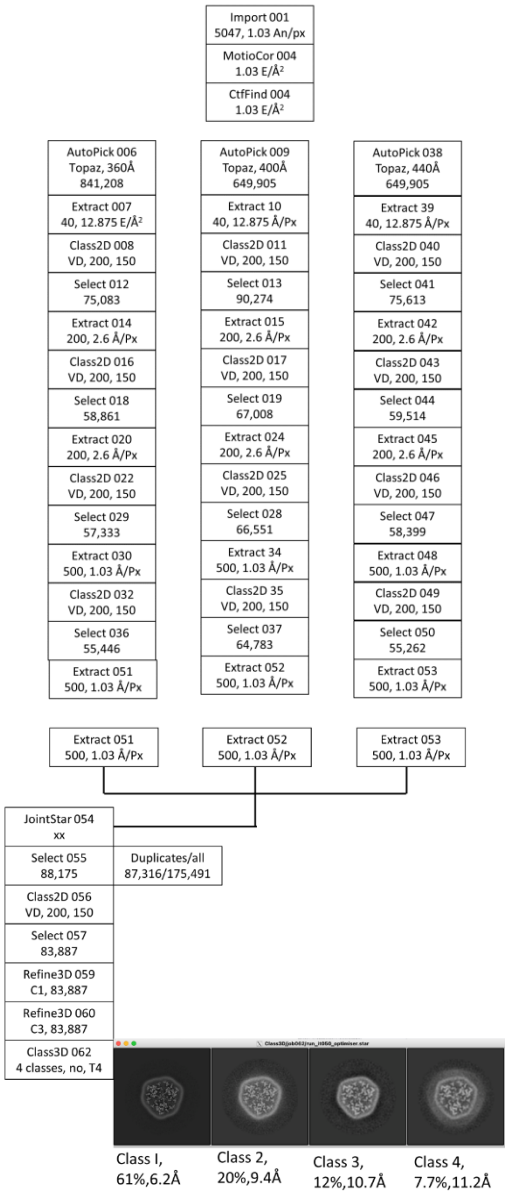

Supplement figure 3.4 Image processing strategy

CHAPTER 4

STRUCTURAL BASIS FOR ENERGY TRANSFER IN THE PSI-ISIA SUPERCOMPLEX.

Jin Li[1,2], Ranel Maqdisi[1,2], Yuval Mazor[1,2]

[1]Biodesign Center for Applied Structural Discover, Arizona State University, Tempe, Arizona, USA

[2]School of molecular Sciences, Arizona State University, Tempe, Arizona, USA

Introduction

Across domains, both PSI and PSII form associations with antennae systems to increase the light cross section(van Amerongen and Croce 2013; Croce and Van Amerongen 2013). In cyanobacteria, phycobilisomes serve as the primary antennae system for PSII and PSI under iron-rich conditions(Mullineaux and Holzwarth 1991). However, bioavailable iron is limited in natural environments outside laboratory settings. In such iron-deficient conditions, cyanobacteria adapted to utilize an antennae protein family known as iron stress-induced (IsiA) proteins, with IsiA being particularly prominent(Andrizhiyevskaya et al. 2002; Burnap, Troyan, and Sherman 1993). In Chapter 2, we determined the high-resolution structure of the PSI-IsiA antennae supercomplex from Synechocystis sp. PCC 6803, achieving a resolution of 3.5 Å using cryogenic transmission electron microscopy (Cryo-EM)(Toporik et al. 2019). The PSI-IsiA supercomplex exhibits a disk-shaped structure with a diameter of 300 Å and a height of 100 Å, displaying three-fold rotational symmetry (Figure 2.6).

IsiA has been called CP43' since it was discovered because of highly homology to CP43 in PSII(T S Bibby, Nield, and Barber 2001; Duncan et al. 2003). While the IsiA monomer

closely resembles the overall conformation of the CP43 subunit found in PSII, there are three notable differences in IsiA, a shortened E loop between helixes V and VI, a different confirmation of the C-terminus and 4 additional chlorophylls and 1 additional carotenoid in IsiA (Figure 3.1). In IsiA, the shortened E loop allows for the coordination of a unique chlorophyll, Chl17 (Toporik et al. 2019).The extended E loop in CP43 connects helices V and VI and connects CP43 to the oxygen evolving complex in PSII, sterically blocking the space where this chlorophyll would occupy (Nelson and Yocum 2006). Currently the role of Chl17 in IsiA is unknown, however its proximity to both chlorophylls located in PSI and chlorophylls in adjacent monomers of IsiA suggests it is crucial for energy transfer (Figure 3.1) (Toporik et al. 2019). Another major difference of IsiA to CP43 is the number of chlorophylls bound to the transmembrane helices. The PSI-IsiA super complex revealed that each monomer of IsiA contains 4 additional chlorophylls relative to CP43 (Figure 3.1B, colored in blue). Interestingly, an additional carotenoid is also positioned at the interface between IsiA and PSI (Figure 3B). Determining the functional significance of these additional pigments presents a significant challenge due to the heterogeneous nature of IsiA assemblies *in vivo* and *in vitro*.

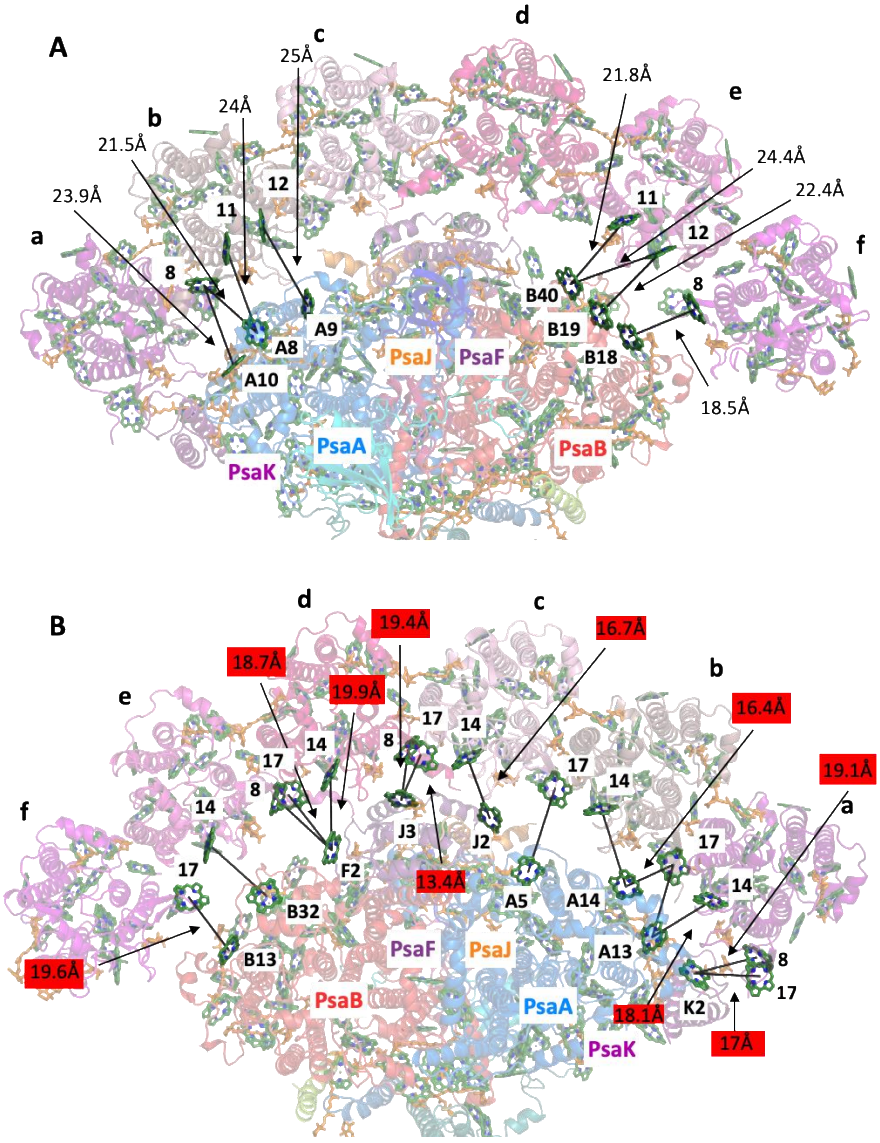

Figure 4.1. Lumenal chlorophylls facilitate excitation energy transfer from IsiA to PSI. (A) Stromal view showing one PSI monomer with the corresponding IsiA hexamer. The closest chlorophylls connecting IsiA to PSI are shown in green, other pigments are shown as background. All Mg to Mg distances shorter than 25 Å are shown as black lines, pair B18-f8 is the closest PSI-IsiA connection,

separated by 18.5 Å, the rest of the distances are in the 21-25 Å range (Supplement table 2.1). (B) View from the lumenal side shows a much denser network of connecting chlorophylls between IsiA and PSI. Most connections are made between three IsiA chlorophylls (17,14 and 8) and PSI pigments. The closest distances between the IsiA chlorophylls and the PSI chlorophylls on different subunits are indicated (Supplement table 2.1).

Energy transfer rates in photosynthetic systems are affected by many variables, however the distance between donor and acceptor is one of the most dominating factors(Clegg 2009; Sahoo 2011). At the current resolution, the PSI-IsiA model still lacks important details, such as a complete atomic description of each pigment and precise locations of each amino acid. Regardless, distances between pigments can be calculated with a high degree of confidence. In this work, we found that chlorophyll 8 (Chl 8) and chlorophyll 17(Chl 17) show the closest distance to PSI trimer (Figure 4.1). Figure 4.1A shows on stromal side, Chl 8 have the closest distance at IsiAb and IsiAf to PSI trimer at PsaA A8 and PsaB B18 at 21.5 Å and 18.5 Å respectively. Meanwhile, figure 4.1B illustrates Chl 17 has even closer distance to PSI trimer on luminal side from IsiAc to PsaF at 13.4 Å. Moreover, compared to other chlorophylls, Chl 8 and 17 were observed more compact to PSI on all IsiA subunits.

Despite the comprehensive information provided earlier, mutational analysis remains essential for identifying key factors involved in energy transfer. Therefore, we have generated mutants targeting chlorophyll coordinating side chains, resulting in chlorophyll 8 and 17 loss, and have assessed the impact of these mutations.

Methods

Design of ΔChl8 and ΔChl17

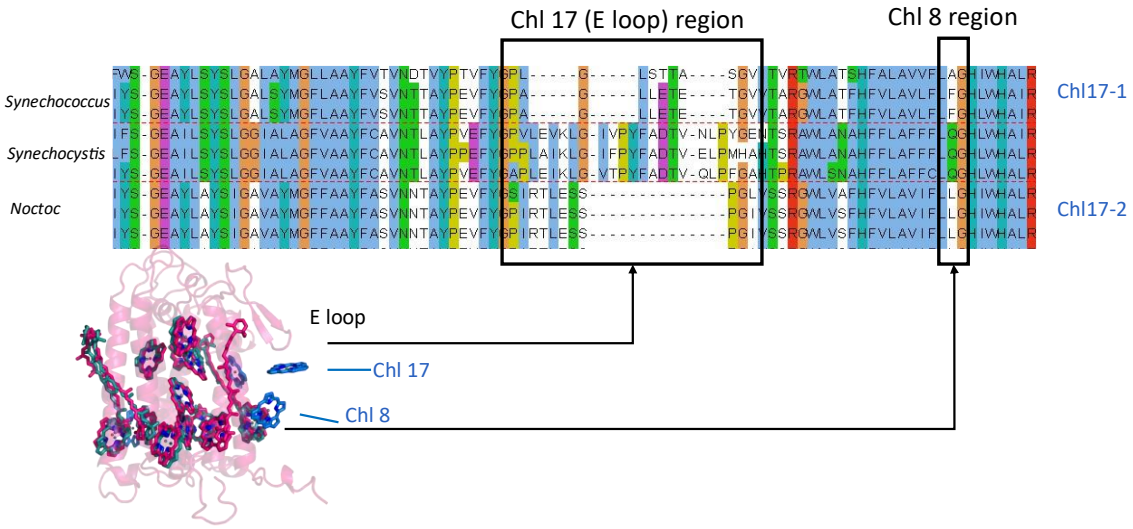

Figure 4.2. Part of alignment result of IsiA on Synechocystis sp. PCC 6803. We labeled chlorophyll 17 and chlorophyll 8 region on IsiA sequence. We found three different IsiA family in 500 alignments with unique E loop. One of these three family have similar E loop to IsiA from Synechocystis sp. PCC 6803, and IsiA family1 and IsiA family2 are two IsiA family we found have shortened E loop without Chl17.

After analyzing the chlorophyll-associated side chains on IsiA (refer to Supplement Table 2.2), we conducted an alignment of 500 IsiA homologous genes from the protein bank. Among these, two families from *Synechococcus* and *Nostoc* stood out for exhibiting a shortened E-loop and lacking the Chl 8 coordinating side chain Q316 simultaneously. As a result, we decided to replace Q316 with alanine (A) to create ΔChl8 and selected families from *Synechococcus* and *Nostoc* to create ΔChl17_1 and ΔChl17_2.

Construction of IsiA mutations

The Δchl8 mutation was constructed into WT by creating a point mutation observed in sequence alignment using the 8_UP and 8_Down primer pairs and WT as a template. The

two fragments were assembled using the NEBuilder® HiFi DNA Assembly Master Mix. All plasmids were sequenced before being used to transform Synechocystis sp. PCC6803 according to standard protocols. Complete and correct replacement of all aspects was verified by PCR and sequencing.

The ∆chl17 mutation 1 and 2 was constructed into p60 via adding the loop sequence observed in *Synechococc*us and *noctoc* using the chl17_1_UP, chl17_1_DOWN, chl17_2_UP and chl17_2_DOWN and WT strain as template.

All primer sequences are listed in Supplementary table 4.1.

Culture conditions, complex isolation and measurments were done similary to chapter 2 and 3 unless indicated otherwise.

Results

The response of *Synechocystis* 6803 to low iron conditions manifests in blue-shifted absorbance spectra at the Qy peak, indicative of the formation of a new chlorophyll-abundant antennae (Kouřil, Kouril, et al. 2005; Melkozernov et al. 2003). We use WT and ∆IsiA from chapter 3 as positive and negative controls in this analysis and measure the absorbance spectra. Similarly, when normalized to Qy peak, IsiA∆Chl17_1 and ∆Chl17_2 also exhibited a weakened and blue-shifted absorbance (Figure 4.3A and B), transitioning from 680 nm to 675 nm, confirming the expression of IsiA. Meanwhile, compared to WT (Figure 4.3C), we also noticed a slower transition on Phycobilisome peak (625nm) from IsiA∆Chl17_1and the IsiA∆Chl17_2 after 7 days of iron starvation. However, ∆IsiA strain does not display this blue-shifted absorbance following 6 days of iron-starvation during the logarithmic phase of growth and ∆IsiA strain has even high PBS peak after 6 days (Figure 4.3D).

The blue-shift absorption observed at the Qy peak signifies the expression of IsiA, while the appearance of the phycobilisome (PBS) peak on day 6 suggests that the orientation of the phycobilisome is influential under iron starvation conditions. To understand the functioning of the IsiAΔChl17 antennae in conjunction with PSI, we opted to employ sucrose gradient density analysis.

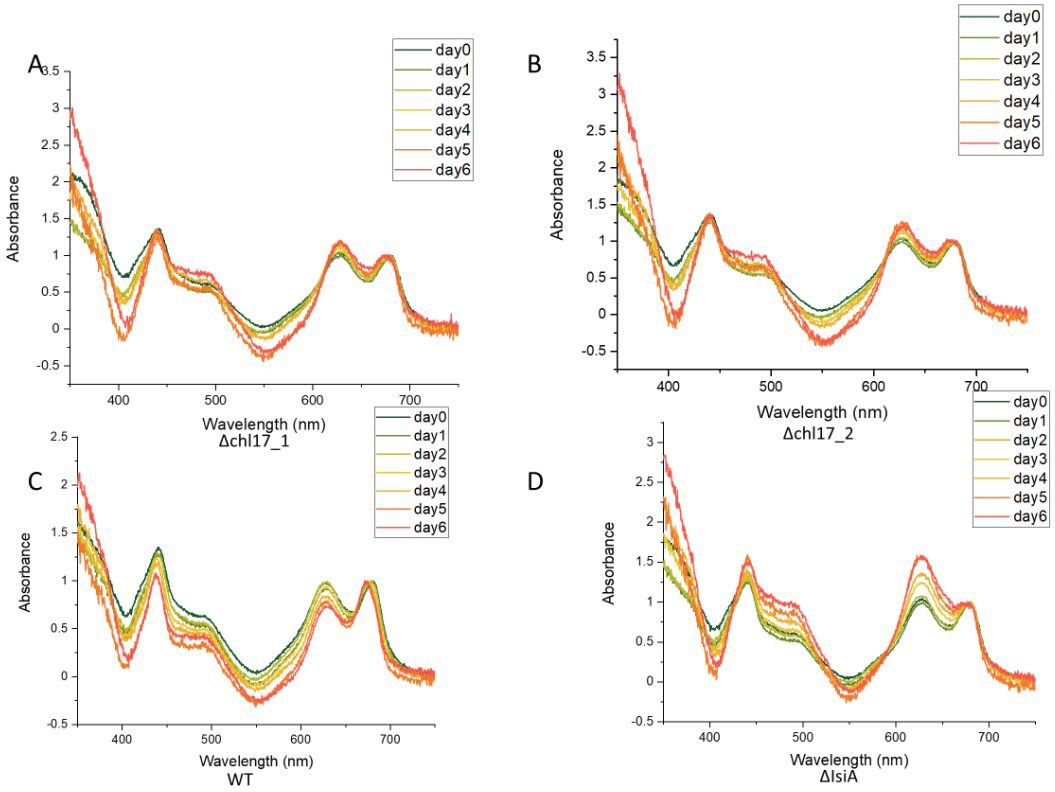

Figure 4.3. Normalized (on the maximum of Qy) absorption spectra of IsiAΔChl17_1, IsiAΔChl17_2, WT and ΔIsiA under iron starvation condition. Day0 is labeled in green while day6 is labeled orange. PBS peak change could be easily observed after day 6.

After six days of iron starvation, 50ml of cyanobacterial cells from IsiAΔChl17_1, IsiAΔChl17_2, WT, and ΔIsiA strains were harvested. Subsequently, the harvested cells

were resuspended in STN1 buffer and disrupted by shaking with glass beads. Membranes were then collected via ultracentrifugation at 45,000g for 2 hours. Following solubilization with DDM (n-Dodecyl β-D-maltoside) at a ratio of 10:1, insoluble material was removed through ultracentrifugation. The solubilized membranes were loaded onto a 12–60% sucrose density gradient, as depicted in Figure 4.4.

Compared to the WT strain, both IsiAΔChl17_1 and IsiAΔChl17_2 strains exhibit a lack of the heaviest band at the bottom, which corresponds to the PSI-IsiA supercomplexes. However, the composition of bands in IsiAΔChl17_1 and IsiAΔChl17_2 strains is similar to that of the ΔIsiA strain. The PSI-IsiA is not visible in this sucrose gradient with PSI even though the absorbance from IsiAΔChl17_1 and IsiAΔChl17_2 (Figure 4.3AB) validated the expression of IsiA. After knocking out the chl 17 in IsiA, the association from PSI-IsiA is broken and it leads to disruption of PSI-IsiA supercomplexes.

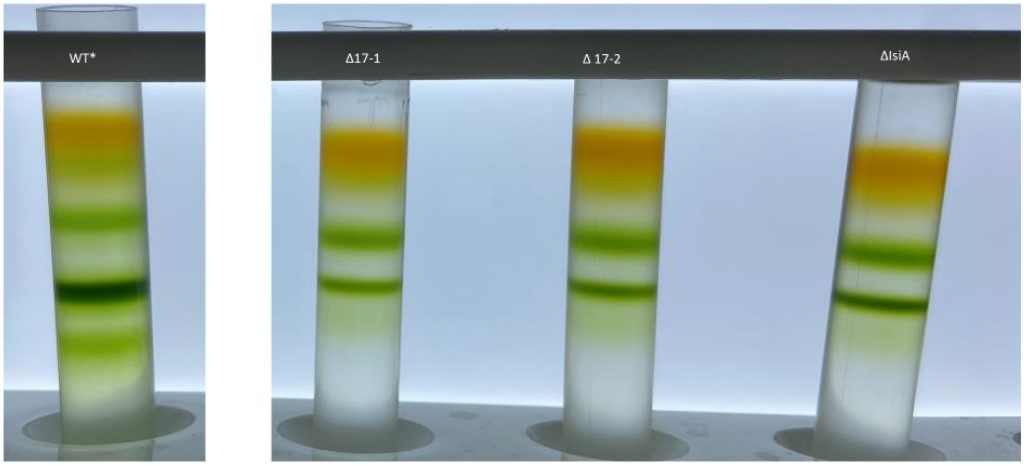

Figure 4.4. Sucrose gradient fraction of dissolved membrane with DDM from IsiAΔChl17_1, IsiAΔChl17_2, WT and ΔIsiA under iron starvation condition. Compared to WT, IsiAΔChl17_1, IsiAΔChl17_2 and ΔIsiA are lack of the bottom PSI-IsiA large band.

Discussion

In our prior analysis outlined in Chapter 2, we observed that chlorophylls 17 and 8, which are specific to IsiA, exhibit the shortest distances with chlorophylls coordinated by the adjacent subunit from the PSI side.

In summary, we successfully created ΔChl17_1, IsiAΔChl17_2 mutations by using alignment from 500 IsiA homologous genes. ΔChl17_1, IsiAΔChl17_2 could express IsiA under iron stress conditions, but they induce PBS at the same time. After solubilization into DDM and loading onto sucrose density gradient, ΔChl17_1, IsiAΔChl17_2 reveal chl 17 play a crucial role in binding of PSI and IsiA.

CHAPTER 5

CONCLUDING REMARKS AND FUTURE OUTLOOK

Jin Li[1,2], Ranel Maqdisi[1,2], Yuval Mazor[1,2]

[1]Biodesign Center for Applied Structural Discover, Arizona State University, Tempe, Arizona, USA

[2]School of molecular Sciences, Arizona State University, Tempe, Arizona, USA

Proteins play indispensable roles in various biological processes within all cells including catalyzing, regulation and comprising structural elements or in numerous other physiological functions. Consequently, comprehending the mechanisms by which proteins operate becomes highly desirable. The structure of protein heavily influences its functional characteristics, along with the specific arrangement of its constituent residues. By solving the three-dimensional arrangement of atoms within a protein, we gain insights into its biological role and how it interacts with other molecules. In addition, solving protein structures is crucial for advancing our understanding of biology, developing new therapeutics, improving biotechnological processes, uncovering evolutionary relationships, and diagnosing diseases.

Since 2001, the interaction between PSI and IsiA has been widely acknowledged. In this dissertation, I provided a summary of previously published work that focused on IsiA properties. To determine the structure of PSI-IsiA, I optimized the iron concentration to promote IsiA expression and applied this optimized condition for cultivating IsiA mutants. I also generated several mutants to investigate the functional connections between IsiA and PSI on the C-terminus and chlorophyll 17 of IsiA.

However, the functional role of IsiA assemblies in the absence of PSI, as well as their potential interaction with PSII, remain unresolved. Notably, the remarkable flexibility of the

IsiA-PSI interaction is a key consideration. This flexibility is evident on multiple levels. Firstly, IsiA has been observed to form multiple rings surrounding a single PSI trimer, as evidenced by low-resolution techniques such as TEM and SEM. Secondly, IsiA can associate with PSI mutants, including those lacking identified PSI binding surfaces in the PSI-IsiA supercomplex, as well as mutants forming only monomers. Moreover, in certain cyanobacteria, an IsiA-PsaL fusion protein is present, which, along with two additional IsiA variants, can form a native monomeric PSI-IsiA complex. Overall, it is evident that IsiA arrays can form around different central cores (PSI trimers, monomers, and mutants) and, in some cases, can exist independently as crescents or circles.

It has been an incredible journey to be immersed in the research of IsiA with Cryo-EM technologies. It’s fortunate to have had the opportunity to make contributions to these groundbreaking fields. In the coming years, as advancements in microscopy technology enable enhanced protein observation capabilities, structural biology might carry relatively less significance in the broader scientific community, it holds immense personal meaning for me.

REFERENCES

Adams, Paul D., Pavel V. Afonine, Paul D. Adams, G. Bunkóczi, Pavel V. Afonine, Gábor Bunkóczi, Vincent B. Chen, et al. 2010. “PHENIX: A Comprehensive Python-Based System for Macromolecular Structure Solution.” *Acta Crystallographica Section D-biological Crystallography*. doi:10.1107/s0907444909052925.

Afonine, PV, JJ Headd, TC Terwilliger, and PD Adams. 2013. “New Tool: Phenix. Real_space_refine.” *Computational Crystallography Newsletter* 4(2): 43–44.

Akimoto, Seiji, Makio Yokono, Fumiya Hamada, Ayaka Teshigahara, Shimpei Aikawa, and Akihiko Kondo. 2012. “Adaptation of Light-Harvesting Systems of Arthrospira Platensis to Light Conditions, Probed by Time-Resolved Fluorescence Spectroscopy.” *Biochimica et Biophysica Acta (BBA)-Bioenergetics* 1817(8): 1483–89.

Allen, John F. 2003. “Cyclic, Pseudocyclic and Noncyclic Photophosphorylation: New Links in the Chain.” *Trends in plant science* 8(1): 15–19.

Alric, Jean. 2010. “Cyclic Electron Flow around Photosystem I in Unicellular Green Algae.” *Photosynthesis research* 106: 47–56.

Alric, Jean, Jérôme Lavergne, and Fabrice Rappaport. 2010. “Redox and ATP Control of Photosynthetic Cyclic Electron Flow in Chlamydomonas Reinhardtii (I) Aerobic Conditions.” *Biochimica et Biophysica Acta (BBA)-Bioenergetics* 1797(1): 44–51.

van Amerongen, Herbert, and Roberta Croce. 2013. “Light Harvesting in Photosystem II.” *Photosynthesis research* 116: 251–63.

van Amerongen, Herbert, and Rienk van Grondelle. 2001. “Understanding the Energy Transfer Function of LHCII, the Major Light-Harvesting Complex of Green Plants.” *The journal of physical chemistry B* 105(3): 604–17.

Andrizhiyevskaya, Elena G., Elena G. Andrizhiyevskaya, Tatjana M. E. Schwabe, Tatjana M. E. Schwabe, M. Germano, Marta Germano, Sandrine D’Haene, et al. 2002. “Spectroscopic Properties of PSI-IsiA Supercomplexes from the Cyanobacterium Synechococcus PCC 7942.” *Biochimica et Biophysica Acta*. doi:10.1016/s0005-2728(02)00371-7.

Andrizhiyevskaya, Elena G., Dmitrij Frolov, Elena G. Andrizhiyevskaya, Rienk van Grondelle, Dmitrij Frolov, Dmitrij Frolov, Jan Dekker, Rienk van Grondelle, and Jan P. Dekker. 2004. “Energy Transfer and Trapping in the Photosystem I Complex of Synechococcus PCC 7942 and in Its Supercomplex with IsiA.” *Biochimica et Biophysica Acta*. doi:10.1016/j.bbabio.2004.02.002.

Antoshvili, Maya, Maya Antoshvili, Ido Caspy, Ido Caspy, Michael Hippler, Michael Hippler, Nathan Nelson, and Nathan Nelson. 2019. “Structure and Function of

Photosystem I in Cyanidioschyzon Merolae." *Photosynthesis Research*. doi:10.1007/s11120-018-0501-4.

Bai, Xiao-Chen, Greg McMullan, and Sjors HW Scheres. 2015. "How Cryo-EM Is Revolutionizing Structural Biology." *Trends in biochemical sciences* 40(1): 49–57.

Baker, Lindsay A, and John L Rubinstein. 2010. "Radiation Damage in Electron Cryomicroscopy." In *Methods in Enzymology*, Elsevier, 371–88.

Ballottari, Matteo, Marcelo JP Alcocer, Cosimo D'Andrea, Daniele Viola, Tae Kyu Ahn, Annamaria Petrozza, Dario Polli, et al. 2014. "Regulation of Photosystem I Light Harvesting by Zeaxanthin." *Proceedings of the National Academy of Sciences* 111(23): E2431–38.

Barber, J, and MD Archer. 2001. "P680, the Primary Electron Donor of Photosystem II." *Journal of Photochemistry and Photobiology A: Chemistry* 142(2–3): 97–106.

Battchikova, Natalia, Julia P Vainonen, Natalia Vorontsova, Mika Keranen, Dalton Carmel, and Eva-Mari Aro. 2010. "Dynamic Changes in the Proteome of Synechocystis 6803 in Response to CO2 Limitation Revealed by Quantitative Proteomics." *Journal of Proteome Research* 9(11): 5896–5912.

Beale, Samuel I. 1993. "Biosynthesis of Phycobilins." *Chemical reviews* 93(2): 785–802.

Ben-Shem, Adam, Felix Frolow, and Nathan Nelson. 2003. "Crystal Structure of Plant Photosystem I." *Nature* 426(6967): 630–35.

Bepler, Tristan, Kotaro Kelley, Alex J Noble, and Bonnie Berger. 2020. "Topaz-Denoise: General Deep Denoising Models for cryoEM and cryoET." *Nature communications* 11(1): 5208.

Bepler, Tristan, Andrew Morin, Micah Rapp, Julia Brasch, Lawrence Shapiro, Alex J. Noble, and Bonnie Berger. 2019. "Positive-Unlabeled Convolutional Neural Networks for Particle Picking in Cryo-Electron Micrographs." *Nature Methods* 16(11): 1153–60. doi:10.1038/s41592-019-0575-8.

Berera, Rudi, Ivo H. M. van Stokkum, Rudi Berera, John T. M. Kennis, Ivo H. M. van Stokkum, Yuanjian Zhang, John T. M. Kennis, et al. 2010. "The Light-Harvesting Function of Carotenoids in the Cyanobacterial Stress-Inducible IsiA Complex." *Chemical Physics*. doi:10.1016/j.chemphys.2010.01.011.

Bibby, T S, J Nield, and J Barber. 2001. "Three-Dimensional Model and Characterization of the Iron Stress-Induced CP43'-Photosystem I Supercomplex Isolated from the Cyanobacterium Synechocystis PCC 6803." *The Journal of biological chemistry* 276(46): 43246–52. doi:10.1074/jbc.M106541200.

Bibby, Thomas S., Thomas S. Bibby, Isabelle Mary, Isabelle Mary, I. Mary, I. Mary, Jon Nield, et al. 2003. "Low-Light-Adapted Prochlorococcus Species Possess Specific Antennae for Each Photosystem." *Nature*. doi:10.1038/nature01933.

Bibby, Thomas S., Jon Nield, Thomas S. Bibby, James Barber, Jon Nield, and James Barber. 2001. “Iron Deficiency Induces the Formation of an Antenna Ring around Trimeric Photosystem I in Cyanobacteria.” *Nature*. doi:10.1038/35089098.

Blankenship, Robert E. 2021. *Molecular Mechanisms of Photosynthesis*. John Wiley & Sons.

Blankenship, Robert E., and Robert E. Blankenship. 1992a. “Origin and Early Evolution of Photosynthesis.” *Photosynthesis Research*. doi:10.1007/bf00039173.

Blankenship, Robert E., and Robert E. Blankenship. 1992b. “Origin and Early Evolution of Photosynthesis.” *Photosynthesis Research*. doi:10.1007/bf00039173.

Blankenship, Robert E., and Robert E. Blankenship. 2002. “Molecular Mechanisms of Photosynthesis.” *null*. doi:10.1002/9780470758472.

Blankenship, Robert E., and Robert E. Blankenship. 2010. “Future Perspectives in Plant Biology Early Evolution of Photosynthesis 1.” *null*. doi:null.

Bonente, Giulia, Sara Pippa, Stefania Castellano, Roberto Bassi, and Matteo Ballottari. 2012. “Acclimation of Chlamydomonas Reinhardtii to Different Growth Irradiances.” *Journal of Biological Chemistry* 287(8): 5833–47.

Büchel, Claudia, and Claudia Büchel. 2015. “Evolution and Function of Light Harvesting Proteins.” *Journal of Plant Physiology*. doi:10.1016/j.jplph.2014.04.018.

Buick, Roger. 2008. “When Did Oxygenic Photosynthesis Evolve?” *Philosophical Transactions of the Royal Society B: Biological Sciences* 363(1504): 2731–43.

Burnap, R. L., T. Troyan, and L. A. Sherman. 1993. “The Highly Abundant Chlorophyll-Protein Complex of Iron-Deficient Synechococcus Sp. PCC7942 (CP43’) Is Encoded by the isiA Gene.” *Plant Physiology* 103(3): 893–902. doi:10.1104/pp.103.3.893.

Chauhan, Devendra Kumar, Devendra K. Chauhan, I. Mihaela Folea, I. Mihaela Folea, Craig C. Jolley, Craig C. Jolley, Roman Kouřil, et al. 2011. “A Novel Photosynthetic Strategy for Adaptation to Low-Iron Aquatic Environments.” *Biochemistry*. doi:10.1021/bi1009425.

Chen, Hui-Yuan S., Hui-Yuan S. Chen, Michelle Liberton, Himadri B. Pakrasi, Michelle Liberton, Dariusz M. Niedzwiedzki, Himadri B. Pakrasi, and Dariusz M. Niedzwiedzki. 2017. “Reevaluating the Mechanism of Excitation Energy Regulation in Iron-Starved Cyanobacteria.” *Biochimica et Biophysica Acta*. doi:10.1016/j.bbabio.2017.01.001.

Chen, Min, Martin Schliep, Robert D Willows, Zheng-Li Cai, Brett A Neilan, and Hugo Scheer. 2010. “A Red-Shifted Chlorophyll.” *Science* 329(5997): 1318–19.

Cheng, Anchi, Edward T Eng, Lambertus Alink, William J Rice, Kelsey D Jordan, Laura Y Kim, Clinton S Potter, and Bridget Carragher. 2018. “High Resolution Single Particle Cryo-Electron Microscopy Using Beam-Image Shift.” *Journal of structural biology* 204(2): 270–75.

Cheng, Yifan. 2015. “Single-Particle Cryo-EM at Crystallographic Resolution.” *Cell* 161(3): 450–57.

Chmeliov, Jevgenij, Andrius Gelzinis, Egidijus Songaila, Ramūnas Augulis, Christopher DP Duffy, Alexander V Ruban, and Leonas Valkunas. 2016. “The Nature of Self-Regulation in Photosynthetic Light-Harvesting Antenna.” *Nature plants* 2(5): 1–7.

Chukhutsina, Volha U, Alfred R Holzwarth, and Roberta Croce. 2019. “Time-Resolved Fluorescence Measurements on Leaves: Principles and Recent Developments.” *Photosynthesis Research* 140(3): 355–69.

Clegg, Robert M. 2009. “Förster Resonance Energy Transfer—FRET What Is It, Why Do It, and How It’s Done.” *Laboratory techniques in biochemistry and molecular biology* 33: 1–57.

Croce, Roberta, and Herbert Van Amerongen. 2014. “Natural Strategies for Photosynthetic Light Harvesting.” *Nature Chemical Biology* 10(7): 492–501. doi:10.1038/nchembio.1555.

Croce, Roberta, and Herbert Van Amerongen. 2013. “Light-Harvesting in Photosystem I.” *Photosynthesis Research* 116: 153–66.

DalCorso, Giovanni, Paolo Pesaresi, Simona Masiero, Elena Aseeva, Danja Schünemann, Giovanni Finazzi, Pierre Joliot, Roberto Barbato, and Dario Leister. 2008. “A Complex Containing PGRL1 and PGR5 Is Involved in the Switch between Linear and Cyclic Electron Flow in Arabidopsis.” *Cell* 132(2): 273–85.

Di Donato, Mariangela, and Marie Louise Groot. 2015. “Ultrafast Infrared Spectroscopy in Photosynthesis.” *Biochimica et Biophysica Acta (BBA)-Bioenergetics* 1847(1): 2–11.

Dobson, Zachary. 2022. “A Structure Guided Approach to Understanding Photosynthetic Membrane Proteins.” PhD Thesis.

Dubochet, Jacques, Marc Adrian, Jiin-Ju Chang, Jean-Claude Homo, Jean Lepault, Alasdair W McDowall, and Patrick Schultz. 1988. “Cryo-Electron Microscopy of Vitrified Specimens.” *Quarterly reviews of biophysics* 21(2): 129–228.

Duncan, James, Thomas Bibby, Ayumi Tanaka, and James Barber. 2003. “Exploring the Ability of Chlorophyll b to Bind to the CP43′ Protein Induced under Iron Deprivation in a Mutant of Synechocystis PCC 6803 Containing the Cao Gene.” *FEBS Letters* 541(1): 171–75. doi:https://doi.org/10.1016/S0014-5793(03)00323-5.

Emsley, Paul, Bernhard Lohkamp, Paul Emsley, William G. Scott, Bernhard Lohkamp, Kevin Cowtan, William G. Scott, and Kevin Cowtan. 2010. “Features and Development of Coot.” *Acta Crystallographica Section D-biological Crystallography*. doi:10.1107/s0907444910007493.

Fernandez-Leiro, Rafael, and Sjors HW Scheres. 2017. “A Pipeline Approach to Single-Particle Processing in RELION.” *Acta Crystallographica Section D: Structural Biology* 73(6): 496–502.

Förster, Th, and Theodor Förster. 1947. “Ein Beitrag Zur Theorie Der Photosynthese.” *null*. doi:null.

Gao, Y, YJ Kaufman, D Tanre, D Kolber, and PG Falkowski. 2001. “Seasonal Distributions of Aeolian Iron Fluxes to the Global Ocean.” *Geophysical Research Letters* 28(1): 29–32.

Garczarek, Laurence, Laurence Garczarek, Laurence Garczarek, Wolfgang R. Hess, Wolfgang R. Hess, Julia Holtzendorff, Julia Holtzendorff, et al. 2000. “Multiplication of Antenna Genes as a Major Adaptation to Low Light in a Marine Prokaryote.” *Proceedings of the National Academy of Sciences of the United States of America*. doi:10.1073/pnas.070040897.

Genty, Bernard, Jean-Marie Briantais, and Neil R Baker. 1989. “The Relationship between the Quantum Yield of Photosynthetic Electron Transport and Quenching of Chlorophyll Fluorescence.” *Biochimica et Biophysica Acta (BBA)-General Subjects* 990(1): 87–92.

Glaeser, Robert M. 2016. “How Good Can Cryo-EM Become?” *Nature methods* 13(1): 28–32.

Glaeser, Robert M. 2018. “Proteins, Interfaces, and Cryo-EM Grids.” *Current opinion in colloid & interface science* 34: 1–8.

Grossman, Arthur R, Michael R Schaefer, Gisela G Chiang, and JL372933 Collier. 1993. “The Phycobilisome, a Light-Harvesting Complex Responsive to Environmental Conditions.” *Microbiological reviews* 57(3): 725–49.

Guikema, James A., and Louis A. Sherman. 1983. “Organization and Function of Chlorophyll in Membranes of Cyanobacteria during Iron Starvation.” *Plant Physiology* 73(2): 250–56. doi:10.1104/pp.73.2.250.

Gunner, MR. 2008. “Computational Analysis of Photosynthetic Systems.” *Photosynthesis research* 97: 1–3.

Havaux, Michel, Geneviève Guedeney, Martin Hagemann, Nataliya Yeremenko, Hans C.P. Matthijs, and Robert Jeanjean. 2005. “The Chlorophyll-Binding Protein IsiA Is Inducible by High Light and Protects the Cyanobacterium Synechocystis PCC6803 from Photooxidative Stress.” *FEBS Letters* 579(11): 2289–93. doi:10.1016/j.febslet.2005.03.021.

Henderson, Richard, Joyce M Baldwin, Thomas A Ceska, Friedrich Zemlin, Erich Beckmann, and Kenneth H Downing. 1990. “Model for the Structure of Bacteriorhodopsin Based on High-Resolution Electron Cryo-Microscopy.” *Journal of molecular biology* 213(4): 899–929.

Henderson, Richard, and P Nigel T Unwin. 1975. “Three-Dimensional Model of Purple Membrane Obtained by Electron Microscopy.” *Nature* 257(5521): 28–32.

Holzwarth, Alfred R. 1996. “Data Analysis of Time-Resolved Measurements.” *Biophysical techniques in photosynthesis*: 75–92.

Ihalainen, Janne A., Sandrine D’Haene, Nataliya Yeremenko, Henny Van Roon, Ana A. Arteni, Egbert J. Boekema, Rienk Van Grondelle, Hans C.P. Matthijs, and Jan P. Dekker. 2005. “Aggregates of the Chlorophyll-Binding Protein IsiA (CP43′) Dissipate Energy in Cyanobacteria.” *Biochemistry* 44(32): 10846–53. doi:10.1021/bi0510680.

Jimenez, Ralph, and Graham R Fleming. 1996. “Ultrafast Spectroscopy of Photosynthetic Systems.” *Biophysical techniques in photosynthesis*: 63–73.

Joliot, Pierre, and Giles N Johnson. 2011. “Regulation of Cyclic and Linear Electron Flow in Higher Plants.” *Proceedings of the National Academy of Sciences* 108(32): 13317–22.

Jordan, Patrick, Petra Fromme, Horst Tobias Witt, Olaf Klukas, Wolfram Saenger, and Norbert Krauß. 2001. “Three-Dimensional Structure of Cyanobacterial Photosystem I at 2.5 Å Resolution.” *Nature* 411(6840): 909–17. doi:10.1038/35082000.

Kaneko, Takakazu, and Satoshi Tabata. 1997. “Complete Genome Structure of the Unicellular Cyanobacterium Synechocystis Sp. PCC6803.” *Plant and Cell Physiology* 38(11): 1171–76.

Keeler, James. 2010. *Understanding NMR Spectroscopy*. John Wiley & Sons.

Klughammer, Christof, and Ulrich Schreiber. 1998. “Measuring P700 Absorbance Changes in the Near Infrared Spectral Region with a Dual Wavelength Pulse Modulation System.” In *Photosynthesis: Mechanisms and Effects: Volume I–V: Proceedings of the XIth International Congress on Photosynthesis, Budapest, Hungary, August 17–22, 1998*, ed. G. Garab. Dordrecht: Springer Netherlands, 4357–60. doi:10.1007/978-94-011-3953-3_1008.

Kojima, Kouji, Toyoko Suzuki-Maenaka, Toshihiko Kikuchi, and Hitoshi Nakamoto. 2006. “Roles of the Cyanobacterial isiABC Operon in Protection from Oxidative and Heat Stresses.” *Physiologia Plantarum* 128(3): 507–19.

Kortüm, G, Wo Braun, and G Herzog. 1963. “Principles and Techniques of Diffuse-Reflectance Spectroscopy.” *Angewandte Chemie International Edition in English* 2(7): 333–41.

Kouřil, Roman, Ana A. Arteni, Julia Lax, Nataliya Yeremenko, Sandrine D'Haene, Matthias Rögner, Hans C.P. Matthijs, Jan P. Dekker, and Egbert J. Boekema. 2005. "Structure and Functional Role of Supercomplexes of IsiA and Photosystem I in Cyanobacterial Photosynthesis." *FEBS Letters* 579(15): 3253–57. doi:10.1016/j.febslet.2005.03.051.

Kouřil, Roman, R. Kouril, Ana-Andreea Arteni, Roman Kouřil, Ana A. Arteni, Julia E.-M. Lax, Julia Lax, et al. 2005. "Structure and Functional Role of Supercomplexes of IsiA and Photosystem I in Cyanobacterial Photosynthesis." *FEBS Letters*. doi:10.1016/j.febslet.2005.03.051.

Kruse, Olaf, Jens Rupprecht, Jan H Mussgnug, G Charles Dismukes, and Ben Hankamer. 2005. "Photosynthesis: A Blueprint for Solar Energy Capture and Biohydrogen Production Technologies." *Photochemical & Photobiological Sciences* 4(12): 957–70.

Kucukelbir, Alp, Fred J. Sigworth, Alp Kucukelbir, Hemant D. Tagare, Fred J. Sigworth, and Hemant D. Tagare. 2014. "Quantifying the Local Resolution of Cryo-EM Density Maps." *Nature Methods*. doi:10.1038/nmeth.2727.

Kurisu, Genji, Huamin Zhang, Janet L Smith, and William A Cramer. 2003. "Structure of the Cytochrome B6f Complex of Oxygenic Photosynthesis: Tuning the Cavity." *Science* 302(5647): 1009–14.

Laudenbach, David E., David E. Laudenbach, Neil A. Straus, and Neil A. Straus. 1988. "Characterization of a Cyanobacterial Iron Stress-Induced Gene Similar to psbC." *Journal of Bacteriology*. doi:10.1128/jb.170.11.5018-5026.1988.

Li, Xueming, Paul Mooney, Shawn Zheng, Christopher R Booth, Michael B Braunfeld, Sander Gubbens, David A Agard, and Yifan Cheng. 2013. "Electron Counting and Beam-Induced Motion Correction Enable near-Atomic-Resolution Single-Particle Cryo-EM." *Nature methods* 10(6): 584–90.

Los, Dmitry A, Anna Zorina, Maria Sinetova, Sergey Kryazhov, Kirill Mironov, and Vladislav V Zinchenko. 2010. "Stress Sensors and Signal Transducers in Cyanobacteria." *Sensors* 10(3): 2386–2415.

Maiuri, Margherita, Marco Garavelli, and Giulio Cerullo. 2019. "Ultrafast Spectroscopy: State of the Art and Open Challenges." *Journal of the American Chemical Society* 142(1): 3–15.

Malavath, Tirupathi, Tirupathi Malavath, Ido Caspy, Ido Caspy, Sigal Yoli Netzer-El, Sigal Y. Netzer-El, Daniel Klaiman, et al. 2018. "Structure and Function of Wild-Type and Subunit-Depleted Photosystem I in Synechocystis." *Biochimica et Biophysica Acta*. doi:10.1016/j.bbabio.2018.02.002.

Mazor, Yuval, Yuval Mazor, Anna Borovikova, Anna Borovikova, Ido Caspy, Ido Caspy, Nathan Nelson, and Nathan Nelson. 2017. "Structure of the Plant Photosystem I Supercomplex at 2.6 Å Resolution." *Nature plants*. doi:10.1038/nplants.2017.14.

Mazor, Yuval, Yuval Mazor, Anna Borovikova, Nathan Nelson, Anna Borovikova, and Nathan Nelson. 2015. “The Structure of Plant Photosystem I Super-Complex at 2.8 Å Resolution.” *eLife*. doi:10.7554/elife.07433.

Melkozernov, Alexander N., Alexander N. Melkozernov, Thomas S. Bibby, Thomas S. Bibby, Su Lin, Su Lin, Su Lin, et al. 2003. “Time-Resolved Absorption and Emission Show That the CP43’ Antenna Ring of Iron-Stressed Synechocystis Sp. PCC6803 Is Efficiently Coupled to the Photosystem I Reaction Center Core.” *Biochemistry*. doi:10.1021/bi026987u.

Michel, Klaus-Peter, and Elfriede K Pistorius. 2004. “Adaptation of the Photosynthetic Electron Transport Chain in Cyanobacteria to Iron Deficiency: The Function of IdiA and IsiA.” *Physiologia plantarum* 120(1): 36–50.

Mirkovic, Tihana, Evgeny E Ostroumov, Jessica M Anna, Rienk Van Grondelle, Govindjee, and Gregory D Scholes. 2017. “Light Absorption and Energy Transfer in the Antenna Complexes of Photosynthetic Organisms.” *Chemical reviews* 117(2): 249–93.

Mitra, Kakoli, and Joachim Frank. 2006. “Ribosome Dynamics: Insights from Atomic Structure Modeling into Cryo-Electron Microscopy Maps.” *Annu. Rev. Biophys. Biomol. Struct.* 35: 299–317.

Mullineaux, Conrad W., and Daniel Emlyn-Jones. 2005. “State Transitions: An Example of Acclimation to Low-Light Stress.” *Journal of Experimental Botany* 56(411): 389–93. doi:10.1093/jxb/eri064.

Mullineaux, Conrad W, and Alfred R Holzwarth. 1991. “Kinetics of Excitation Energy Transfer in the Cyanobacterial Phycobilisome-Photosystem II Complex.” *Biochimica et Biophysica Acta (BBA)-Bioenergetics* 1098(1): 68–78.

Mullineaux, Conrad W, Andrew A Pascal, Peter Horton, and Alfred R Holzwarth. 1993. “Excitation-Energy Quenching in Aggregates of the LHC II Chlorophyll-Protein Complex: A Time-Resolved Fluorescence Study.” *Biochimica et Biophysica Acta (BBA)-Bioenergetics* 1141(1): 23–28.

Munekage, Yuri, Mihoko Hashimoto, Chikahiro Miyake, Ken-Ichi Tomizawa, Tsuyoshi Endo, Masao Tasaka, and Toshiharu Shikanai. 2004. “Cyclic Electron Flow around Photosystem I Is Essential for Photosynthesis.” *Nature* 429(6991): 579–82.

Murata, Kazuyoshi, and Matthias Wolf. 2018. “Cryo-Electron Microscopy for Structural Analysis of Dynamic Biological Macromolecules.” *Biochimica et Biophysica Acta (BBA)-General Subjects* 1862(2): 324–34.

Nakajima, Tsubasa, Shuichi Kajihata, Katsunori Yoshikawa, Fumio Matsuda, Chikara Furusawa, Takashi Hirasawa, and Hiroshi Shimizu. 2014. “Integrated Metabolic Flux and Omics Analysis of Synechocystis Sp. PCC 6803 under Mixotrophic and Photoheterotrophic Conditions.” *Plant and Cell Physiology* 55(9): 1605–12.

Nelson, Nathan, and Adam Ben-Shem. 2004. “The Complex Architecture of Oxygenic Photosynthesis.” *Nature Reviews Molecular Cell Biology* 5(12): 971–82. doi:10.1038/nrm1525.

Nelson, Nathan, Nathan Nelson, Wolfgang Junge, and Wolfgang Junge. 2015. “Structure and Energy Transfer in Photosystems of Oxygenic Photosynthesis.” *Annual Review of Biochemistry*. doi:10.1146/annurev-biochem-092914-041942.

Nelson, Nathan, and Charles F. Yocum. 2006. “Structure and Function of Photosystems I and Ii.” *Annual Review of Plant Biology* 57(1): 521–65. doi:10.1146/annurev.arplant.57.032905.105350.

Nogales, Eva. 2016. “The Development of Cryo-EM into a Mainstream Structural Biology Technique.” *Nature methods* 13(1): 24–27.

Opatíková, Monika, Dmitry A Semchonok, David Kopečnỳ, Petr Ilík, Pavel Pospíšil, Iva Ilíková, Pavel Roudnickỳ, et al. 2023. “Cryo-EM Structure of a Plant Photosystem II Supercomplex with Light-Harvesting Protein Lhcb8 and α-Tocopherol.” *Nature Plants* 9(8): 1359–69.

Palovcak, Eugene, Feng Wang, Shawn Q Zheng, Zanlin Yu, Sam Li, Miguel Betegon, David Bulkley, David A Agard, and Yifan Cheng. 2018. “A Simple and Robust Procedure for Preparing Graphene-Oxide Cryo-EM Grids.” *Journal of structural biology* 204(1): 80–84.

Pan, Xiaowei, Xiaowei Pan, Jun Ma, Xiaodong Su, Jun Ma, Peng Cao, Xiaodong Su, et al. 2018. “Structure of the Maize Photosystem I Supercomplex with Light-Harvesting Complexes I and II.” *Science*. doi:10.1126/science.aat1156.

Pathania, Ruchi, Amit Srivastava, Shireesh Srivastava, and Pratyoosh Shukla. 2022. “Metabolic Systems Biology and Multi-Omics of Cyanobacteria: Perspectives and Future Directions.” *Bioresource Technology* 343: 126007.

Pettersen, Eric F., Thomas D. Goddard, Eric F. Pettersen, Conrad C. Huang, Thomas D. Goddard, Conrad C. Huang, Gregory S. Couch, et al. 2004. “UCSF Chimera–a Visualization System for Exploratory Research and Analysis.” *Journal of Computational Chemistry*. doi:10.1002/jcc.20084.

Pi, Xiong, Xiong Pi, Lirong Tian, Lirong Tian, Huai En Dai, Huai En Dai, Xiaochun Qin, et al. 2018. “Unique Organization of Photosystem I-Light Harvesting Supercomplex Revealed by Cryo-EM from a Red Alga.” *Proceedings of the National Academy of Sciences of the United States of America*. doi:10.1073/pnas.1722482115.

Pisciotta, John M, YongJin Zou, and Ilia V Baskakov. 2010. “Light-Dependent Electrogenic Activity of Cyanobacteria.” *PloS one* 5(5): e10821.

Punjani, Ali, John L Rubinstein, David J Fleet, and Marcus A Brubaker. 2017. “cryoSPARC: Algorithms for Rapid Unsupervised Cryo-EM Structure Determination.” *Nature methods* 14(3): 290–96.

Qin, Xiaochun, Xiong Pi, Wenda Wang, Guangye Han, Lixia Zhu, Mingmei Liu, Linpeng Cheng, et al. 2019. “Structure of a Green Algal Photosystem I in Complex with a Large Number of Light-Harvesting Complex I Subunits.” *Nature Plants* 5(3): 263–72.

Qin, Xiaochun, Xiaochun Qin, Michihiro Suga, Tingyun Kuang, Michihiro Suga, Jian Ren Shen, Tingyun Kuang, and Jian-Ren Shen. 2015. “Structural Basis for Energy Transfer Pathways in the Plant PSI-LHCI Supercomplex.” *Science*. doi:10.1126/science.aab0214.

Raymond, Jason, and Robert E Blankenship. 2008. “The Origin of the Oxygen-Evolving Complex.” *Coordination chemistry reviews* 252(3–4): 377–83.

Ringsmuth, Andrew K., Michael J. Landsberg, and Ben Hankamer. 2016. “Can Photosynthesis Enable a Global Transition from Fossil Fuels to Solar Fuels, to Mitigate Climate Change and Fuel-Supply Limitations?” *Renewable and Sustainable Energy Reviews* 62: 134–63. doi:https://doi.org/10.1016/j.rser.2016.04.016.

Roche, J. La, G. W. M. van der Staay, G. W. M. van der Staay, Frédéric Partensky, Frédéric Partensky, Axel Ducret, A. Ducret, et al. 1996. “Independent Evolution of the Prochlorophyte and Green Plant Chlorophyll a/b Light-Harvesting Proteins.” *Proceedings of the National Academy of Sciences of the United States of America*. doi:10.1073/pnas.93.26.15244.

Rohou, Alexis, and Nikolaus Grigorieff. 2015. “CTFFIND4: Fast and Accurate Defocus Estimation from Electron Micrographs.” *Journal of structural biology* 192(2): 216–21.

Saer, Rafael G., Rafael G. Saer, Robert E. Blankenship, and Robert E. Blankenship. 2017. “Light Harvesting in Phototrophic Bacteria: Structure and Function.” *Biochemical Journal*. doi:10.1042/bcj20160753.

Sahoo, Harekrushna. 2011. “Förster Resonance Energy Transfer–A Spectroscopic Nanoruler: Principle and Applications.” *Journal of Photochemistry and Photobiology C: Photochemistry Reviews* 12(1): 20–30.

Scheres, Sjors H. W., and Sjors H. W. Scheres. 2012. “RELION: Implementation of a Bayesian Approach to Cryo-EM Structure Determination.” *Journal of Structural Biology*. doi:10.1016/j.jsb.2012.09.006.

Scheres, Sjors H. W., Sjors H. W. Scheres, Shao-Xia Chen, Shaoxia Chen, and Shaoxia Chen. 2012. “Prevention of Overfitting in Cryo-EM Structure Determination.” *Nature Methods*. doi:10.1038/nmeth.2115.

Scheres, Sjors HW. 2012. “RELION: Implementation of a Bayesian Approach to Cryo-EM Structure Determination.” *Journal of structural biology* 180(3): 519–30.

Scheres, Sjors HW. 2019. “Single-Particle Processing in RELION-3.1.” *MRC Lab. Mol. Biol., Cambridge, UK, Tutorial RELION-3.1*.

Schreiber, Ulrich, Christof Klughammer, and Christian Neubauer. 1988. “Measuring P700 Absorbance Changes around 830 Nm with a New Type of Pulse Modulation System.” *Zeitschrift für Naturforschung C* 43(9–10): 686–98.

Setif, P, and P Mathis. 1980. “The Oxidation-Reduction Potential of P-700 in Chloroplast Lamellae and Subchloroplast Particles.” *Archives of Biochemistry and Biophysics* 204(2): 477–85.

Shen, Gaozhong, Fei Gan, and Donald A Bryant. 2016. “The Siderophilic Cyanobacterium Leptolyngbya Sp. Strain JSC-1 Acclimates to Iron Starvation by Expressing Multiple isiA-Family Genes.” *Photosynthesis research* 128: 325–40.

Singh, Abhay K., Hong Li, and Louis A. Sherman. 2004. “Microarray Analysis and Redox Control of Gene Expression in the Cyanobacterium Synechocystis Sp. PCC 6803.” *Physiologia Plantarum* 120(1): 27–35. doi:10.1111/j.0031-9317.2004.0232.x.

Sobotka, Roman, Ulf Duhring, Josef Komenda, Enrico Peter, Zdenko Gardian, Martin Tichy, Bernhard Grimm, and Annegret Wilde. 2008. “Importance of the Cyanobacterial Gun4 Protein for Chlorophyll Metabolism and Assembly of Photosynthetic Complexes.” *Journal of Biological Chemistry* 283(38): 25794–802.

Sparrow, Raymond, Robert G Brown, E Hilary Evans, and David Shaw. 1990. “Time-Resolved Spectroscopy of Photosynthetic Systems. 3: Photosystem 1 Preparations from the Cyanobacterium Chlorogloea Fritschii.” *Journal of Photochemistry and Photobiology B: Biology* 5(3–4): 445–55.

van Stokkum, Ivo HM, Delmar S Larsen, and Rienk Van Grondelle. 2004. “Global and Target Analysis of Time-Resolved Spectra.” *Biochimica et Biophysica Acta (BBA)-Bioenergetics* 1657(2–3): 82–104.

Stroebel, David, Yves Choquet, Jean-Luc Popot, and Daniel Picot. 2003. “An Atypical Haem in the Cytochrome b 6 f Complex.” *Nature* 426(6965): 413–18.

Su, Xiaodong, Xiaodong Su, Jun Ma, Jun Ma, Xuepeng Wei, Xuepeng Wei, Peng Cao, et al. 2017. “Structure and Assembly Mechanism of Plant C2S2M2-Type PSII-LHCII Supercomplex.” *Science*. doi:10.1126/science.aan0327.

Suga, Michihiro, Michihiro Suga, Jian Ren Shen, and Jian-Ren Shen. 2020. “Structural Variations of Photosystem I-Antenna Supercomplex in Response to Adaptations to Different Light Environments.” *Current Opinion in Structural Biology*. doi:10.1016/j.sbi.2020.02.005.

Sundström, Villy. 2008. “Femtobiology.” *Annu. Rev. Phys. Chem.* 59: 53–77.

Thomas, Steven, Nathaniel D Maynard, and John Gill. 2015. “DNA Library Construction Using Gibson Assembly®.” *Nature Methods* 12(11): i–ii.

Thompson, Adam, Ian Maskery, and Richard K Leach. 2016. “X-Ray Computed Tomography for Additive Manufacturing: A Review.” *Measurement Science and Technology* 27(7): 072001.

Toporik, Hila, Jin Li, Dewight Williams, Po Lin Chiu, and Yuval Mazor. 2019. “The Structure of the Stress-Induced Photosystem I–IsiA Antenna Supercomplex.” *Nature Structural and Molecular Biology* 26(6): 443–49. doi:10.1038/s41594-019-0228-8.

Trebst, Ann. 1974. “Energy Conservation in Photosynthetic Electron Transport of Chloroplasts.” *Annual Review of Plant Physiology* 25(1): 423–58.

Umena, Yasufumi, Yasufumi Umena, Keisuke Kawakami, Keisuke Kawakami, Jian Ren Shen, Jian-Ren Shen, Nobuo Kamiya, and Nobuo Kamiya. 2011. “Crystal Structure of Oxygen-Evolving Photosystem II at a Resolution of 1.9 Å.” *Nature*. doi:10.1038/nature09913.

Unwin, Nigel, and Yoshinori Fujiyoshi. 2012. “Gating Movement of Acetylcholine Receptor Caught by Plunge-Freezing.” *Journal of molecular biology* 422(5): 617–34.

Unwin, P Nigel T, and Richard Henderson. 1975. “Molecular Structure Determination by Electron Microscopy of Unstained Crystalline Specimens.” *Journal of molecular biology* 94(3): 425–40.

Wei, Xuepeng, Xuepeng Wei, Xiaodong Su, Xiaodong Su, Peng Cao, Peng Cao, Peng Cao, et al. 2016. “Structure of Spinach Photosystem II–LHCII Supercomplex at 3.2 Å Resolution.” *Nature*. doi:10.1038/nature18020.

Whitton, Brian A, and Malcolm Potts. 2007. *The Ecology of Cyanobacteria: Their Diversity in Time and Space*. Springer Science & Business Media.

Wikipedia contributors. 2024. “Chlorophyll — Wikipedia, The Free Encyclopedia.” https://en.wikipedia.org/w/index.php?title=Chlorophyll&oldid=1197207048.

Xu, Min, Gabor Bernat, Abhay Singh, Hualing Mi, Matthias Rögner, Himadri B Pakrasi, and Teruo Ogawa. 2008. “Properties of Mutants of Synechocystis Sp. Strain PCC 6803 Lacking Inorganic Carbon Sequestration Systems.” *Plant and Cell Physiology* 49(11): 1672–77.

Yeremenko, Nataliya, Roman Kouřil, Nataliya Yeremenko, Janne A. Ihalainen, R. Kouril, Janne A. Ihalainen, Sandrine D’Haene, et al. 2004. “Supramolecular Organization and Dual Function of the IsiA Chlorophyll-Binding Protein in Cyanobacteria.” *Biochemistry*. doi:10.1021/bi048772l.

Zhang, Jun, Jianfei Ma, Desheng Liu, Song Qin, Shan Sun, Jindong Zhao, and Sen-Fang Sui. 2017. “Structure of Phycobilisome from the Red Alga Griffithsia Pacifica.” *Nature* 551(7678): 57–63.

Zhang, Yinan, Min Chen, W Bret Church, Kwok Wai Lau, Anthony WD Larkum, and Lars S Jermiin. 2010. “The Molecular Structure of the IsiA–Photosystem I Supercomplex, Modelled from High-Resolution, Crystal Structures of Photosystem I and the CP43 Protein.” *Biochimica et Biophysica Acta (BBA)-Bioenergetics* 1797(4): 457–65.

Zheng, Sijie, Eugene Palovcak, Shawn Q. Zheng, Eugene Palovcak, Jean-Paul Armache, Jean-Paul Armache, Yifan Cheng, et al. 2016. “Anisotropic Correction of Beam-Induced Motion for Improved Single-Particle Electron Cryo-Microscopy.” *bioRxiv*. doi:10.1101/061960.

Zivanov, Jasenko, Takanori Nakane, Björn O Forsberg, Dari Kimanius, Wim JH Hagen, Erik Lindahl, and Sjors HW Scheres. 2018. “New Tools for Automated High-Resolution Cryo-EM Structure Determination in RELION-3.” *elife* 7: e42166.

APPENDIX A

PERMISSIONS

Chapter 1:

Figure 1.2. Figure reproduced with permission of G. Govindjee and W. Viet (https://www.life.illinois.edu/govindjee/Z-Scheme.html)

Figure 1.4. Reproduced under the terms of the Creative Commons CC-BY license Sobotka, Roman, Ulf Duhring, Josef Komenda, Enrico Peter, Zdenko Gardian, Martin Tichy, Bernhard Grimm, and Annegret Wilde. 2008. “Importance of the Cyanobacterial Gun4 Protein for Chlorophyll Metabolism and Assembly of Photosynthetic Complexes.” Journal of Biological Chemistry 283(38): 25794–802. (Sobotka et al. 2008)

Figure 1.6 Reprinted from Ringsmuth, Andrew K., Michael J. Landsberg, and Ben Hankamer. 2016. “Can Photosynthesis Enable a Global Transition from Fossil Fuels to Solar Fuels, to Mitigate Climate Change and Fuel-Supply Limitations?” Renewable and Sustainable Energy Reviews 62: 134–63. doi:https://doi.org/10.1016/j.rser.2016.04.016.(Ringsmuth, Landsberg, and Hankamer 2016)

Figure 1.9 Reprinted with permission from Chauhan, Devendra Kumar, Devendra K. Chauhan, I. Mihaela Folea, I. Mihaela Folea, Craig C. Jolley, Craig C. Jolley, Roman Kouřil, et al. 2011. “A Novel Photosynthetic Strategy for Adaptation to Low-Iron Aquatic Environments.” Biochemistry. doi:10.1021/bi1009425. (Chauhan et al. 2011)

Figure 1.10 &1.15 Reprint with permission from Nogales, Eva. 2016. “The Development of Cryo-EM into a Mainstream Structural Biology Technique.” Nature methods 13(1): 24–27. (Nogales 2016)

Chapter 2:

Figure 2.1 Reprint with permission from Guikema, James A., and Louis A. Sherman. 1983. “Organization and Function of Chlorophyll in Membranes of Cyanobacteria during

Iron Starvation." Plant Physiology 73(2): 250–56. doi:10.1104/pp.73.2.250. (Guikema and Sherman 1983)

Figure 2.2 Reprint with permission from Bibby, Thomas S., Thomas S. Bibby, Isabelle Mary, Isabelle Mary, I. Mary, I. Mary, Jon Nield, et al. 2003. "Low-Light-Adapted Prochlorococcus Species Possess Specific Antennae for Each Photosystem." Nature. doi:10.1038/nature01933. (Thomas S. Bibby et al. 2001; James Duncan et al. 2003)